LARGE IMPACT CRATERS AND BASINS: MECHANICS OF SYNGENETIC AND POSTGENETIC MODIFICATION

Thesis by

William Beall McKinnon

In Partial Fulfillment of the Requirements

For the Degree of

Doctor of Philosophy

California Institute of Technology

Pasadena, California

1981

(Submitted July 25, 1980)

Copyright © by

William Beall McKinnon

1980

To my parents

ACKNOWLEDGMENTS

It is my great pleasure to thank Dr. H.J. Melosh for his support and enthusiasm as a thesis advisor. As we traveled down the parallel path of research, I can only hope I gleaned some measure of his physical intuition.

My interactions with others here has likewise been quite stimulating. I particularly thank Drs. Andy Ingersoll, Dewey Muhleman and Gene Shoemaker for making Caltech memorable.

My fellow graduates provided much needed scientific and moral support, among them Bruce Bills, Tony Dobrovolskis, Quinn Passey, David Pollard, and Daniel Wenkert.

Life, of course, continues beyond this realm, and I am indebted to many. To Dave Brock, Bob Calvert, Brian Eno, Patrick McGoohan, Chris O'Dea, the Prufrockers, Marc Southerland, Richard and Linda Thompson, Nik Turner, and Steve Zeitzew goes cosmic kudos.

I must extend my deepest appreciation to Juliet Seigle, who acted as an oasis of sanity and joy during the longest days of this research.

This work would not have been completed without the help of many: Dr. Ron Scott provided valuable time on his centrifuge and John Lee supplied technical assistance in its operation; the Department of Earth and Space Science at SUNY Stony Brook and Arthur Raefsky were most hospitable during the winter of 1979-1980; Dr. A. Woronow brought to my attention the work of Dr. M. Ashby on ice deformation; Drs. Ron Greeley and Gerald Schaber kindly sent advance versions of their Mercury

quadrangle geologic maps; David Jewitt graciously donated his lunar terrace width measurements; Kathleen Lee provided priceless photographic assistance; Ben Sewell and the gang at Graphic Arts were diligent and precise; Jan Mayne supplied quality draftsmanship.

Without the typing skill of Kay Campbell and the divine intervention of Donna Lathrop (*deus ex selectric*) all of this would have been impossible.

I thank the Earle C. Anthony Foundation for support during the first year of my graduate career. Most of the rest was due to NASA grant NSG-7316, and gratefully acknowledged.

PREFACE

The furthermost, the outermost, the most peripheral sensations of the times in which we live are bound up with the G that is the inevitable concomitant of space flight. Almost certainly, the remotest extremities of everyday sensation in our age blend with G. We live in an age where the ultimate in what was once referred to as the psyche resolves itself into G. All love and hate that does not anticipate G somewhere in the distance is invalid.

G is the physical compelling force of the divine; and yet it is an intoxication that lies at the opposite extreme from intoxication, an intellectual limit that lies at the opposite extreme from the outer limit of the intellect.

- Yukio Mishima

Sun and Steel

ABSTRACT

The impact crater is the ubiquitous landform of the solar system. Theoretical mechanical analyses are applied to the modification stage of crater formation, both syngenetic (immediate or short term) and postgenetic (long term).

The mechanical stability of an impact crater is analyzed via a quasi-static, axisymmetric slip line theory of plasticity. The yield model incorporated is Mohr-Coulomb and a simplified rectangular profile is used for the transient cavity. The degree of stability (or instability) is described as a function of internal friction angle, depth/diameter ratio, and a dimensionless parameter $\rho gH/c$ (ρ = density, g = acceleration of gravity, H = depth, and c = cohesion strength). To match the observed slumping of large lunar craters the cohesion strength of the lunar surface material must be low (<20 bars) and the angle of internal friction must be less than 2°. It is not implausible that these failure strength characteristics are realized by freshly shocked rock. A theoretical description of impact crater collapse is evolved which accounts for the development of wall scallops, slump terraces, and flat floors. A preliminary set of scale model experiments performed in a centrifuge corroborate the theory. The strength of terrestrial planet surfaces under impact is seen to vary by as much as a factor of two.

Shortly after the excavation of a *large* impact crater the transient cavity collapses, driven by gravity. It is shown that at least one concentric fault scarp forms *about* the crater, if the strength of the

target material decreases sufficiently rapidly with increasing depth. This is demonstrated by two classes of models: extrusion flow models which assume a weak layer underlying a strong layer, and plastic flow models which assume a continuous decrease of cohesion strength with depth. Both classes predict that the ratio of the radius of the scarp to the transient crater radius is between 1.2 and 2 for large craters.

Large impact basins on Ganymede and Callisto are characterized by one or more concentric rings or scarps. The number, spacing, and morphology of the rings is a function of the thickness and strength of the lithosphere, and crater diameter. When the lithosphere is thin and weak, the collapse is regulated by flow induced in the asthenosphere. The lithosphere fragments in a multiply concentric pattern (e.g., Valhalla, Asgard, Galileo Regio, and a newly discovered ring system on Callisto). The thickness and viscosity of a planetary lithosphere increases with time as the mantle cools. A thicker lithosphere leads to the formation of one (or very few) irregular normal faults concentric to the crater (e.g., Gilgamesh). A gravity wave or tsunami induced by impact into a liquid mantle would result in both *concentric and radial* extension features. Since these are not observed, this process cannot be responsible for the generation of the rings around the basins on Ganymede and Callisto. The appearance of Galileo Regio and portions of Valhalla is best explained by ring graben, and though the Valhalla system is older, the lithosphere was 1.5-2.0 times as thick at the time of formation. The present lithosphere thickness is too great to permit development of any rings.

It has been proposed that a mascon may be in the form of an annulus surrounding the Caloris basin on Mercury, associated with the smooth plains. The effects (stresses, deformation, surface tectonic style, gravity anomalies, etc.) of such a ring load on a floating elastic lithosphere of variable thickness are investigated. The main characteristics of the surface tectonic pattern are normal faulting within the basin and thrust faulting beneath the ring load, both in agreement with observation . Moreover, the dominant concentric trend of the basin normal faults is consistent with the ring load hypothesis provided the mercurian lithosphere was $\leqslant$125 km thick at the time of faulting. Simple updoming within the basin would produce normal faults of predominantly radial orientation.

TABLE OF CONTENTS

Page

FIGURES

FIGURES (Continued) Page

FIGURES (Continued) Page

TABLES

I. CONCERNING THE MODIFICATION OF IMPACT CRATERS AND BASINS

a) Introduction

A crater is a cup or bowl shaped depression. The term crater in non-generic. This broad definition is necessary as many of these "depressions" studied herein will scarcely resemble each other at first. However, the purpose of this work is to explore crater genesis and to quantify the relationships between the various crater morphologies.

The crater is the ubiquitous landform of the solar system. It is predominant on the moon, Mercury, Mars, Diemos, Phobos, Ganymede, Callisto, and Amalthea. Craters will probably be found in abundance on other worlds of low geologic activity as the reconnaissance of the solar system continues. They are relatively rare on the earth, which accounts for their unfamiliarity. Yet they were recognized immediately at the dawn of modern astronomy by Galileo, as he trained his new device, the telescope, on the moon. The name he gave them, κρατερ, survives.

As for the origin of these roughly circular cavities, overwhelming evidence supports the *Aufsturzhypothese* (Gilbert, 1893; Wegener[1], 1920; and see Shoemaker, 1962) or the impact hypothesis. G.K. Gilbert, first Chief Geologist of the United States Geological Survey, broke from his predecessors and contemporaries and ascribed the origin of lunar craters to the impact of objects of various sizes traveling at cosmic velocities, although he admitted a small

---

[1] Better known for his advocacy of continental drift.

fraction could be volcanic. Gilbert's detailed study of the similarities between impacts at the smallest scales and at the largest, which he considered to be the circular maria, has not been truly outdated.

Before an examination of crater modification can begin, crater formation should be understood. What follows is a brief summary of the mechanics of impact cratering as deduced from high-explosive and nuclear-explosive tests, geological investigations of terrestrial impact structures, laboratory high-explosive and impact experiments, and large computer code theoretical models. As a final note, the word geology will be generalized to encompass such deviants as selenology, hermeology, etc., in accordance with present usage.

b) Mechanics

Excavation of an impact crater begins at the first contact between the cosmic object, or projectile, and the planetary surface, or target. For simplicity, assume both to be structurally and chemically homogeneous. Atmospheric effects (Krinov, 1960; Passey and Melosh, 1980) are not considered germane to the present discussion, which draws heavily from E.M. Shoemaker's pioneering analysis of cratering mechanics as applied to Meteor Crater, Arizona and D.E. Gault's hypervelocity impact experiments performed at NASA-Ames Research Center (see in particular Shoemaker, 1963 and Gault *et al.*, 1968).

Typical impact velocities are on the order of 10 km/sec, resulting in a high pressure shock wave propagating onto the target, accelerating it forward, and one propagating back into and decelerating the meteorite (though not reversing its motion). Jumps in pressure across the shock are on the order of 10^3 GPa (10 Mbar). The actual shock pressures, densities, and velocities are determined by the material properties of both projectile and target (Shoemaker, 1963; Gault and Heitowit, 1963; O'Keefe and Ahrens, 1975). Tables 1 and 2 are calculations for planar impact of both iron and gabbroic anorthosite into a gabbroic anorthosite target (petrologically dominant in the lunar highlands) at various velocities. The shock compressed wad of meteorite and target rock continues to travel into the planetary surface. The forward shock expands hemispherically, engulfing increasing amounts of the target mass. Eventually, the backward propagating shock reaches the rear surface of the

TABLE 1

Peak shock (impedance match) states for gabbroic anorthosite impacting gabbroic anorthosite.

Impact velocity (km/sec)	Shock pressure (Mbar)	Particle velocity (km/sec)	Shock velocity (km/sec)	Density (gm/cm^3)	Internal[a] energy density (10^{10} erg/g)
5	0.62[b]	2.50	8.45	4.17	3.13
7.5	0.99[b]	3.75	8.99	5.04	7.03
15.0	3.04[c]	7.50	13.81	6.43	28.13
30.0	10.11[d]	15.0	22.96	8.47	112.50
45.0	21.29[d]	22.50	32.23	9.73	253.13

[a]With respect to low-pressure phase of gabbroic anorthosite at STP.

[b]Partial melting upon isentropic release.

[c]Partial vaporization upon isentropic release.

[d]Complete vaporization upon isentropic release.

From Ahrens and O'Keefe (1977).

TABLE 2

Peak shock (impedance match) states for iron impacting gabbroic anorthosite.

Impact velocity (km/sec)	Shock pressure (Mbar)	Particle velocity[a] iron (km/sec)	Shock velocity[a] iron (km/sec)	Density iron (g/cm^3)	Internal energy iron (10^{10} erg/g)	Particle velocity anorthosite (km/sec)	Shock velocity anorthosite (km/sec)	Density anorthosite (g/cm^3)	Internal energy density[b] anorthosite (10^{10} erg/g)
5.0	0.825[c]	1.59	6.60	10.35	1.26	3.41	8.24	5.01	5.81
7.5	1.531[d]	2.51	7.76	11.62	3.15	4.99	10.45	5.62	12.45
15.0	4.807[e]	5.21	11.74	14.13	13.57	9.79	16.72	7.08	47.92
30.0	15.852[f]	10.70	18.85	18.18	57.25	19.30	27.98	9.47	186.25
45.0	33.556[g]	16.35	26.11	21.02	133.66	28.65	39.89	10.42	410.41

[a] With respect to iron, at rest.

[b] With respect to low-pressure phase of gabbroic anorthosite at STP.

[c] Iron solid upon isentropic release; gabbroic anorthosite completely melted upon isentropic release.

[d] Iron solid upon isentropic release; gabbroic anorthosite partially vaporized upon isentropic release.

[e] Both iron and gabbroic anorthosite partially vaporized upon isentropic release.

[f] Gabbroic anorthosite vaporized upon isentropic release; iron partially vaporized.

[g] Both iron and gabbroic anorthosite completely vaporized upon isentropic release.

From Ahrens and O'Keefe (1977)

projectile. This ends what Gault *et al.* (1968) termed the *compression* stage of impact mechanics. This stage is unique to the hypervelocity event, as contrasted with explosion cratering. Timescales range from $\sim 10^{-4}$ to ~ 1 sec for meteorites of ~ 1 m to ~ 10 km diameter (obviously).

The influence of the lateral boundary of the meteorite on the compression stage should not be neglected. Even as the shocks begin to propagate, they intersect a free surface initially formed at the triple junction of projectile, target, and void (planetary atmospheres are essentially vacua with respect to the pressures encountered in cratering). This free surface immediately begins to unload the shocked region via rarefaction from the sides. The material undergoing rarefaction is subjected to a high pressure gradient, decompressed along an isentrope, which generally results in melting or vaporization, and accelerated upward and outward in a jet. Initial contact, jetting, and terminal engulfment are illustrated schematically in figure 1. The degree to which shocked material is heated and volatilized depends on peak shock pressure, as Tables 1 and 2 demonstrate.

As the particle velocities behind the shock are of necessity slower than the shock speed (sometimes by more than a factor of two), at the end of the compression stage the meteorite-target interface has not quite moved one projectile diameter into the ground (and maybe quite a bit less). The shocked region has been substantially unloaded from the sides and material is no longer being solely accelerated downward. An induced upward and outward motion is the

FIGURE 1: The *compression* stage of impact mechanics, from Melosh (1980) and after Gault *et al.* (1968). Shock wave propagation begins at initial contact between the projectile (moving at velocity v) and the target. Shocked projectile and target material is lined and stipled respectively. Arrows denote particle velocities. Rarefaction "waves" (dashed lines) unload the shocked zone from available free surfaces, causing jetting. *Compression* ends when the backward propagating shock reaches the rear of the meteorite, now quite distorted. Jetting segues into the beginning of the ejecta curtain.

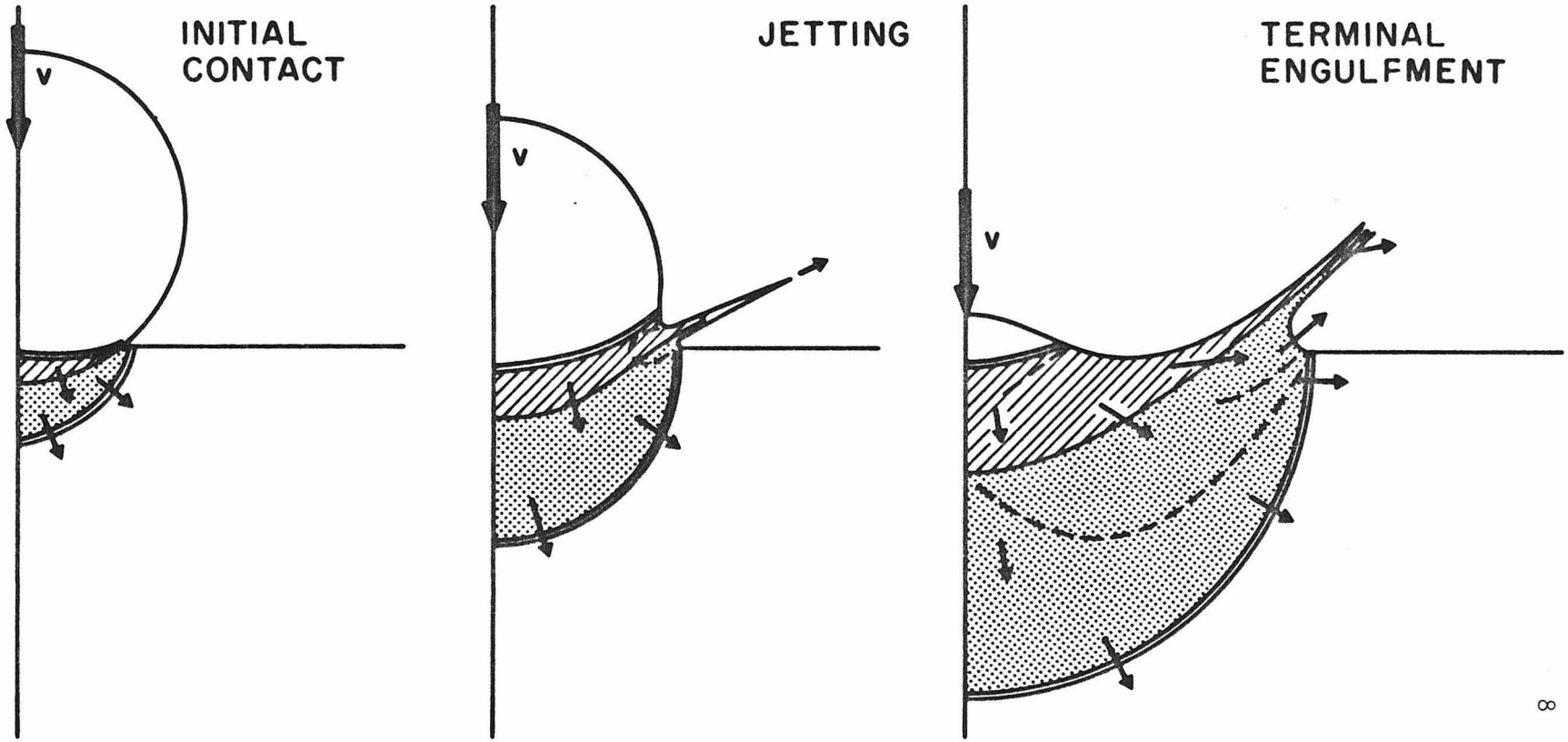
INITIAL
CONTACT
v
JETTING
v
TERMINAL
ENGULFMENT
v

beginning of the ejecta curtain. The meteorite itself is badly distorted, flattening and flowing to the sides. The meteorite has transferred roughly one-half its total energy to the target, partitioned into kinetic and internal energy (Gault and Heitowit, 1963; Ahrens and O'Keefe, 1977; Bryan *et al.*, 1978). Momentum transfer is slower owing to the dominance of the kinetic term in the energy partitioning for the projectile (Thomsen *et al.*, 1979).

Momentum and energy transfer continue in the excavation stage (Gault *et al.*, 1968). The shock wave from the initial contact has reached the back of the meteorite. The shocked region is now unloaded by a rarefaction "wave" propagating from *this* free surface. It travels at the speed of sound in the shocked material and as this must be greater than the shock speed, the rarefaction wave eventually outruns the original hemispherical shock.

The combination of rarefactions from the rear and lateral boundaries of the meteorite and the free surface of the target comprises a complex series of unloading events or waves whose overall effect is to rotate the velocity vectors of the flow field from an essentially radial direction towards the original target surface. Pressures are still high, with the meteorite and target having been subjected to peak pressures far in excess of their mechanical strengths. Typical shear strengths for intact rock specimens are 10^{-1} - 1 GPa (1 - 10 kbar), (Handin, 1966). That which has not vaporized or melted is severely comminuted. Theoretical *and* experimental viscosity estimates for this pressure regime are low, 10^{2}-10^{4} kg $m^{-1}sec^{-1}$ (10^{3}-10^{5} poise), (Jeanloz and Ahrens, 1979).

A dimensional analysis can be made from the ratio of strain rate to stress

$$\eta \simeq \sigma/\dot{\epsilon} \sim \sigma/\frac{1}{\tau}\frac{\Delta V}{V} \quad , \tag{1.1}$$

with a shock rise time of 10^{-1} μsec, ratio of specific volumes of order 10^{-1} and identifying σ with the difference between shock-induced and hydrostatic compressions ($\lesssim$ 10 GPa), $\eta \leqslant 10^{2}$ kg $m^{-1}sec^{-1}$ (10^{3} poise). The shock accelerated material, its mechanical integrity destroyed, flows in a hydrodynamic fashion. Flow velocities are basically radially outward from the point of initial contact. The flow field (see fig. 2) in approximately the upper one-third of the crater has an upward velocity component and most of this material will be ejected (Stöffler *et al.*, 1975), traveling ballistically on atmosphereless planets. This near radial symmetry in late-stage excavation has been exploited in the so-called Z-model (Maxwell, 1977; Orphal, 1977). In this scheme, the flow field may be described in terms of a radial velocity

$$u_r = \alpha(t)\ r^{-Z} \tag{1.2}$$

where Z is a small number of order unity (the shape parameter) and α is a function of time (the intensity parameter), determinable by requiring energy conservation of the cratered region as a whole. Although originally conceived as centered at the initial contact point on the target surface, the Z-model flow field may be better represented by an origin on the order of one projectile diameter below the contact point (Thomsen *et al.*, 1979).

FIGURE 2: Four instantaneous views of the excavation stage, after Gault *et al.*(1968), Maxwell (1977), and Melosh (1980). The shock front and flow field velocity vectors are denoted by double lines and arrows respectively. Meteorite remains are indicated by dark lining of the crater surface. Growth of the transient cavity is nearly hemispherical with material in roughly the upper one-third of the crater being ejected. Eventually maximum dynamic depth is reached, but lateral expansion (shearing along the crater wall) continues. Stagnation of the entire crater flow results in the classic bowl shape, raised rim, and overturned flap of ejecta.

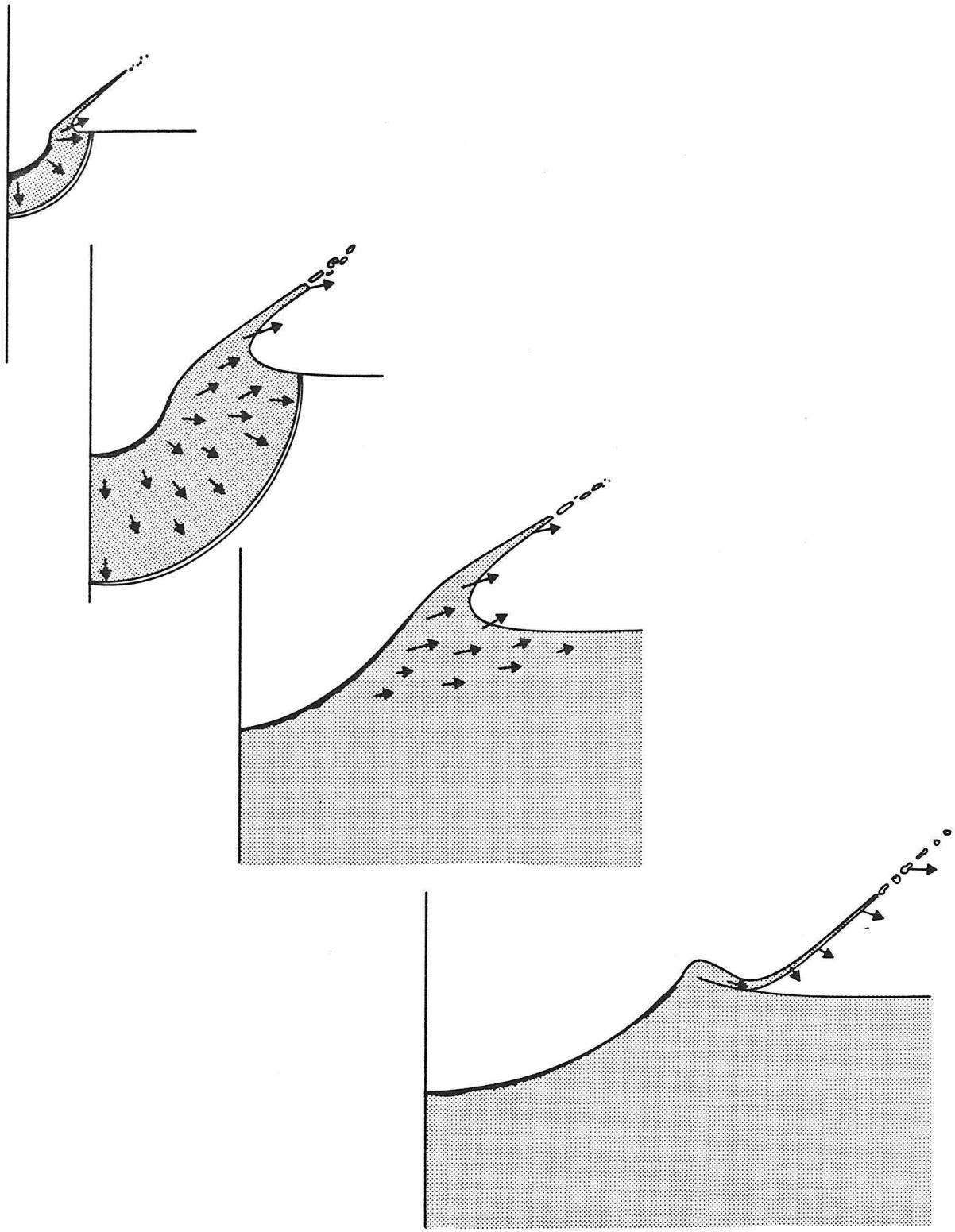

The applicability of such a simple analytic model is based on the fact that (1) most of the late stage excavation of the crater occurs well behind the propagating ground shock(s) and (2) the flow field initiated by the impulsive stresses is approximately steady-state and incompressible (Maxwell and Seifert, 1974; Maxwell, 1977; Cooper, 1977; Orphal, 1977). Obviously the excavation stage cannot go on forever. The original shock decays in amplitude as it diverges. In addition, it is weakened by rarefactions merging with it. As the shock speed declines to trans-sonic values, elastic precursors "smear out" the pressure and particle velocity jump, transforming the shock wave to a "plastic wave." Eventually pressures decline into the elastic regime. Power law decay rates for the shock have been estimated by a variety of analytical, numerical, and geologic methods (Gault and Heitowit, 1963; Ahrens and O'Keefe, 1977; Dence, *et al.*, 1977; Robertson and Grieve, 1977). Under a variety of conditions, they range from $r^{-1.6}$ to $r^{-5.5}$.

The transient cavity continues to grow in a nearly hemispherical manner until a maximum dynamic depth is reached. Expansion continues laterally, "shearing" material from the crater wall (Orphal, 1977; Piekutowski, 1977). Observations of terrestrial impact structures formed in crystalline rocks (Dence *et al.*, 1977) associate this depth with peak shock pressures in the 15-30 GPa (150-300 kbar) range. It is clear that the ultimate limitation on the size and shape of the crater is the conversion of flow field kinetic energy to distortional energy (as the materials resist further shear deformation) and gravitational potential energy.

The flow only remains hydrodynamic as long as the stagnation pressure ρu^2 (where $\rho \equiv$ density and $u \equiv$ the velocity of cratered materials) is much greater than either a representative *post-shock* yield strength Y or $\rho g \ell$ (where $g \equiv$ local acceleration of gravity and ℓ is a relevant distance scale) corresponding to Cauchy or Froude scaling (Maxwell and Seifert, 1974; Melosh, 1980). Material propelled outward from the transient crater lip forms a conical ejecta sheet opening outward to the void. The ejection angle remains remarkably constant during cavity growth, with 35-55° from the horizontal bracketing laboratory impact results (Stöffler *et al.*, 1975; Oberbeck and Morrison, 1976). Eventually the last material lofted stagnates at the transient crater rim and the ejecta blanket overrides it, forming an overturned flap (Shoemaker, 1962). The excavation stage is schematically illustrated in figure 2.

Final crater dimensions are typically one to two orders of magnitude greater than that of the original projectile. As late stage excavation velocities are comparatively low, the timescale for excavation is many orders of magnitude longer than compression. At the laboratory scale a 10 cm crater may form in 10^{-1} sec with compression lasting $\sim 1\,\mu$sec. The resulting ratio of timescales is 10^5 (Gault, 1968). Formation time had been assumed to scale linearly with diameter (Cooper, 1977), but laboratory impact experiments indicate that it grows only as the square root of the diameter (Gault and Wedekind, 1977). Thus a 1 km crater may form in $\sim$ 10 sec, and a 100 km crater in $\sim$ 100 sec. An increase in gravity would

FIGURE 3: A schematic overview (rich in physics) of phenomena associated with the formation of an approximately 1 km diameter crater as a function of time and pressure. The scaling of impact velocity to peak pressure is indicated on the ordinate. Note that the *excavation* stage dominates crater formation in terms of total time. By late stage excavation, pressures are quite low (10^2 kPa ≡ 1 bar).

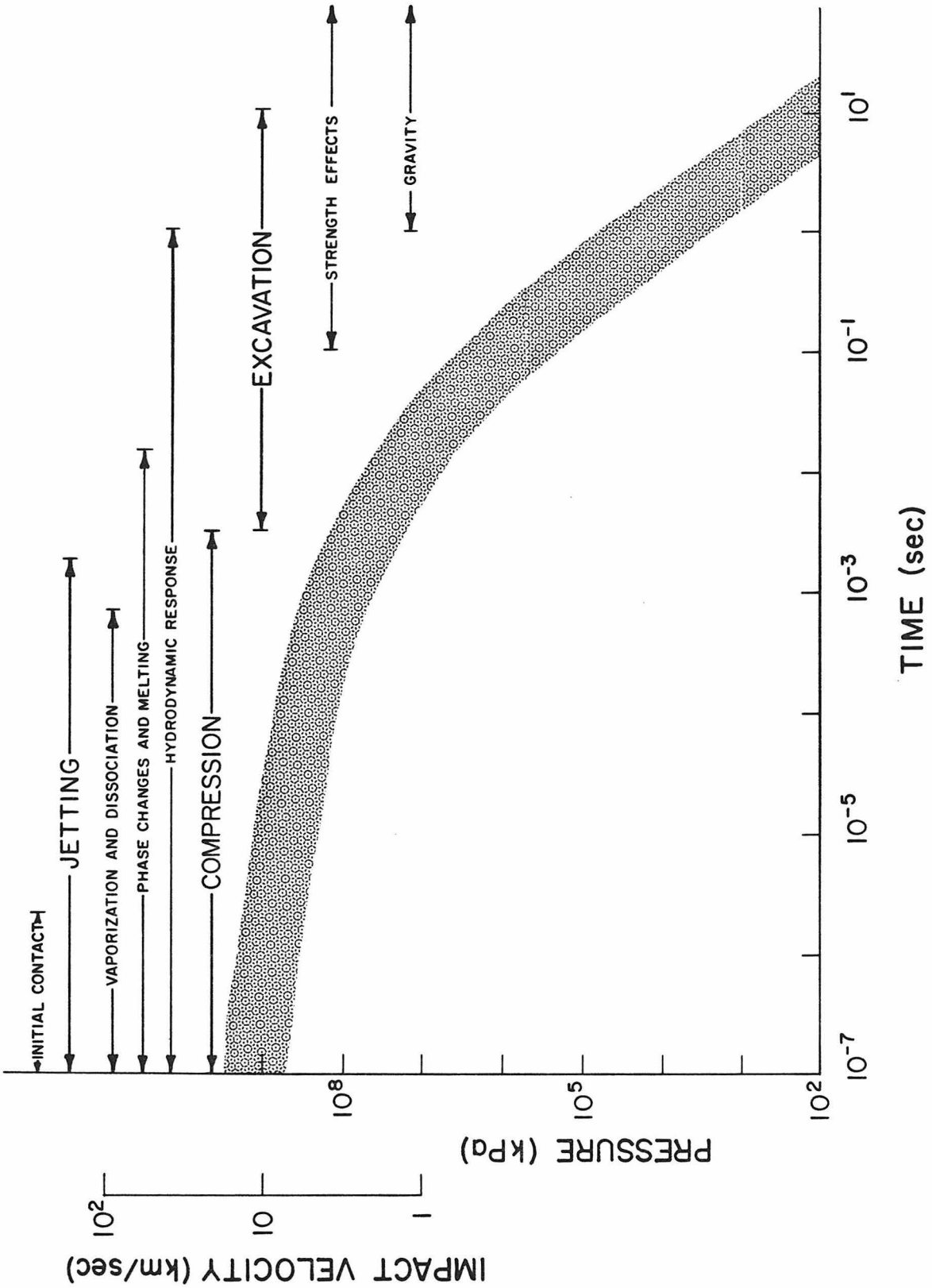
INITIAL CONTACT
JETTING
VAPORIZATION AND DISSOCIATION
PHASE CHANGES AND MELTING
HYDRODYNAMIC RESPONSE
COMPRESSION
EXCAVATION
STRENGTH EFFECTS
GRAVITY
IMPACT VELOCITY (km/sec)
10^2
10
1
PRESSURE (kPa)
10^8
10^5
10^2
10^{-7}
10^{-5}
10^{-3}
10^{-1}
10^1
TIME (sec)

render excavation more difficult, resulting in smaller craters and shorter timescales. Schmidt (1980) shows that cratering efficiency declines drastically with increasing gravity or scale for very large craters.

Figure 3 depicts the relevant pressures, impact velocities, and cratering phenomena as a function of timescale for an approximately 1 km diameter crater. While schematic, it summarizes aspects of the above discussion. The simple crater formed is bowl shaped, with a raised rim and an ejecta blanket. The crater shape is due to both ejection of material and (non-recoverable) plastic deformation of the region surrounding the transient cavity. This is not the only final crater shape, however. A peculiar and diverse array of morphologies is to be found, and what is more important, they are correlated with size.

c) Impact Crater Morphology

The simple bowl-shaped crater form is only prevalent at the smallest scales. Figure 4, from Cooper (1977), gives the apparent radius and depth as a function of crater volume. Apparent radii are determined by the intersection of the crater shape and the original ground plane. While smaller than radii measured to the rim crest, the distinction will not be made as the least squares fit may be adjusted. What is striking is that geologic variation notwithstanding, most of the craters are parabolic in profile with a depth to diameter ratio of essentially 0.2. Significant deviations from this occur for those craters formed in wet soils. Above a certain size, the craters have much larger aspect ratio (i.e., diameter/depth). This transitional diameter is $\sim$ 30 m for the Pacific Nuclear Tests and less than 100 m for high explosion trials at the Suffield Experimental Station (Jones, 1977; Roddy, 1977). The high explosion tests also displayed complexities in their floor and rim morphologies which will be examined later.

On the moon, the change in aspect ratio for fresh impact craters occurs near 15 km diameter. Smaller craters are bowl-shaped, with depth/diameter ratios near 0.2. The 3.8 km diameter lunar crater, Mösting C (figure 5), in mare west of Sinus Medii is typical. The floors of such craters are smooth, rubbled, or textured, a term applied to once-molten material. A small flat floor may result from the accumulation of fallback debris and minor landsliding from the steep crater walls. The continuous ejecta field is blocky near the rim crest, becoming hummocky farther away (Schultz, 1974).

FIGURE 4: Apparent crater radius (R) and depth (D) as a function of apparent crater volume (V) for terrestrial explosions in widely varying geologic settings, from Cooper (1977). Shapes are generally paraboloids of revolution. Significant deviations occur for those craters formed in wet media.

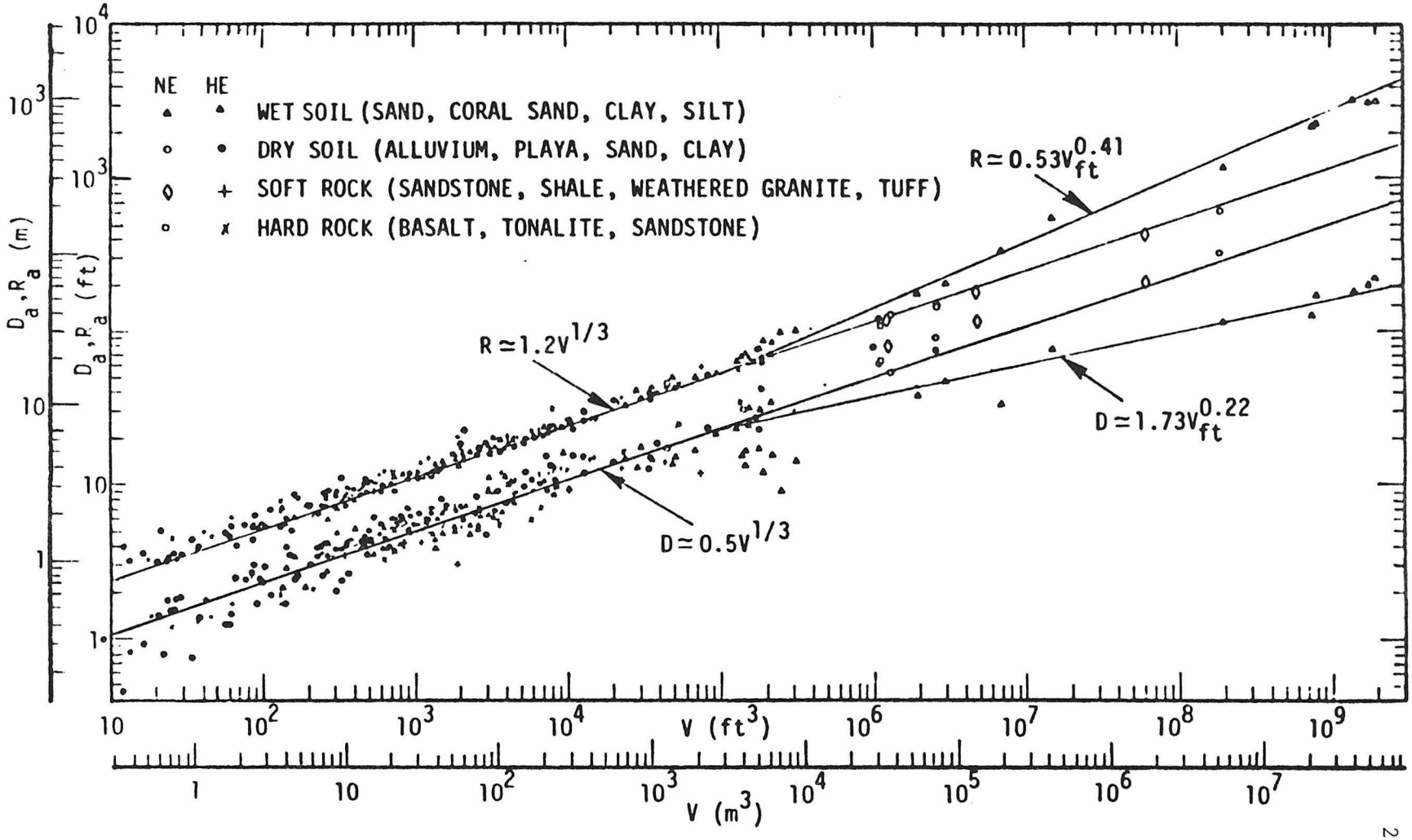
NE HE
WET SOIL (SAND, CORAL SAND, CLAY, SILT)
DRY SOIL (ALLUVIUM, PLAYA, SAND, CLAY)
SOFT ROCK (SANDSTONE, SHALE, WEATHERED GRANITE, TUFF)
HARD ROCK (BASALT, TONALITE, SANDSTONE)
R ≃ 1.2V^1/3
R ≃ 0.53V_ft^0.41
D ≃ 0.5V^1/3
D ≃ 1.73V_ft^0.22
D_a, R_a (m)
D_a, R_a (ft)
V (ft^3)
V (m^3)

FIGURE 5: Mösting C, a fresh 3.8 km diameter crater formed in the lunar mare, exhibits all the salient morphological characteristics of the simple crater: smooth bowl shape, blocky inner rim, hummocky continuous ejecta surrounded by discontinuous ejecta patches and secondary craters, and bright ray material. *Lunar Orbiter photograph III-113-M.*

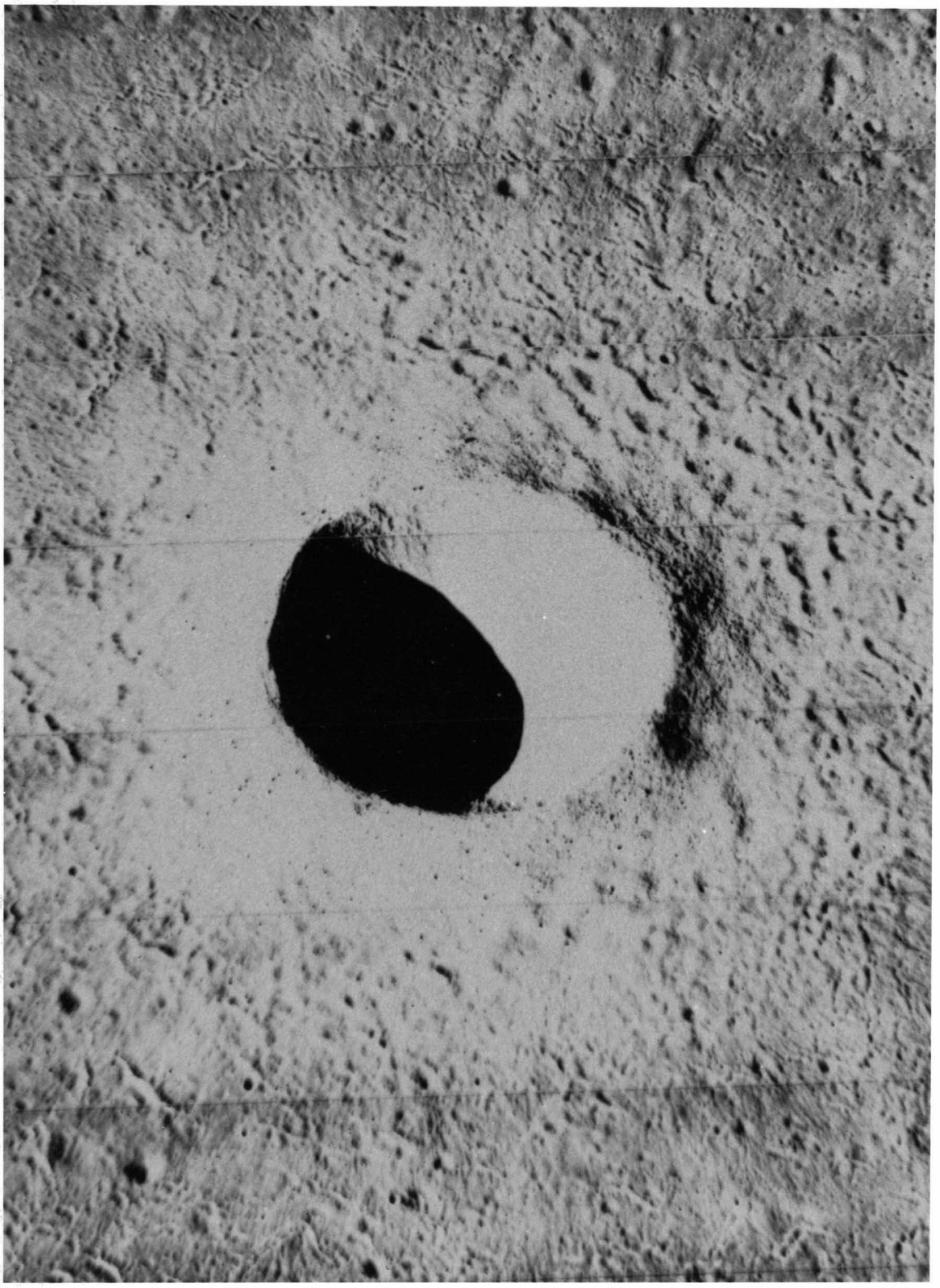

The continuous ejecta eventually gives way to discontinuous ejecta and secondary impacts. Crater depths above 15 km diameter remain remarkably constant, between 3 and 5 km, as is seen in the data of Pike (1974), reproduced in figure 6. A number of other quantitative shape parameters change over the 10-30 km diameter range. These include rim height/diameter, outer rim (or flank) width/diameter, floor diameter/crater diameter, inner (or rimwall) slope, and circularity and profile evenness of the rimcrest (Pike, 1977). These changes reflect the distinct geological modification of the crater form, whose size dependence has been well-documented (Gilbert, 1893; Quaide *et al.*, 1965; Smith and Sanchez, 1973; Howard 1974; Pike, 1977). Rimwall slumps and central peaks appear simultaneously in the diameter range 10-20 km. Dawes, an 18 km diameter crater in Mare Tranquilitatis, figure 7, is scalloped in outline, probably due to the collapse and landsliding of wall materials to form a hummocky floor of debris (so-called "swirl texture") and a "central peak" (Schultz, 1976).

Flat hummocky floors become increasing characteristic above 20 km in diameter. The rimwall slumps become a wreath of terraces whose complexity and size grow with increasing diameter. The floor surface is textured, attesting to a previously molten state. Smooth-surfaced pools of solidified melt and leveed flow channels are found on the slumped walls and rim units beyond (Schultz, 1976). Theophilus, a 95 km diameter crater formed in the lunar highlands near Mare Nectaris, is seen in an oblique view in figure 8. The

FIGURE 6: Depth of fresh lunar craters as a function of rim diameter, determined photogrammetrically by Pike (1974). The relation inflects near 15 km diameter and may be viewed as two distinct populations. The depths of large lunar craters are restricted, lying between 3 and 5 km. From Melosh (1977).

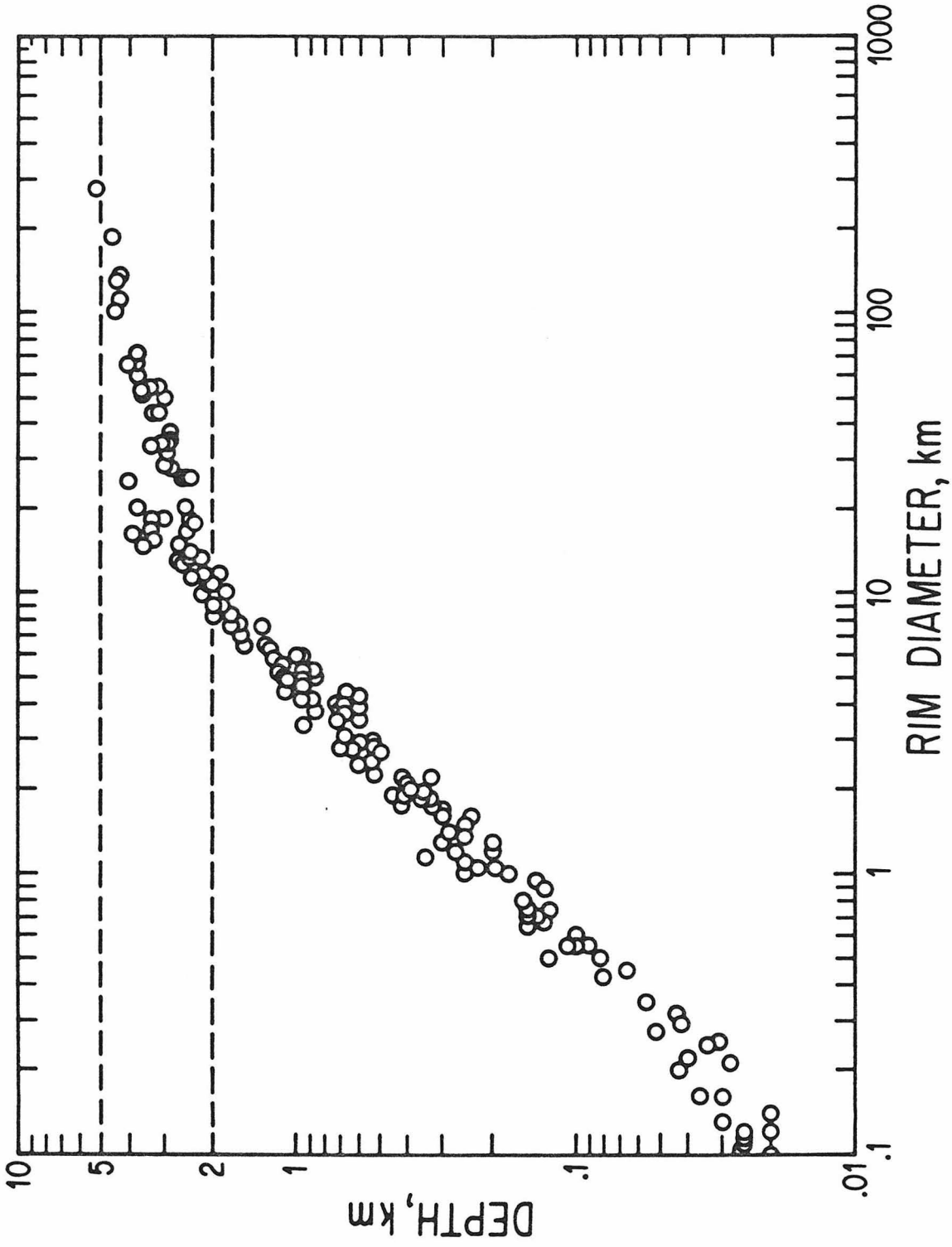
DEPTH, km
10
5
2
1
.1
.01
.1
1
10
100
1000
RIM DIAMETER, km

FIGURE 7: Dawes, a fresh 18 km diameter crater in northern Mare Tranquilitatis, is morphologically characteristic of craters in the 15-20 km range. The scalloped rim and undulating flat floor are indicative of collapse and landsliding. The low "central peak" may reflect the coalescence of toes of slumped material. High sun angle photos reveal patterns of debris draining down the crater wall. *Lunar Orbiter photograph V-070-M.*

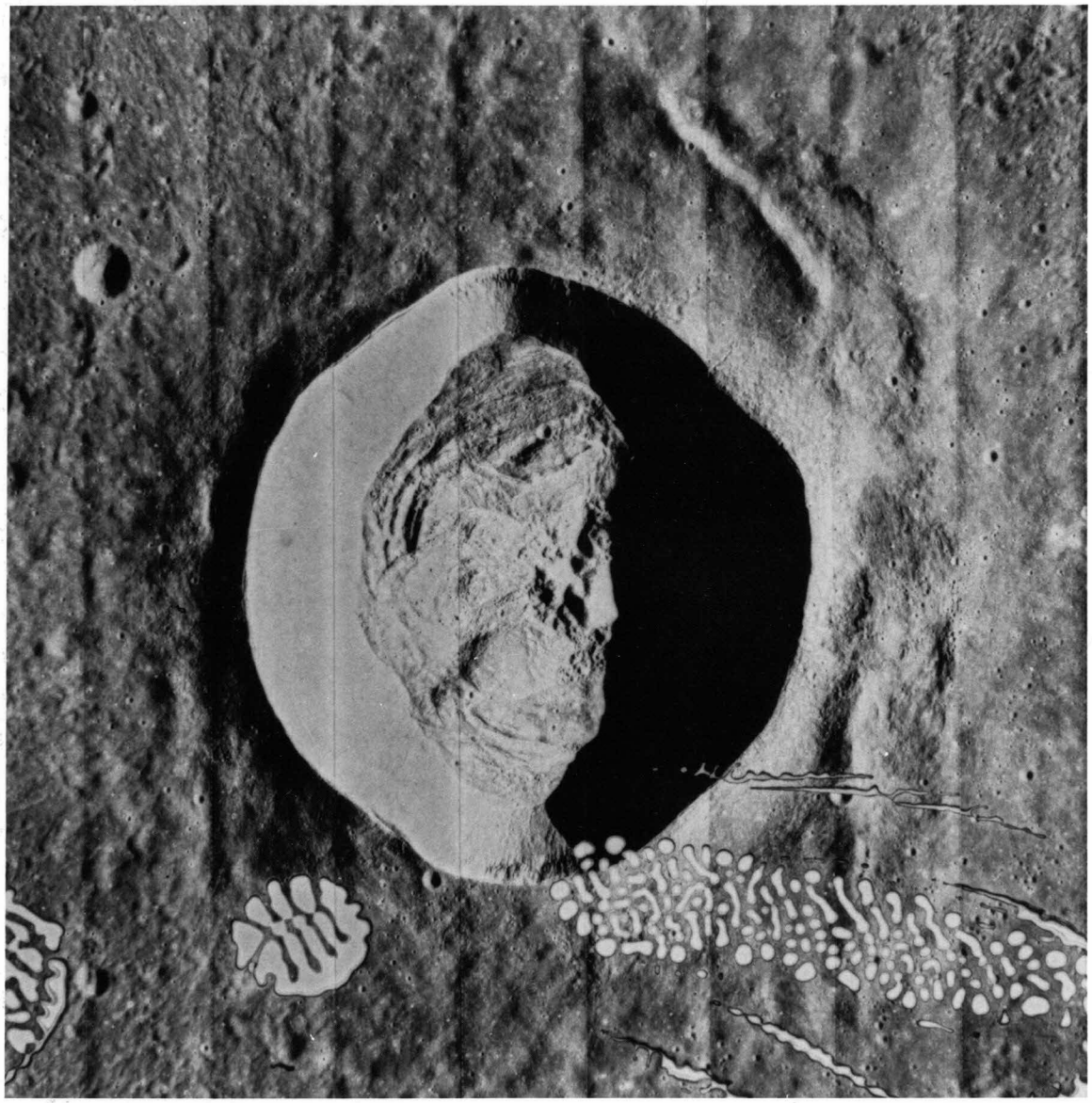

prominent central peak is typical of craters this size. At greater scales (> 100 km) , the central peak declines in significance and one or more concentric mountain rings or scarps may develop. This is the realm of the multiringed basin and its consideration will be deferred to Chapter 3.

A similar scale dependent sequence of morphologies is seen on Mercury. Figures 9 and 10 depict fresh mercurian craters reminiscent of Mösting C, Dawes, and Theophilus. In figure 9, a slump-shallowed 14 km diameter crater is superposed upon the rim of a larger more degraded impact structure. Several smaller fresh craters can be observed in the frame. In figure 10, the 93 km diameter Brahms displays a well-developed central peak complex and terrace wreath. The depth/diameter relation for fresh mercurian craters is a matter of some dispute. Initial analysis by Gault *et al.* (1975) described a "kink" in the relation similar to that for the moon (see figure 6), but occurring at a factor of two smaller diameter. Re-analysis (Malin and Dzurisin, 1977; Malin and Dzurisin, 1978) proclaimed the relation to be essentially identical. However, if the data are examined (figure 11), four points can be made. (1) The mercurian data set exhibits significantly more scatter. (2) Regardless, the population inflects somewhat below 10 km diameter. (3) The bulk of the mercurian craters larger than 10 km diameter are shallower than their lunar counterparts. And (4) the deepest craters on Mercury are deeper than those on the moon.

FIGURE 8: Theophilus, 95 km in diameter, displays a wide "wreath" of slump terraces, a flat floor, and well-developed central peak complex. Smooth-surfaced pools, comprised (at least in part) of once-molten country rock, on the inner and outer rim attest to the rapidity of structural modification of large impact craters. *Lunar Orbiter photograph III-078-M.*

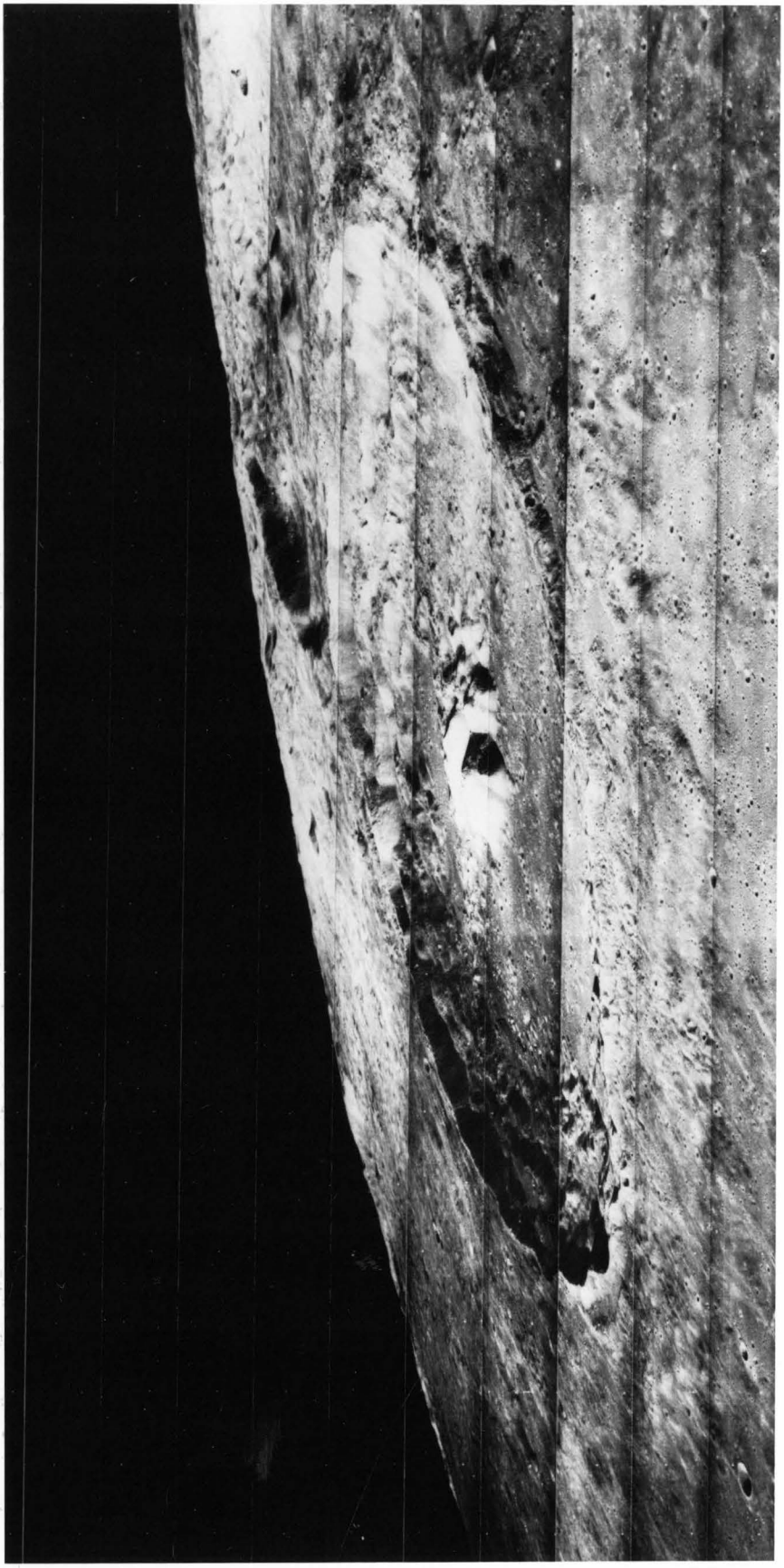

FIGURES 9 AND 10: Fresh impact craters on Mercury follow the same morphological sequence as those on the moon. Fig. 9, a high-resolution view of *heavily cratered terrain* east of Homer, reveals a slumped 14 km diameter crater superposed on a larger, older impact, and several small bowl-shaped craters. The interior structure of Brahms (fig. 10), 93 km across and formed in the *smooth plains* NNE of Caloris, is smiliar to lunar craters of the same size class (e.g., Theophilus, Copernicus). *Mariner 10 frames FDS 27475 and FDS 80* (orthographic projection).

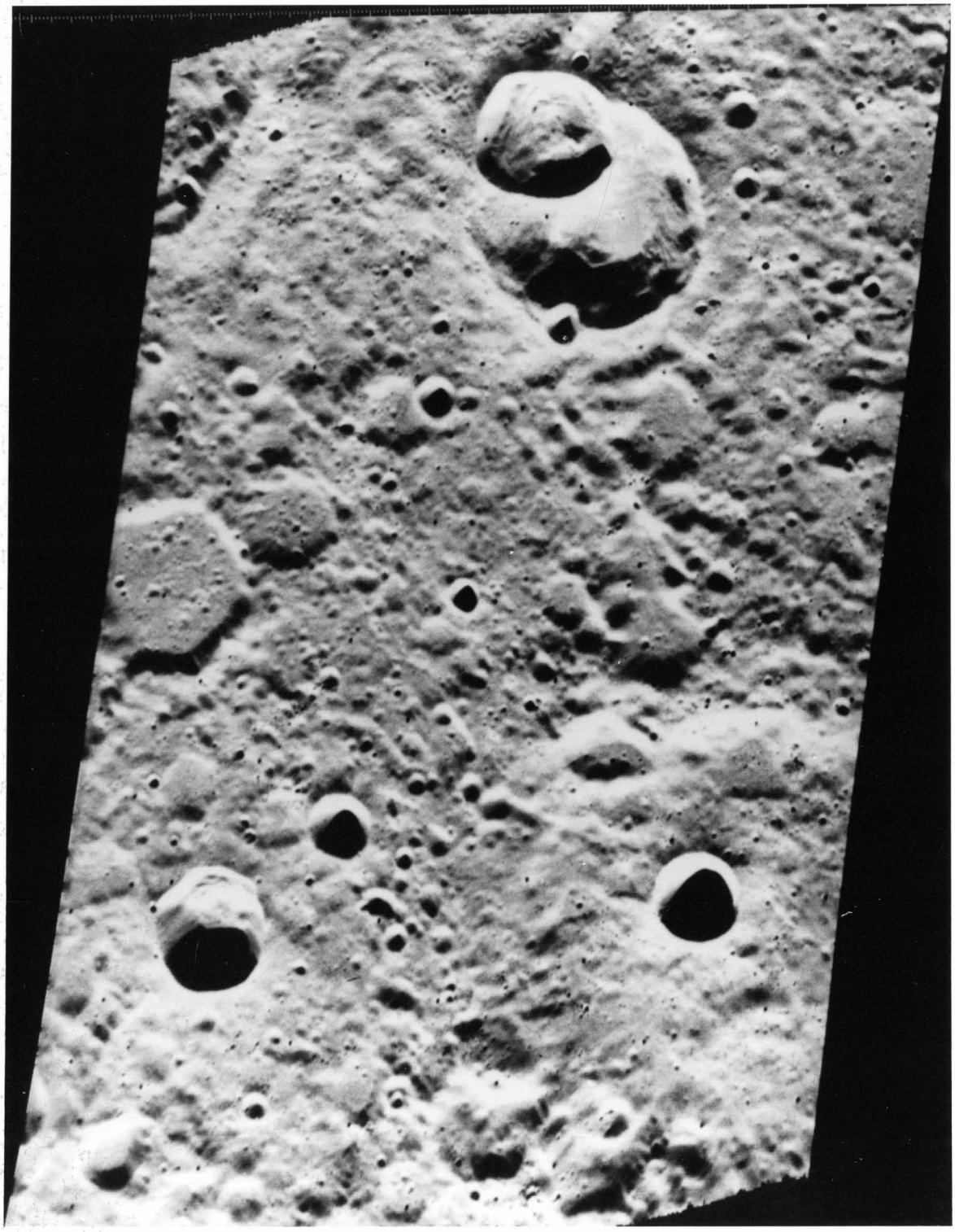

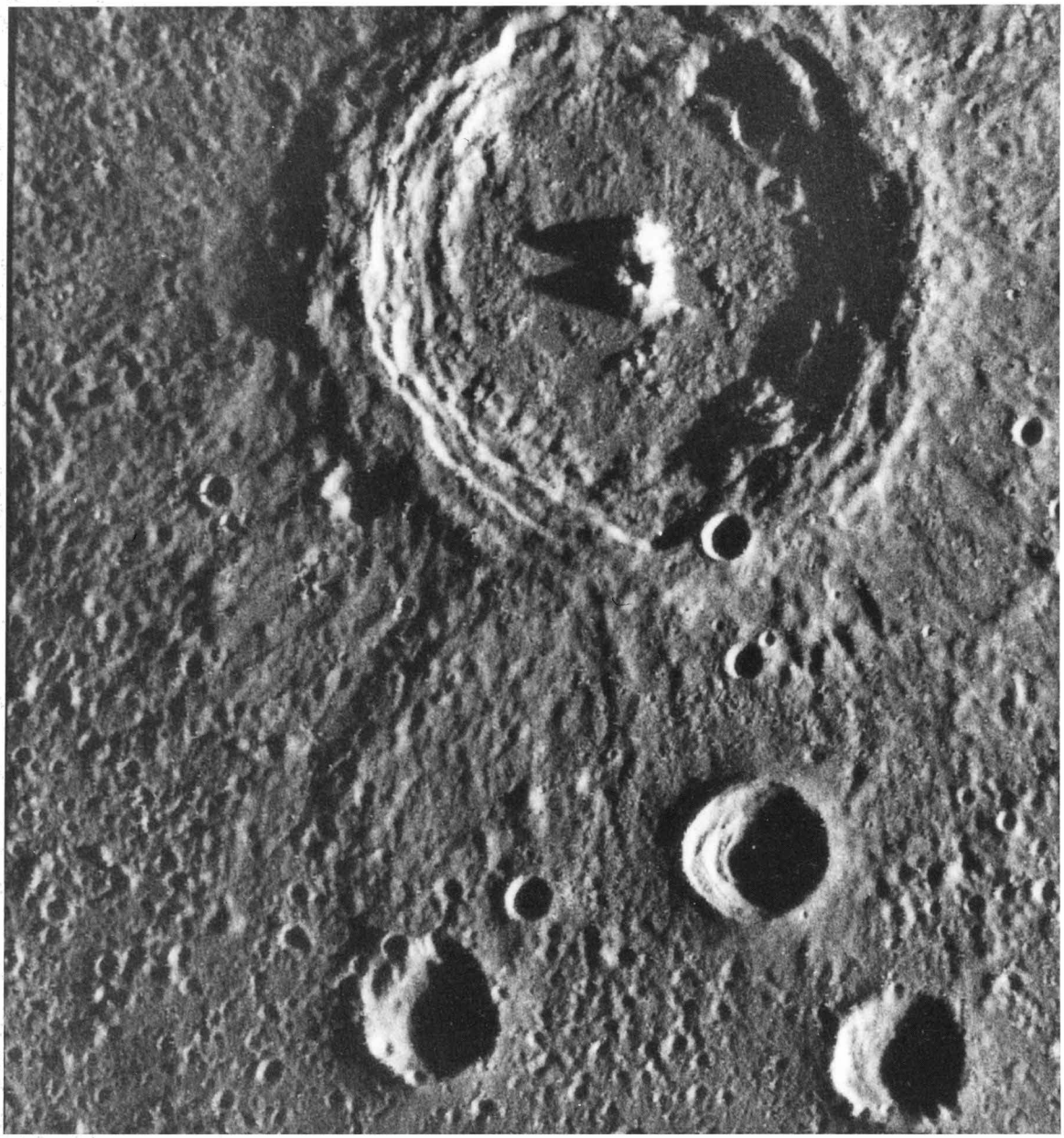

In figure 6, several lunar craters larger than 10 km diameter appear to be an extension of the small crater population (thus preserving the 0.2 depth/diameter ratio). A similar small subset is evident in fig. 11, extending to greater depths than on the moon. Considering the remaining craters above 10 km diameter as those that have been shallowed removes some of the scatter. Malin and Dzurisin (1978) point out that the anomalously deep mercurian and lunar craters display none of the telltale modification morphologies (i.e., terraces and central peaks). Power law fits to the small and large crater populations in fig. 11 intersect between 7 and 10 km diameter. The lunar populations, considerably less noisy, intersect near 11 km. The large mercurian craters are, on the average, 20-30% shallower than large lunar craters. The kinks in the depth/diameter relations for the two planets also differ by this same factor.

The occurrence of central peaks, slumping, and terrace formation on Mercury, as a function of crater diameter, has also received some attention (Gault *et al.*, 1975; Cintala *et al.*, 1977; Malin and Dzurisin, 1978; Smith and Hartnell, 1978; Cintala, 1979). There is no agreement between these authors as to "onset" or median occurrence diameters for the various structures. The difference between the quantitative, such as measuring depths and diameters, and qualitative photogeological evaluations is apparent. It has been variously claimed that the morphological transitions on the moon and Mercury occur over nearly the same diameter ranges or that the ranges on Mercury are up to a factor of two less. However, it is clear from all the data sets that the transitions on Mercury occur at somewhat smaller diameters.

FIGURE 11: Depth of fresh mercurian craters as a function of rim diameter, determined from shadow-length measurement by Malin and Dzurisin (1977). While exhibiting greater scatter, the relation is similar to that for the moon (fig. 6). Differences include inflection at a smaller diameter and shallower large crater depths.

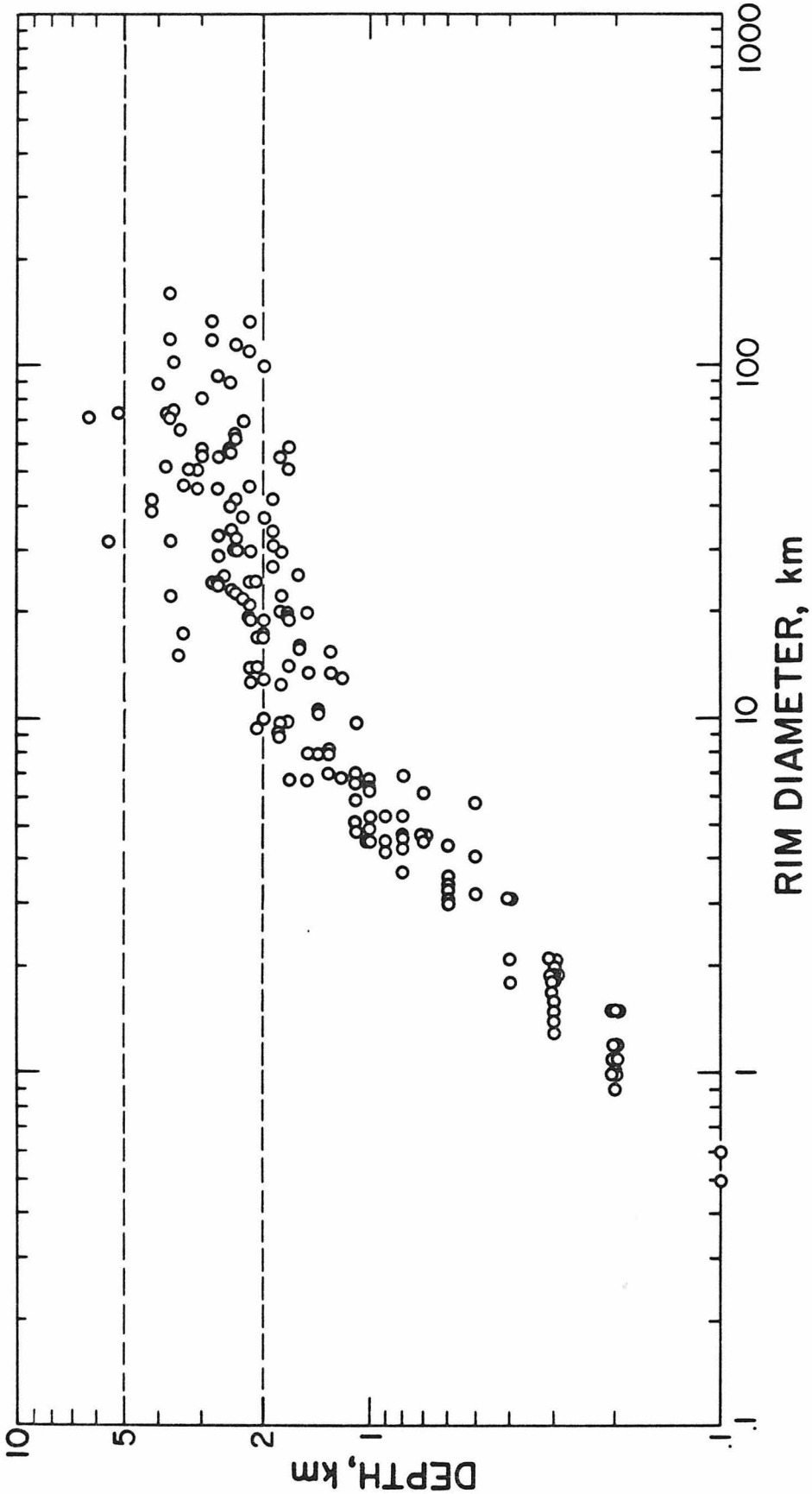
DEPTH, km
10
5
2
1
.1
.1
1
10
100
1000
RIM DIAMETER, km

No systematic variation of the lunar depth/diameter relation for upland craters from that of postmare craters is indicated (Pike, 1974). There is similarly no detectable difference between mercurian craters formed in *smooth plains* or in *heavily cratered terrain* with regard to this matter (Gault *et al.*, 1975; Malin and Dzurisin, 1977). In addition, the seven morphometric quantities of Pike (1977) show no terrain correlation for the moon. Indeed, the only observable correlation with intraplanet geologic setting concerns the degree of central peak formation and the mode of wall failure in upland and postmare craters on the moon. Both the development of the peaks and the transition from smaller wall slumps (or scallops) to more concentric terracing occur at slightly greater diameters (approximately 10 km greater) in highland terrains (Cintala *et al.*, 1977; Smith and Hartnell, 1978). Fresh lunar craters situated on the rim flanks of older impacts exhibit terrace formations at anomalously small diameters compared to either highland or postmare craters. Terracing and slumping for these craters also occurs preferentially in the direction of local topographic highs, i.e., the older crater rims (Gifford and Maxwell, 1979).

Photogeologic studies of the moon and Mercury form the core data for this work as they retain the most studied, least degraded assemblage of impact craters. Complimenting this inventory is the fact that these two bodies are *relatively* geologically uncomplicated. The data set for Mercury could no doubt be refined in terms of resolution and areal coverage, but this would require an orbital mission.

Data from Mars, the earth, and other heavenly bodies will be considered supplemental. Pre-Viking statistics are unreliable due to a combination of resolution and degradation effects, coupled with technique biases (Cintala, 1977). Preliminary analysis of Viking photographs, though, has determined that the transition from bowl shaped to flat floored craters occurs over a diameter range of 4-5 km (Carr *et al.*, 1977), and that the development of slumps, terraces, and central peaks takes place between 5-15 km diameter, depending on terrain (Wood *et al.*, 1978). Some martian impact craters also display peculiar ejecta patterns (Carr *et al.*, 1977) and "central pits" (Smith, 1976; Hodges, 1978; Wood *et al.*, 1978), but as they have no lunar or mercurian counterparts, they will not be discussed further.

Terrestrial impact structures are relatively few in number, and with some notable exceptions, deeply eroded. Nevertheless, the transition from simple to complex craters occurs between 1.5-2 km diameter for craters formed in competent sedimentary strata and at approximately 4 km for those formed in crystalline rock (Dence *et al.*, 1977). Complex in this instance denotes the presence of a central uplift, which can usually still be detected even in severely eroded structures.

Examination of Viking images of Deimos and Phobos (Veverka and Duxbury, 1977; Duxbury and Veverka, 1978) does not reveal any fresh impact craters with slump features or central peaks. While no evidence of morphological transition exists, it should be borne in mind that the 10 km diameter Stickney on Phobos is the largest crater on either body. Voyager images of Almathea have permitted the

identification of three large craters, and an estimate of the dimensions of one of them (Veverka *et al.*, 1980). This crater, with a diameter and depth of 70 and 12 km respectively, represents for its size the deepest crater yet discovered in the solar system.

Photogeologic studies of the craters on Ganymede and Callisto will no doubt soon be available for our edification, as will eventually be data from Venus, and the Saturnian and Uranian satellite systems.

d) Mechanisms of Simple Crater Modification

The morphological transition of fresh lunar craters has been held to be indicative of gravitationally induced mechanical instability (Gilbert, 1893; Shoemaker, 1962; Quaide *et al.*,1965; Gault *et al.*, 1968; Gault *et al.*, 1975). The direct correspondence of the kink in the depth/diameter curve with the appearance of wall slumps and central peaks centainly implies a causal link. Both the formational and gravitational potential energy of a fresh bowl shaped crater scale with crater size. That a gravitational threshold is being crossed is a photogeological evaluation, as the wall slumps and terraces found in impact craters bear a striking resemblance to the collapse of cohesive slopes and cliffs (Mackin, 1969). When lunar crater slumps and terraces are restored to their original "uncollapsed" positions, the change in the depth/diameter relation (at least for craters of 10-50 km diameter) is seen to be directly attributable to this gravitative adjustment (Malin and Dzurisin, 1978; Settle and Head, 1979). The implication is clear. Before the formation of slumps and terraces, the crater reaches a transient parabolic form with a depth/diameter ratio similar to that of small craters, i.e., approximately 0.2. Above 50 km diameter, the restoration becomes less sure, but the authors suggest that transient crater growth may become non-proportional.

Central peak formation appears linked to crater collapse. Their origin remains undetermined, however, as they are not generally associated with the more traditional terrestrial slump processes. It has been suggested that the toes of the more deep seated slumps (and terraces) meet near the crater center, thrusting up a central peak (Shoemaker, 1962;

Quaide *et al.*, 1965; Dence, 1968). Formation may be linked to the early-time flow field of the excavation stage. While shallowly buried charges best simulate hypervelocity impact crater formation (Quaide and Oberbeck, 1968; Oberbeck, 1971; Oberbeck, 1977), some zero depth-of-burst and surface tangent explosion trials have produced central uplifts (Milton and Roddy, 1972; Jones, 1977; Roddy, 1977). Presumably placing the effective center of energy deposition at or above the free surface alters the shock wave geometry such that the rarefaction stage not only imparts an upward and outward component to the cratering flow field as described in section 1b, but actually reverses the downward motion along the crater symmetry axis. A finite element attack on this problem (Ullrich, 1976; Ullrich *et al.*, 1977) supports this interpretation, but unfortunately remains the only study of its kind due to complexity and cost. This type of flow field, differing markedly from the Z-flow model, is termed toroidal flow.

The applicability of toroidal flow to planetary impact central peaks is problematical. Only low density objects, such as comets, could possibly fulfill the effective depth-of-burst criterion, as they would volatilize during the compression phase. Such a cometary origin for central peaks has been suggested (Roddy, 1968; Milton and Roddy, 1972; Roddy, 1977). This mechanism is not dependent on crater size, however. Nor can all planetary impacts be cometary, as central peaks eventually reach 100% occurrence levels for the moon, Mercury, Mars, and the earth (Carr *et al.*, 1977; Cintala *et al.*,

1977; Dence *et al.*, 1977; Smith and Hartnell, 1978). In addition, finite element calculations for the hypervelocity impact of "water ice" projectiles into anorthosite (O'Keefe and Ahrens, 1980) do not result in toroidal flow unless the projectile density is less than 0.1 g/cm^3. However, changes in impact crater morphology due to local geologic setting cannot be ignored (Shoemaker, 1963; Gault *et al.*, 1968).

Toroidal flow probably represents the best approximation to what has been loosely termed "rebound" or "elastic recoil," a phrase again attributable to Gilbert (1893). This rebound is formally part of the crater excavation stage. If "elastic recoil" is defined as the elastic contribution to crater modification, its influence is marginal. Impact seismic efficiencies have been estimated between 10^{-3} and 10^{-5} (Schultz and Gault, 1975), with most of the elastic energy concentrated in the elastic remnant of the initial ground shock. This energy is quite distant from the crater at the end of the excavation stage.

Zero or negative depth-of-burst will not insure central uplift development. Pre-Mine Throw IV Crater 6, a 100 ton surface tangent nitromethane sphere detonated on Yucca Lake playa did not result in an uplift (Roddy, 1977), while the Snowball explosion crater, formed in layered alluvium by a 500 ton TNT hemisphere lying on the surface did (Jones, 1977; Roddy, 1977). One principal difference between the two was the presence of a water table for the Snowball test, located at a depth of 7m. It is suggested that the reduced strength of saturated sediments, fluidized by the explosion, also favors central uplift formation. Fluidization combined with centripetal collapse

driven by gravity could form peaks via hydrodynamic oscillation (Gilbert, 1893; Scott, 1967; Dence and Grieve, 1979), but only if sufficient damping were available to preserve the uplift.

A central mound or peak is observed in laboratory impact and explosive cratering experiments which involve an unconsolidated layer overlying a competent "basement," typically quartz sand and cement, respectively (Quaide and Oberbeck, 1968; Oberbeck, 1977; Pieukutowski, 1977). This occurs for those craters for which the excavation depth is just comparable to the unconsolidated layer thickness. The crater bottoms out at the layer interface, but a small pile of sand remains at the center, due to stagnation of the cratering flow field. Slight increases in the crater size eliminate the peak. This morphological transition has proved useful in determining regolith thickness on the moon (Quaide and Oberbeck, 1968), but it is not applicable to the general problem as terrestrial impact crater central peaks show, without exception, characteristic uplifts in the form of thrust faults and/or anticlinal folding (Milton and Roddy, 1972; Dence *et al.*, 1977).

A first principle calculation of an impact cratering event, from initial contact through the last ground motions is well beyond the present state-of-the-art. Therefore an intuitive severing of the modification stage from the excavation stage is applied in Chapter 2, in which theoretical mechanical analysis is applied to the problem of slumping, terracing, and the kink in depth/diameter curves for cratered planetary bodies. Such a procedure is not

absolutely justifiable, but if correctly formulated leads to valid results and insights. Also included in Chapter 2 is a discussion of a preliminary set of crater collapse experiments designed to test the connection between slumping and central peak formation.

e) Long Term Modification

Slumping, terracing, and central peak formation are immediate or short term modifications of the simple crater form. Flat lying sheets and pools of impact melt, formed within terrestrial impact structures (Grieve *et al.*, 1977) and superposed on lunar crater floors, walls and rims (Howard and Wilshire, 1975; Schultz, 1976) evidently formed and solidified after the structural modifications ceased.

Subsequent modification is myriad in its complexity and diversity. A crater will be transformed, or even erased by further impacts, volcanism, tectonism, aeolian, fluvial, periglacial, or even biological activity. For the moon and Mercury, only the first three are important. Neither planet shows any geomorphological evidence for an ancient atmosphere or hydrous process (Murray *et al.*, 1974). Mars exhibits much greater vigor in all these areas save biology (Schubert *et al.*, 1977).

Subsequent impacts not only possess obliterative capacity due to direct superposition, but also through ejecta deposition and secondary crater formation. Great basin ($\geq$ 200 km diameter) impacts are especially significant in this regard. Their ejecta scours, sculpts, overturns, and reworks vast areas of terrain (Gilbert, 1893; Oberbeck, 1975; Schultz, 1976). The stratigraphy of the lunar highlands may be characterized by consecutive basin ejecta horizons (Howard *et al.*, 1974).

Impact induced seismicity can disrupt crater forms. Antipodal focusing of basin impact seismic energy has been studied as a causative agent for the *hilly and lineated terrains* on the moon and Mercury (Schultz and Gault, 1975) and as a compaction method for crater breccia zones (Dvorak and Phillips, 1978). Less catastrophic seismicity, not necessarily due to impact, probably plays a minor role in initiating downslope movement of loose debris or regolith (Houston *et al.*, 1973).

Volcanic infilling and burial of craters by mare basalt on the moon, lava plains and volcanic constructs on Mars, and by *smooth plains* materials on Mercury is self-evident. While some question mercurian volcanism (Wilhelms, 1976), mostly on the basis of the lack of a returned sample, the evidence is quite compelling (Strom *et al.*, 1975; Trask and Strom, 1976).

In so far as impact, seismic and volcanic modifications have been considered (as well as aeolian, hydrous, and biological contributions, which will not be examined further), the crater acts as a passive victim to the various erosional and constructional forces. What is of greater interest are those long term modifications brought on by the *presence* of the crater. Generally this occurs when the scale of the impact structure makes it necessary to consider the local planetary thermal structure. Proximity to magma sources, or an asthenosphere (a deeper planetary layer that acts as a fluid on a geological timescale) enhances both volcanism and tectonic adjustment. This distinction becomes blurred for planetary crusts warm enough

to allow the crater to viscously deform. Theoretical analysis (Scott, 1967) can be applied to such craters as found in abundance on Ganymede (Smith *et al.*, 1979; Shoemaker and Passey, 1979).

In general, observational and geophysical evidence for viscous relaxation has been lacking for the moon and Mercury. The material that surround these craters is apparently quite rigid, with viscosities in excess of 10^{25} kg $m^{-1}sec^{-1}$ (10^{26} poise) (see Schaber *et al.*, 1977). How deep these viscosities extend is a question of primary importance. Any reasonable temperature gradient will lead to a rapid decrease in viscosity with depth as solid state flow mechanisms are thermally activated (Weertman and Weertman, 1975). This leads to a two-layer rheological approximation, in analogy with highly successful terrestrial studies, of an elastic layer overlying a viscous layer or interior (lithosphere and asthenosphere). Terrestrial viscosities for these layers are near 10^{23} and 10^{19} kg $m^{-1}sec^{-1}$ (10^{24} and 10^{20} poise), respectively.

It is efficient to consider steady state solutions to problems posed in this manner, especially when dealing with the moon or Mercury. Viscous transients can thus be ignored and the planetary interior can be treated as fluid. The isostatic response of such a floating elastic lithosphere to negative and positive central loading has been examined (Melosh, 1976; Melosh, 1978; Solomon and Head, 1979). Predictions of such analyses have been quite successful in relating such observables as surface deformation (flexure), tectonic style (fault expression), gravity anomalies, and magma release patterns for lunar mare basins. Chapter 4 is an analysis

of Caloris Basin, Mercury, a 1300 km diameter structure possessing a vast province of central extension unique among solar system basins. This extension, the final tectonic episode for Caloris (Strom *et al.*, 1975), is shown to be related to the emplacement of *smooth plains* in a wide annulus around the basin, leading to constraints on mercurian lithospheric thickness and thermal history.

This study of Caloris serves only as an example of long term crater modification. Further detailed consideration of all the processes that a planetary crust is heir to will not be attempted here. Analyzed or not, long term modification of craters will continue across the fullness of time.

REFERENCES

Ahrens, T.J., and O'Keefe, J.D. (1977). Equations of state and impact-induced shock-wave attenuation on the moon. In *Impact and Explosion Cratering* (D.J. Roddy, R.O. Pepin, and R.B. Merrill, eds.), p. 1245-1260. Pergamon Press, New York.

Bryan, J.B., Burton, D.E., Cunningham, M.E., and Letlis, L.A., Jr. (1978). A two-dimensional computer simulation of hypervelocity impact cratering: Some preliminary results for Meteor Crater, Arizona. *Proc. Lunar Planet. Sci. Conf. 9th*, 3931-3964.

Carr, M.H., Crumpler, L.S., Cutts, J.A., Greeley, R., Guest, J.E., and Masursky, H. (1977). Martian impact craters and implacement of ejects by surface flow. *J. Geophys. Res. 82*, 4055-4065.

Cintala, M.J. (1977). Martian fresh crater morphology and morphometry - a pre-Viking review. In *Impact and Explosion Cratering* (D.J. Roddy, R.O. Pepin, and R.B. Merrill, eds.), p. 575-591. Pergamon Press, New York.

Cintala, M.J. (1979). Mercurian crater rim heights and some inter-planetary comparisons. *Proc. Lunar Planet Sci. Conf. 10th*, 2635-2650.

Cintala, M.J., Wood, C.A., and Head, J.W. (1977). The effect of target characteristics on fresh crater morphology: Preliminary results for the moon and Mercury. *Proc. Lunar Sci. Conf. 8th*, 3409-3425.

Cooper, H.F. (1977). A summary of explosion cratering phenomena relevant to meteor impact events. In *Impact and Explosion Cratering* (D.J. Roddy, R.O. Pepin, and R.B. Merrill, eds.), p. 11-44. Pergamon Press, New York.

Dence, M.R. (1968). Shock zoning at Canadian Craters: petrography and structural implications. In *Shock Metamorphism of Natural Materials* (B.M. French and N.M. Short, eds.), p. 168-184. Mono Book Corp., Baltimore.

Dence, M.R. and Grieve, R.A.F. (1979). The formation of complex impact structures (abstract). In *Lunar and Planetary Science X*, p. 292-294. Lunar and Planetary Institute, Houston.

Dence, M.R., Grieve, R.A.F., and Robertson, P.B. (1977). Terrestrial impact structures: Principal characteristics and energy considerations. In *Impact and Explosion Cratering* (D.J. Roddy, R.O. Pepin, and R.B. Merrill, eds.), p. 247-275. Pergamon Press, New York.

Duxbury, T.C. and Veverka, J. (1978). Deimos encounter by Viking: Preliminary imaging results. *Science 201*, 812-814.

Dvorak, J. and Phillips, R.J. (1978). Lunar Bouger gravity anomalies: Imbrian age craters. *Proc. Lunar Planet. Sci. Conf. 9th*, 3651-3668.

Gault, D.E., Guest, J.E., Murray, J.B., Dzurisin, D., and Malin, M.C. (1975). Some comparisons of impact craters on Mercury and the Moon. *J. Geophys. Res. 80*, 2444-2460.

Gault, D.E. and Heitowit, E.D. (1963). The partition of energy for hypervelocity impact craters formed in rock. *Proc. Sixth Hypervelocity Impact Symp., 2*, 419-456, Firestone Rubber Co., Cleveland, Ohio.

Gault, D.E., Quaide, W.L., and Oberbeck, V.R. (1968). Impact cratering mechanics and structures. In *Shock Metamorphism of Natural Materials* (B.M. French and N.M. Short, eds.), p. 87-99. Mono

Book Corp. Baltimore.

Gault, D.E. and Wedekind, J.A. (1977). Experimental hypervelocity impact into quartz sand - II: Effects of gravitational acceleration. In *Impact and Explosion Cratering* (D.J. Roddy, R.O. Pepin, and R.B. Merrill, eds.), p. 1231-1244. Pergamon Press, New York.

Gifford, A.W. and Maxwell, T.A. (1979). Asymmetric terracing of lunar highland craters: Influence of pre-impact topography and structure. *Proc. Lunar Planet. Sci. Conf. 10th*, 2597-2607.

Gilbert, G.K. (1893). The moon's face; a study of the origin of its features. *Bull. Phil. Soc. Wash. 12*, 241-292.

Grieve, R.A.F., Dence, M.R. and Robertson, P.B. (1977). Cratering processes: As interpreted from the occurrence of impact melts. In *Impact and Explosion Cratering* (D.J. Roddy, R.O. Pepin, and R.B. Merrill, eds.), p. 791-814. Pergamon Press, New York.

Handin, J.A. (1966). Strength and ductility. *GSA Memior 97*, 223-289.

Hodges, C.A. (1978). Central pit craters on Mars (abstract). In *Lunar and Planetary Science IX*, p. 521-522. Lunar and Planetary Institute, Houston.

Houston, W.N., Moriwaki, Y., and Chang, C.S. (1973). Downslope movement of lunar soil and rock caused by meteoroid impact. *Proc. Lunar Sci. Conf. 4th*, 2425-2435.

Howard, K.A. (1974). Fresh lunar impact craters: Review of variation with size. *Proc. Lunar Sci. Conf. 5th*, 67-79.

Howard, K.A., Wilhelms, D.E., and Scott, D.H. (1974). Lunar basin formation and highland stratigraphy. *Rev. Geophys. Space Phys. 12*, 309-327.

Howard, K.A. and Wilshire, H.G. (1975). Flows of impact melt at lunar craters. *J. Res. U.S. Geol. Survey 3*, 237-251.

Jeanloz, R. and Ahrens, T.J. (1979). Release adiabat measurements on minerals: The effect of viscosity. *J. Geophys. Res. 84*, 7545-7548.

Jones, G.H.S. (1977). Complex craters in alluvium. In *Impact and Explosion Cratering* (D.J. Roddy, R.O. Pepin, R.B. Merrill, eds.), p. 163-183. Pergamon Press, New York.

Krinov, E.L. (1960). *Principles of Meteoritics*, translated by I. Vidziunas. Pergamon Press, New York. 535 pp.

Mackin, J.H. (1969). Origin of lunar maria. *Geol. Soc. America Bull. 80*, 735-748.

Malin, M.C. and Dzurisin, D. (1977). Landform degradation on Mercury, the moon, and Mars: Evidence from depth/diameter relationships. *J. Geophys. Res 82*, 376-388.

Malin, M.C. and Dzurisin, D. (1978). Modification of crater landforms: Evidence from the moon and Mercury. *J. Geophys. Res. 83*, 233-243.

Maxwell, D.E. (1977). Simple Z model of cratering, ejection, and the overturned flap. In *Impact and Explosion Cratering* (D.J. Roddy, R.O. Pepin, and R.B. Merrill, eds.), p. 1003-1008. Pergamon Press, New York.

Maxwell, D.E. and Seifert, K. (1974). Modeling of cratering, close-in displacement, and ejecta. *Report DNA 3628F*, Defense Nuclear Agency, Washington, D.C., 106 pp.

Melosh, H.J. (1976). On the origin of fractures radial to lunar basins. *Proc. Lunar Sci. Conf. 7th*, 2967-2982.

Melosh, H.J. (1978). Tectonics of mascon loading. *Proc. Lunar Planet.*

Sci. Conf. 9th, 3513-3525.

Melosh, H.J. (1980). Cratering Mechanics - Observational, Experimental, and Theoretical. *Ann. Rev. Earth Planet. Sci. 8* (in press).

Milton, D.J. and Roddy, D.J. (1972). Displacements within impact craters. *Proc. 24th Internat. Geol. Congress, Section 15 (Planetology)*, 119-124.

Murray, B.C., Belton, M.J.S., Danielson, G.E., Davies, M.E., Gault, D.E., Hapke, B., O'Leary, B., Strom, R.G., Suomi, V., and Trask, N. (1974). Mercury's surface: Preliminary description and interpretation from Mariner 10 pictures. *Science 185*, 169-179.

Oberbeck, V.R. (1971). Laboratory simulation of impact cratering with high explosives. *J. Geophys. Res. 76*, 5732-5749.

Oberbeck, V.R. (1975). The role of ballistic erosion and sedimentation in lunar stratigraphy. *Rev. Geophys. Space Phys. 13*, 337-362.

Oberbeck, V.R. (1977). Application of high explosion cratering data to planetary problems. In *Impact and Explosion Cratering* (D.J. Roddy, R.O. Pepin, and R.B. Merrill, eds.), p. 45-65. Pergamon Press, New York.

Oberbeck, V.R. and Morrison, R.H. (1976). Candidate areas for *in situ* ancient lunar materials. *Proc. Lunar Sci. Conf. 7th*, 2983-3006.

O'Keefe, J.D. and Ahrens, T.J. (1975). Shock effects from a large impact on the moon. *Proc. Lunar Sci. Conf. 6th*, p. 2831-2844.

O'Keefe, J.D. and Ahrens, T.J. (1980). Cometary impact calculations: flat floors, multirings and central peaks (abstract). In *Lunar and Planetary Science XI*, p. 830-832. Lunar and Planetary Institute, Houston.

Orphal, D.L. (1977). Calculations of explosion cratering II: Cratering mechanics and phenomenology. In *Impact and Explosion Cratering*. (D.J. Roddy, R.O. Pepin, and R.B. Merrill, eds.), p. 489-509. Pergamon, N.Y.

Passey, Q.R. and Melosh, H.J. (1980). Effects of atmospheric break-up on crater field formation. *Icarus* (in press).

Piekutowski, A.J. (1977). Cratering mechanisms observed in laboratory-scale high-explosive experiments. In *Impact and Explosion Cratering* (D.J. Roddy, R.O. Pepin, and R.B. Merrill, eds.), p. 1245-1260. Pergamon Press, New York.

Pike, R.J. (1974). Depth/diameter relations of fresh luner craters: Revision from spacecraft data. *Geophys. Res. Lett. 1*, 291-294.

Pike, R.J. (1975). Size-morphology relations of lunar craters - Discussion. *Mod. Geol. 5*, 169-173.

Pike, R.J. (1977). Size dependence in the shape of fresh impact craters on the moon. In *Impact and Explosion Cratering* (D.J. Roddy, R.O. Pepin, and R.B. Merrill, eds.), p. 489-509. Pergamon, New York.

Quaide, W.L., Gaulet, D.E. and Schmidt, R.A. (1965). Gravitative effects on lunar impact structures. *Annals N.Y. Acad. Sci. 123*, 563-572.

Quaide, W.L. and Oberbeck, V.R. (1968). Thickness determinations of the lunar surface layer from lunar impact craters: *J. Geophys. Res. 73*, 5247-5270.

Robertson, P.B. and Grieve, R.A.F. (1977). Shock attenuation at terrestrial impact structures. In *Impact and Explosion*

Cratering (D.J. Roddy, R.O. Pepin, and R.B. Merrill, eds.), p. 687-702. Pergamon Press, New York.

Roddy, D.J. (1968). The Flynn Creek crater, Tennessee. In *Shock Metamorphism of Natural Materials* (B.M. French and N.M. Short, eds.), p. 291-322. Mono Book Corp., Baltimore.

Roddy, D.J. (1977). Large-scale impact and explosion craters: Comparisons of morphological and structural analogs. In *Impact and Explosion Cratering* (D.J. Roddy, R.O. Pepin, and R.B. Merrill eds.), p. 185-246. Pergamon Press, New York.

Schaber, G.G., Boyce, J.M., and Trask, N.J. (1977). Moon-Mercury: Large impact structures, isostasy and average crustal viscosity. *Phys. Earth Plant. Int. 15*, p. 189-201.

Schmidt, R.M. (1980). Meteor crater-implications of centrifuge scaling (abstract). In *Lunar and Planetary Science XI*, p. 984-986. Lunar and Planetary Institute, Houston.

Schubert G., Lingenfelter, R.E., and Terrile, R.J. (1977). Crater evolutionary tracks. *Icarus 32*, p. 131-146.

Schultz, P.H. (1974). A review of lunar surface features. In *A Primer in Lunar Geology* (R. Greeley and P. Schultz, eds.), p. 91-133.

Schultz, P.H. (1976). *Moon Morphology*. U. Texas Press, Austin, Texas. 626 pp.

Schultz, P.H. and Gault, D.E. (1975). Seismic effects from major basin formation on the Moon and Mercury. *Moon 12*, 159-177.

Scott, R.F. (1967). Viscous flow of craters. *Icarus 7*, 139-148.

Settle, M. and Head, J.W. (1979). The role of rim slumping in the modification of lunar impact craters. *J. Geophys. Res. 84*, 3081-3096.

Shoemaker, E.M. (1962). Interpretation of lunar craters. In *Physics and Astronomy of the Moon* (Z. Kopal, ed.), p. 283-357. New York & London, Academic Press.

Shoemaker, E.M. (1963). Impact mechanics at Meteor Crater, Arizona. In *The Moon, Meteorites and Comets* (B.M. Middlehurst and G.P. Kuiper, eds.), v. 4, p. 301-336. Chicago & London. U. of Chicago Press.

Shoemaker, E.M. and Passey, Q.R. (1979). Tectonic history of Ganymede (abstract). *EOS 60*, 871.

Smith, B.A., Soderblom, L.A., Beebe, R., Boyce, J., Briggs, G., Carr, M., Collins, S.A., Cook, A.F., Danielson, G.E., Davies, M.E., Hunt, G.E., Ingersoll, A., Johnson, T.V., Masursky, H., McCauley, J., Morrison, D., Owen, T., Sagan, C., Shoemaker, E.M., Strom, R., Suomi, V.E., and Veverka, J. (1979). The Galilean satellites and Jupiter: Voyager 2 imaging science results. *Science 206*, 927-950.

Smith, E.I. (1976). Comparison of the crater morphology-size relationship for Mars, Moon, and Mercury. *Icarus 28*, 543-550.

Smith, E.I. and Hartnell, J.A. (1978). Crater size-shape profiles for the Moon and Mercury: Terrain effects and interplanetary comparisons. *Moon and Planets 19*, 479-511.

Smith, E.I. and Sanchez, A.G. (1973). Fresh lunar craters: Morphology as a function of diameter, a possible criterion for crater origin. *Mod. Geol. 4*, 51-59.

Solomon, S.C. and Head, J.W. (1979). Vertical movement in mare basins: relation to mare emplacement, basin tectonics, and lunar thermal history. *J. Geophys. Res. 84*, 1667-1682.

Stöffler, D., Gault, D.E., Wedekind, J., and Polkowski, G. (1975). Experimental hypervelocity impact into quartz sand: Distribution and shock metamorphism of ejecta. *J. Geophys. Res. 80*, 4062-4077.

Strom, R.G., Trask, N.J., and Guest, J.E. (1975). Tectonism and volcanism on Mercury. *J. Geophys. Res. 80*, 2478-2507.

Thomsen, J.M., Austin, M.G., Ruhl, S.F., Shultz, P.H. and D.L. Orphal (1979). Calculational investigation of impact cratering dynamics: Early time material motions. *Proc. Lunar Planet. Sci. Conf. 10th*, 2741-2756.

Trask, N.J. and Strom, R.G. (1976). Additional evidence of Mercurian volcanism. *Icarus 28*, 559-563.

Ullrich, G.W. (1976). The mechanics of central peak formation in shock wave cratering events. *AFWL-TR-75-88*, Air Force Weapons Laboratory, Kirtland AFB, New Mexico, 134 pp.

Ullrich, G.W., Roddy, D.J., and Simmons, G. (1977). Numerical simulations of a 20-ton TNT detonation on the earth's surface and implications concerning the mechanics of central uplift formation. In *Impact and Explosion Cratering* (D.J. Roddy, R.O. Pepin and R.B. Merrill, eds.), p. 959-982. Pergamon Press, New York.

Veverka, J. and Duxbury, T.C. (1977). Viking observations of Phobos and Deimos: Preliminary results, *J. Geophys. Res. 82*, 4213-4223.

Veverka, J., Thomas, P., Gradie, J., Morrison, D., Davies, M. (1980). Amalthea: Analysis of Voyager imaging data (abstract). In *Reports of Planetary Geology Program, 1979-1980*, p. 343-344. NASA TM-81776.

Weertman, J. and Weertman, J.R. (1975). High temperature creep of rock and mantle viscosity. *Ann. Rev. Earch Planet. Sci. 3*, 293-315.

Wegener, Alfred (1920). Die Aufsturzhypothese der mondkrater. *Sirius Lpz. 53*, 189.

Wilhelms, D.E. (1976). Mercurian volcanism questioned. *Icarus 28*, 551-558.

Wood, C.A., Head, J.W., and Cintala, M.J. (1978). Interior morphology of fresh Martian craters: The effects of target characteristics. *Proc. Lunar Planet. Sci. Conf. 9th*, 3691-3709.

II. MECHANICS OF CRATER COLLAPSE: FORMATION OF SLUMP TERRACES, FLAT FLOORS, AND CENTRAL PEAKS

a) Introduction

Evidence that the simple bowl shaped crater is not an equilibrium landform above a certain threshold dimension was reviewed in section 1c. Physical inferences regarding crater collapse were drawn in 1d. The main purpose of this chapter is to preform a mechanical analysis of this situation and to elucidate the details of the process. The stability of transient crater is studied via an axisymmetric slip line theory of plasticity. The planetary surface material surrounding the newly formed cavity is considered to be a Mohr-Coulomb solid, parameterized by a cohesion strength and an internal friction angle.

The analysis yields two major results, reported in McKinnon (1978). The internal friction angle must be less than 2° for major collapse to occur. The rock must also possess rather low strength, on the order of tens of bars. This result is in substantial agreement with a previous analysis (Melosh, 1977) which considered the crater formed in a perfectly plastic material possessing no internal friction. While these material properties are inconsistent with laboratory measurements of the strength characteristics of rock (Handin, 1966), it is possible that they may be realized during the cratering process. Moreover, they are essential if the observed slumping is to occur.

A theoretical description of impact crater collapse is evolved which accounts for the development of wall scallops, slump terraces, and flat floors. The increasing occurrence of flat floors of nearly constant depth with increasing crater diameter is consistent with the re-establishment of mechanical equilibrium. A preliminary set of scale model experiments performed in a centrifuge (Melosh and McKinnon, 1979) corroborate the theory. These and other scale collapse experiments will be discussed in section 2g. The theoretical insights gained herein *do not* lead to a satisfactory description of central peak development, as discussed in sections 2e and 2h. Fortunately, pathways for more sophisticated analysis can be drawn.

b) Engineering Estimates of Crater Stability

Examining the stability of the crater form may be considered a specialization of slope stability analysis, a pre-eminent concern of soil mechanicians (e.g., see discussions in Scott, 1963; Terzaghi and Peck, 1967; Wu, 1976; Lambe and Whitman, 1979; and others). Dimensional considerations require that the effective crater failure strength c, be of the order $\rho g \ell$, where ℓ is the relevant length scale. Identifying this length with the limiting depth for simple craters ($\sim$ 2.5 km for the moon) and using lunar values for ρ and g (3.0 g/cm^3 and 162 g/s^2, respectively) gives

$$c \sim 12 \text{ MPa} \quad (120 \text{ bars}).$$

While intact rock specimens, measured in the laboratory, exhibit yield strengths in excess of 10^2 MPa (1 kbar), the effective strength of large masses of faulted and fractured rock may be closer to the above estimate.

More careful approaches to crater failure lead to even *lower* strength estimates, however. Field investigation of the collapse of cohesive slopes on earth has determined that failure occurs along discrete curved surfaces, oriented convexly outward to the direction of mass motion. These surfaces of slip are geometrically close to circles or logarithmic spirals. Analyses of the equilibrium of material along presumed failure surfaces are usually described in terms of a "stability factor"

$$N_s = \rho g H_c / c \quad , \qquad (2.1)$$

where H_c is the critical height for failure. Results give $N_s \geq 4$

at failure. Thus since $c \simeq \rho g H_c / N_s$, yield strengths for crater collapse are a few *tens of bars* at most. The mechanism of this low strength is unknown at present, but it is not implausible that freshly shocked rock behaves in this manner.

The analysis of this chapter does not assume that the failure surfaces are known, as above, but derives them. This provides a powerful method of predicting the geometry of collapse.

c) Field Equations of the Plastic Model

The mathematical model of crater stability begins with Cauchy's first law of motion for a continuum

$$- \nabla \cdot \mathbf{T} + \rho \underset{\sim}{b} = \rho \frac{d\underset{\sim}{v}}{dt} \quad , \tag{2.2}$$

where $\mathbf{T}$ is the stress tensor suitably defined so that compression is positive, $\underset{\sim}{b}$ is the body force per unit mass, and $\underset{\sim}{v}$ is particle velocity. Expansion in cylindrical coordinates is straightforward (Malvern, 1969). Axial symmetry is assumed for simplicity. All crater shapes examined here will be figures of revolution. The only body force considered will be gravity, directed in the positive z-direction (see figure 12).

The collapse of the transient crater is taken to be quasi-static, i.e., the inertial term $\rho \frac{d\underset{\sim}{v}}{dt}$ is neglected. This is justified if both

$$\left| \nabla \cdot \mathbf{T} \right| \gg \left| \rho \frac{d\underset{\sim}{v}}{dt} \right| \quad \text{and} \tag{2.3a}$$

$$\left| \underset{\sim}{g} \right| \gg \left| \frac{d\underset{\sim}{v}}{dt} \right| \quad . \tag{2.3b}$$

If ℓ and c are taken as characteristic lengths and stress as in section 2b, and a denotes a typical acceleration then equations (2.3) become

$$\rho a \ell / c \ll 1 \quad , \quad a/g \ll 1 \quad . \tag{2.4}$$

As $a\ell \sim v^2$, with v as a typical velocity, these conditions stipulate that accelerations must be small compared to gravity (free fall) and the slumping velocity must not grow so as to approach the hydrodynamic limit. This is clearly a good approximation for craters near the

FIGURE 12: Principal stress and slip line geometry. The crater is considered axially symmetric and rectangular in profile, with a depth H and diameter D. θ is the angle to the maximum principal stress (σ_1) direction, measured counterclockwise from the positive z-axis. σ_3 is the minimum principal stress. The characteristics of the plastic theory, or slip lines, form at angles of $\pi/4 - \phi/2$ with respect to the maximum principal stress direction. ϕ is the internal friction angle.

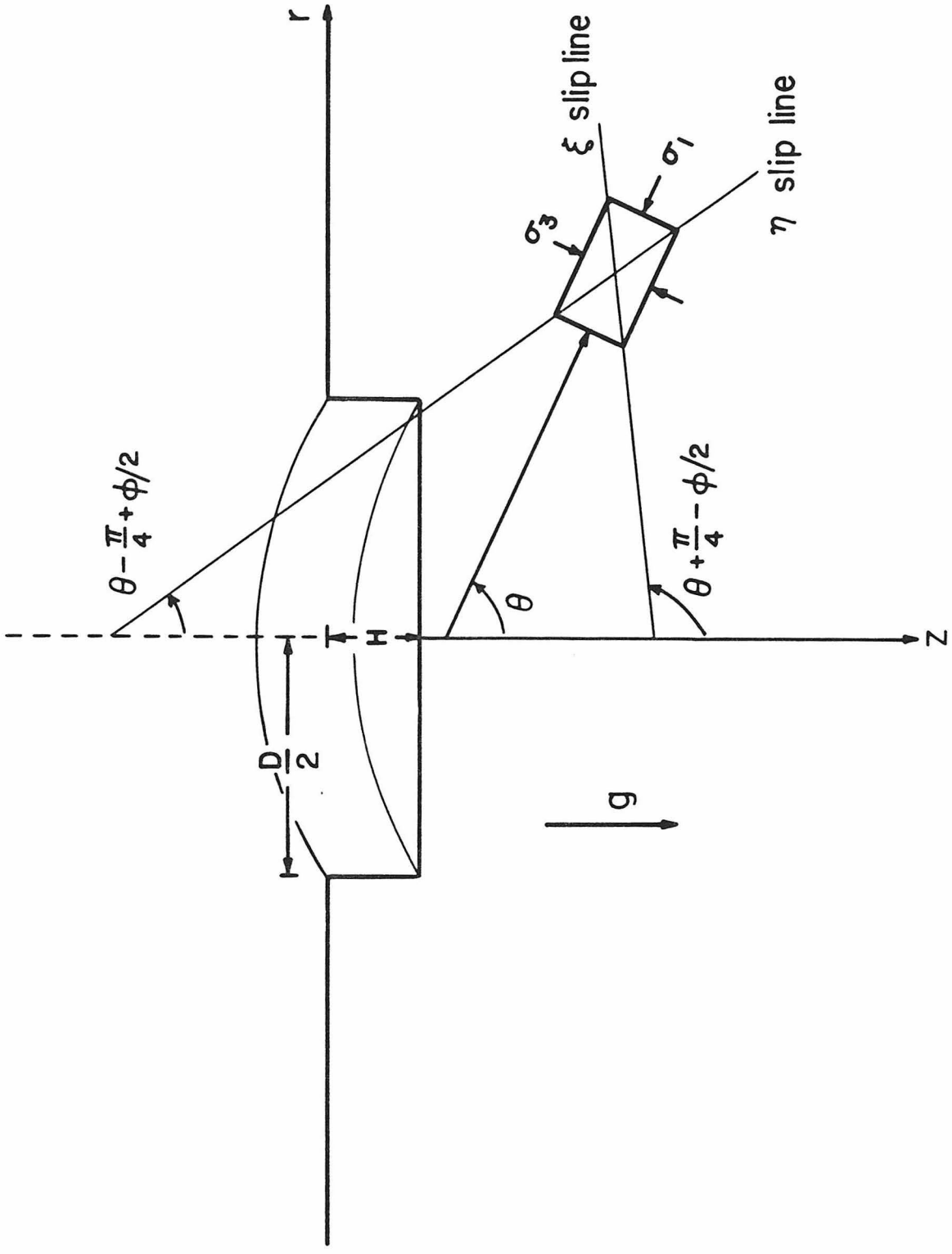
r
ξ slip line
η slip line
σ1
σ3
θ − π/4 + φ/2
θ + π/4 − φ/2
θ
H
D/2
g
z

stability limit, as discussed in the last chapter, and for the initiation of slumping, when velocity fields are minimized. The inertial term should be included when analyzing large scale transient craters significantly out of equilibrium and possibly at the late stages of collapse, when velocities peak. However, the incipient failure surfaces described by the quasi-static theory are likely to persist to these late stages.

Under the above qualifications equation (2.2) may be written in component form:

$$\frac{\partial \sigma_{rr}}{\partial r} + \frac{\partial \sigma_{rz}}{\partial z} + \frac{\sigma_{rr} - \sigma_{\varphi\varphi}}{r} = 0 \qquad (2.5a)$$

$$\frac{\partial \sigma_{rz}}{\partial r} + \frac{\partial \sigma_{zz}}{\partial z} + \frac{\sigma_{rz}}{r} = \rho g \quad , \qquad (2.5b)$$

where σ_{ij} is the stress tensor in cylindrical coordinates centered on the crater axis. The shear stress components $\sigma_{r\varphi}$ and $\sigma_{z\varphi}$ are zero for axial symmetry.

A failure strength model must be chosen that reproduces the inability of real materials to withstand arbitrarily large stress and strain. Such a model should be flexible in order to accommodate the variable and inhomogeneous physical structure of the rock units that define the crater. The Mohr-Coulomb model, incorporating a cohesion strength c and an internal friction angle ϕ, was first developed to describe the yielding of terrestrial soils. The failure law may be stated as:

$$\tau_f = c + \sigma_f \tan\phi \quad , \qquad (2.6)$$

where τ_f and σ_f are the shear and normal stresses acting on the failure plane *at failure*. The failure plane is inclined at an angle $\alpha = \frac{\pi}{4} - \frac{\phi}{2}$ to the principal stress direction. Figure 13 is a Mohr failure envelope for a Mohr-Coulomb solid.

Both cohesion and friction reflect the strength of molecular bonds between "soil" particles. The frictional resistance to shear, however, is proportional to normal stress. The constant of proportionality, tan ϕ, is often writen as μ , the coefficient of friction. The recognition of frictional behavior is credited to Leonardo da Vinci.

Mohr-Coulomb failure is an accurate description of yielding for a much wider range of geologic materials than soils. In triaxial tests, competent rock fails in this manner, and can be understood in terms of modified Griffith crack theory (McClintock and Walsh, 1962; Walsh and Brace, 1964). In this case, the cohesion strength c is much enhanced over that for soils. Thus the Mohr-Coulomb model (sometimes called Navier-Coulomb) will be adopted for analysis of yielding of freshly cratered materials, whether they be fines, rubble, breccia, or bedrock. It should be noted that generally $\phi \simeq 30\text{-}50°$ for terrestrial materials. Exceptions would be clays. Pure clay (after sufficient strain to align the plate-like clay particles face to face) may exhibit friction angles as low as 3-4° (Lambe and Whitman, 1979). *Saturation* can reduce this even further.

Equation (2.6) can be expressed in terms of the principal stresses ($\sigma_1 > \sigma_2 > \sigma_3$) at failure (see fig. 13 and Jaeger [1969]):

FIGURE 13: Mohr envelope for failure of a Mohr-Coulomb solid (symmetric about the σ axis, only the top half is shown). The Mohr circle represents the locus of all possible stress states in $\sigma\tau$ (normal and shear) space. The functional relationship for failure is $\tau_f = c + \sigma_f \tan \phi$. The failure plane is oriented at $\pm\alpha = \pm\left(\frac{\pi}{4} - \frac{\phi}{2}\right)$ to the principal stress (σ_1) direction. The development of one failure plane usually precludes the formation of its conjungate. Triaxial compression tests of real materials are described amazingly well by this failure criterion, though at high confining pressures, internal friction decreases (by up to a factor of ~ 2) as asperities on sliding surfaces yield plastically. Strength in tension is also inadequately described. Brittle materials fail at much lower stresses (dotted line) while granular, non-cohesive media have no strength in tension at all.

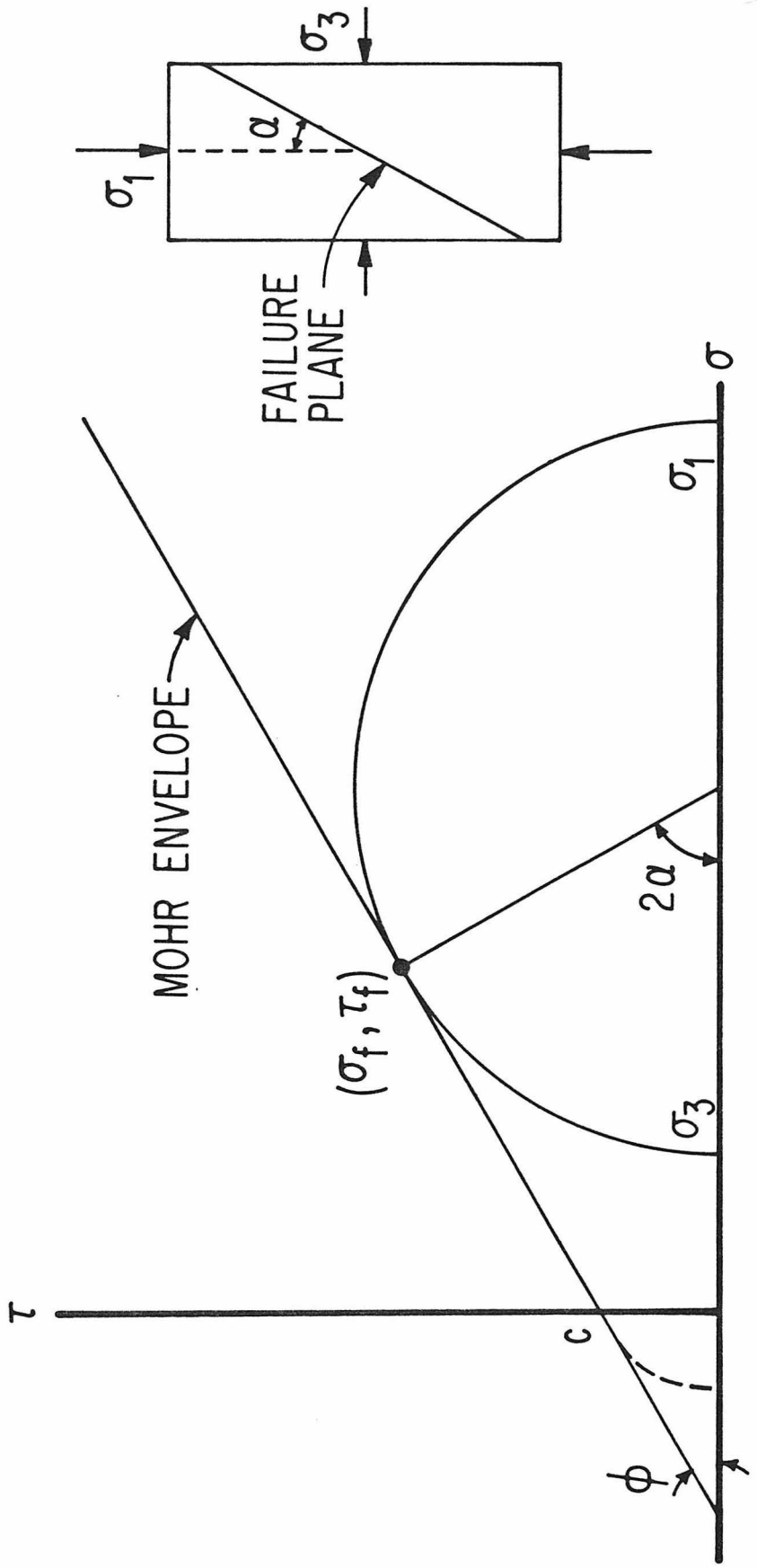
σ3
α
σ1
FAILURE PLANE
σ
σ1
MOHR ENVELOPE
2α
(σf, τf)
σ3
τ
c
i
φ

$$\frac{\sigma_1 - \sigma_3}{2} = c \cos \phi + \frac{(\sigma_1 + \sigma_3)}{2} \sin \phi \quad . \qquad (2.7)$$

The "hoop" stress $\sigma_{\varphi\varphi}$ is automatically a principal stress. Equations (2.5) and (2.7) constitute three equations in four unknowns, the relationship between the principal stresses in (2.7) and the σ_{ij} being strictly geometrical. It is therefore further assumed that the stress field satisfies the Haar-Von Kármán hypothesis (Cox *et al.* 1961), setting

$$\sigma_{\varphi\varphi} = \sigma_2 = \sigma_1 \qquad (2.8)$$

This allows a static determination of the stresses in the yielding, or *plastic* region.

No solution is complete without the specification of a compatible velocity field. However, given certain assumptions on the plastic flow, it can be shown to exist in principle. The strain rate behavior of the material is considered to be rigid, perfectly plastic, and obeying the associated flow rule. The rigid-plastic behavior entirely neglects elastic strain. Intuitively the plastic strain inherent in crater collapse completely dominates any elastic contribution in the *deforming* region. For those regions in which the stress state is below yield, $\tau < \tau_f$, plastic flow is not possible. The elastic response there is also ignored, with such material remaining completely undeformed ("rigid"). It is reasonable to assume that if the development of the plastic region is unconstrained by the elastic region , as it is in the problem under consideration

here, then treating the elastic zone as rigid will introduce small, if not negligible, errors.

The associated flow rule relates the generalized strain rates to the outward directed normal to the yield surface, defined by equation (2.7) in generalized stress space(i.e., the plastic potential; see Kachanov [1974]), through a rate parameter having the dimensions of time. Perfect plasticity determines that once a state of yield develops, unrestricted plastic flow is possible at that yield point. No account is given for changes in the yield surface (i.e., strain hardening) due to deformation. It is clear that while the Mohr-Coulomb yield criterion is valid for competent rock, perfect plasticity and the associated flow rule are not, as appreciable "strain softening" occurs in brittle failure. However, the extremely low yield strengths required for crater collapse obviate the consideration of this material as the "active" constituent of the crater form.

It is the examination of the velocity solutions under these assumptions that justify the use of the heuristic principle of Haar and Von Kármán. Alternate stress states for $\sigma_{\varphi\varphi}$ from that of equation (2.8) lead to certain vanishing velocity or strain rate components, and may be rejected *a priori* for the solution of this problem.

To solve the system of equations (2.5), (2.7), and (2.8), it is necessary to express the σ_{ij} in terms of the principal stresses and angle to the principal stress direction $\theta(r,z)$ measured in a counter-clockwise sense with respect to the positive z-axis (see figure 13):

$$\sigma_{rr} = \frac{1}{2}(\sigma_1+\sigma_3) - \frac{1}{2}(\sigma_1-\sigma_3)\cos 2\theta \qquad (2.9a)$$

$$\sigma_{zz} = \frac{1}{2}(\sigma_1+\sigma_3) + \frac{1}{2}(\sigma_1-\sigma_3)\cos 2\theta \qquad (2.9b)$$

$$\sigma_{rz} = \frac{1}{2}(\sigma_1-\sigma_2)\sin 2\theta \quad . \qquad (2.9c)$$

Combinations of (2.5), (2.7), (2.8), and (2.9) give two coupled quasi-linear hyperbolic partial differential equations for the stress field. A solution by the method of characteristics is appropriate. The equations can be uncoupled using the Riemann variables $\xi(r,z)$ and $\eta(r,z)$:

$$\xi(r,z) = \frac{\operatorname{ctn}\Phi}{2}\ell n\frac{Q}{c} + \theta \qquad (2.10a)$$

$$\eta(r,z) = \frac{\operatorname{ctn}\Phi}{2}\ell n\frac{Q}{c} - \theta \quad , \qquad (2.10b)$$

where

$$Q(r,z) = \frac{1}{2}(\sigma_1-\sigma_3) \quad . \qquad (2.11)$$

The uncoupled equations for ξ and η are

$$\left.\frac{d\xi}{dz}\right|_{\theta+\alpha} = \frac{-\rho g \sin(\theta-\alpha)}{2Q\cos(\theta+\alpha)} + \frac{\cos\theta\cos\alpha}{r\cos(\theta+\alpha)} \qquad (2.12a)$$

$$\text{on } \frac{dr}{dz} = \tan(\theta+\alpha)$$

and

$$\left.\frac{d\eta}{dz}\right|_{\theta-\alpha} = \frac{\rho g \sin(\theta+\alpha)}{2Q\cos(\theta-\alpha)} - \frac{\cos\theta\cos\alpha}{r\cos(\theta-\alpha)} \qquad (2.12b)$$

$$\text{on } \frac{dr}{dz} = \tan(\theta-\alpha)$$

where

$$\alpha = \pi/4 - \Phi/2 \quad . \qquad (2.13)$$

The characteristic curves defined by equations (2.12) and (2.13) are termed "slip lines." Through any point the "ξ" and "η" slip lines intersect at a constant angle $\frac{\pi}{2} - \Phi$ (see fig. 12). They are not in general orthogonal. The architecture for calculation of such characteristics is illustrated in figure 14. Given stress boundary conditions on some data curve $\mathscr{D}$, ξ and η are also known along $\mathscr{D}$. The variation of ξ is given by (2.12a) along a ξ-slip line, but because Q *and* θ are coupled in the definition of ξ, to determine θ (say at point 1a), information about η must be brought in on an η-slip line. Thus the iterative procedure is defined. New values of Q and θ at points 1a and 1b determine the position of point 2 and Q and θ there. Such a procedure must of necessity be carried out numerically and computational details are discussed in soil mechanics and plasticity literature (Hill, 1950; Sokolovski, 1960; Scott 1963). When $\mathscr{D}$ is itself a characteristic (fig. 14b), arbitrary stress conditions cannot be imposed, and another data curve ($\mathscr{D}'$) is required. In general the domain and range of the solution are finite, in contrast to that for elliptic PDE's.

The slip lines, because of the axial symmetry of the problem, are traces of surfaces of maximum shear stress available for yielding. As $\Phi \to 0$, these coincide with the surfaces of maximum shear. Under the plastic potential theory and associated flow rule for the stress states satisfying (2.5), (2.7), and (2.8), the velocity field is also hyperbolic and its characteristics *coincide* with that of the stress field.

FIGURE 14: Design for characteristic determination of the mathematical theory of plasticity. Stress boundary conditions are given on data curves $\mathscr{D}$ and $\mathscr{D}'$. The ξ and η-slip lines form the characteristic net.

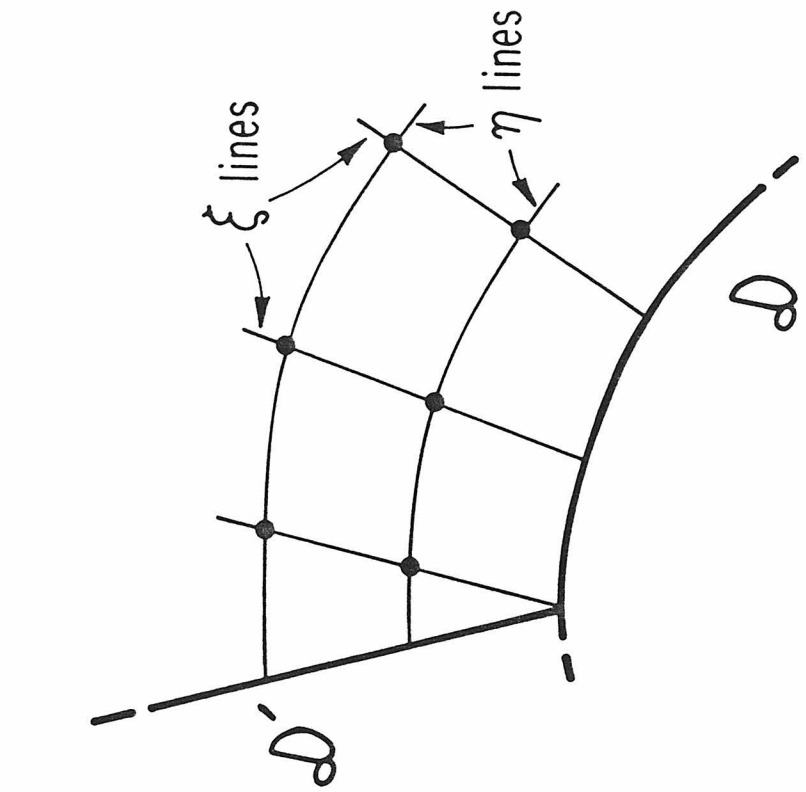

(b)

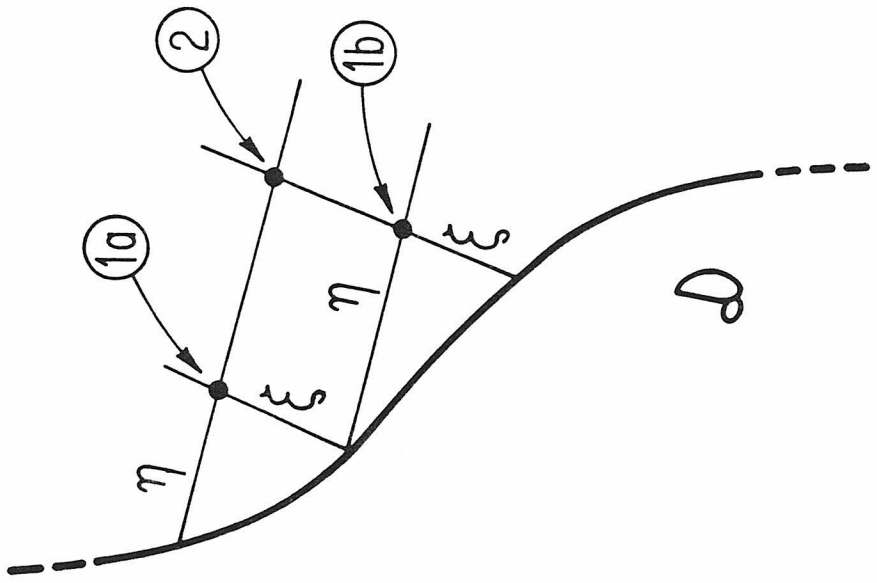

(a)

Hyperbolic systems such as this allow for the possibility of discontinuities in the solution. Weak discontinuities, as in the derivatives of the stress and velocity fields are possible generally, originating in non-analytic boundary conditions. Strong discontinuities in the field quantities themselves may also exist (Hill, 1950; Prager, 1954; Odé, 1960; Cox *et al.*, 1961; Kachanov, 1974). In particular, the velocity field tangential to the characteristic surfaces may be discontinuous *across these surfaces*, representing potential faults. These discontinuous solutions are, of course, only mathematical idealizations of transitions that would become smooth over suitably defined narrow regions, if higher order effects were considered in the field equations.

With the mathematical formalism above, the question of the mechanical stability of the crater form may be solved.

d) Analysis of Crater Slumping

The transient crater is considered to be rectangular in profile; that is, a right cylindrical hole of depth H and diameter D (see figure 12). Given suitable boundary conditions, the extent of the zone of plastic failure surrounding the crater and the stresses in that zone can be determined. This is illustrated by the example calculation at the top of figure 15.

The initial boundary condition is given by assuming the crater floor has failed. This determines Q and θ,

$$Q = c \frac{\cos \phi}{1 - \sin \phi} = c \tan \alpha, \ \theta = \pi/2 \quad , \tag{2.14}$$

and thus ξ and η there. Integration of equations (2.12) along the characteristics or slip lines determines ξ and η for a triangular region under the crater floor. The stress field is singular at the floor-rim contact ($z = H$, $r = d/2$). The principal stress direction rotates from $\pi/2$ to π there and defines a fan shaped slip line region (see fig. 15) as η but not ξ is continuous at that point. The slip line field may be extended outward from the crater by requiring that $\theta = \pi$ under the rim at $Z = H$, $r > D/2$. In the lower part of figure 15 the failed zone has been extended upwards assuming that the principal compressive stress is vertical throughout the rim region.

The extension of the slip line field to include the crater axis requires further analysis as equations (2.12) contain divergent terms as $r \to 0$. However, axial symmetry requires that

$$\sigma_{rr} = \sigma_{\varphi\varphi} \quad , \quad \sigma_{rz} = 0 \tag{2.15}$$

on $r = 0$. By equation (2.8) this implies that $\theta\big|_{r=0} = \pi/2$. Therefore

FIGURE 15: The upper part of the figure shows an example slip line field under a crater with a rectangular profile, depth/diameter ratio $\lambda = .2$, $\rho gH/c = 3$, and an internal friction angle $\phi = 3°$. Distances are normalized by the crater diameter D. The actual grid used in the numerical calculations is much finer than the one shown. In general the shape of the field is a function of λ, $\rho gH/c$, and ϕ. The extent of failure is given by the region below the rim where the calculated vertical stress is smaller than the rim overburden pressure ρgH (vertical arrows). The lower part of the figure shows progressively greater amounts of failure. The solid lines outline the failed zone and the arrows indicate the general direction of mass movement.

SLIP LINE FIELD/RECTANGULAR CRATER PROFILE

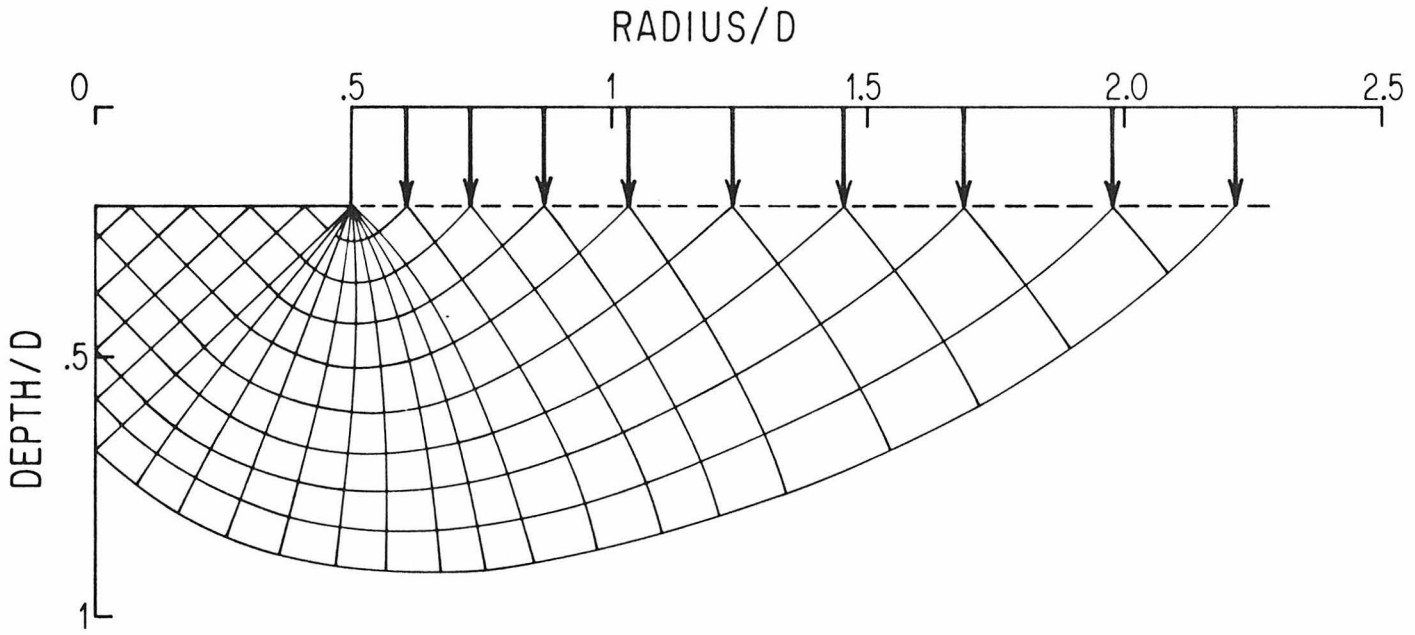

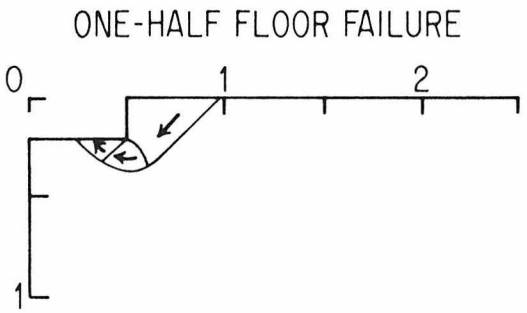

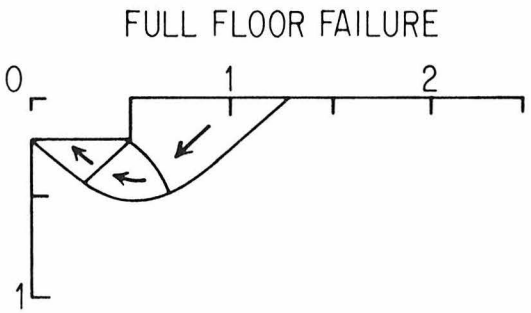

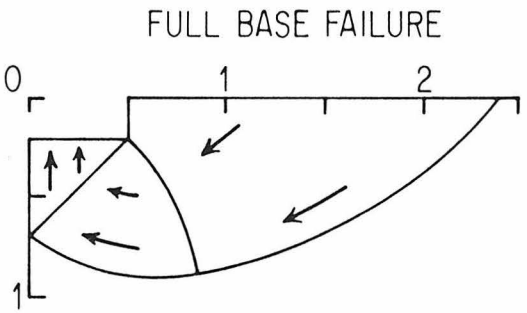

expand θ in a Taylor series about r = 0.

$$\theta(r,z) = \frac{\pi}{2} + k(z)r + \mathcal{O}(r^2) \quad . \tag{2.16}$$

Substituting (2.16) into (2.12a) and (2.12b), keeping only the leading terms in r, gives

$$\left.\frac{d\xi}{dz}\right|_{\theta+\alpha} = \left\{\frac{\rho g}{2Q} + k(z)\right\} \operatorname{ctn} \phi + \mathcal{O}(r) \quad , \tag{2.17a}$$

$$\left.\frac{d\eta}{dz}\right|_{\theta-\alpha} = \left\{\frac{\rho g}{2Q} + k(z)\right\} \operatorname{ctn} \phi + \mathcal{O}(r) \quad . \tag{2.17b}$$

Using (2.16) in conjunction with equations (2.9) to examine the stress equilibrium equations, (2.5a and 2.5b), in the limit of small r determines k(z):

$$k(z) = \frac{1}{4Q}\left\{(1 - \sin\phi)\left.\frac{dP}{dz}\right|_{r=0} - \rho g\right\} \quad , \tag{2.18}$$

where

$$P(r,z) = \frac{1}{2}(\sigma_1 + \sigma_3) \quad , \tag{2.19}$$

and

$$\lim_{r\to 0} \frac{\partial P}{\partial r} = 0 \quad . \tag{2.20}$$

As long as $\left.\frac{dP}{dz}\right|_{r=0}$ is known, the numerical solution of the slip line field may be carried out using the relations (2.17). This is true when the slip lines have already been extended a finite distance along the crater axis. However, $\left.\frac{dP}{dz}\right|_{r=0}$ must first be derived via a Taylor expansion of the surface boundary conditions at the center of the crater floor to begin the extension.

$$\left.\frac{dP}{dz}\right|_{r=0,z=H} = \frac{\rho g}{(1 - \sin\phi)} \tag{2.21}$$

for a rectangular profile. More generally, if the shape of the floor near the crater axis is expressed as

$$z(r)_{surf} = H + Br^2 + \mathcal{O}(r^3) \quad , \tag{2.22}$$

then

$$\left.\frac{dP}{dz}\right|_{r=0,z=H} = \frac{(-8BQ + \rho g)}{(1 - \sin \phi)} \quad . \tag{2.23}$$

Thus the characteristic net or slip line field may be extended throughout the region shown in figure 15, i.e., down along the axis, beneath the crater, and outward under the crater rim. The actual zone of plastic failure is given by the region below the rim where the calculated vertical stress is less than the overburden pressure $\sigma_{zz} = \rho gH$. This limit to the plastic zone is then followed back along the appropriate slip line to determine the extent of failure of the crater floor.

Through this model, it is possible to define modes of failure, essentially the extent of plastic collapse. Failure, if it occurs, is initiated under the crater rim crest. The bottom of figure 15 illustrates increasing degrees of failure from left to right. The first two are labeled by the amount of crater floor which has reached failure. The most extreme is termed "full base" in which the failed zone extends under the center of the crater. In this case the entire crater floor rises as a unit while the rim slumps downward. A general feature of base collapses is a zone of plastic failure centered on the crater axis which moves upward as a wedge-shaped plug.

A true bowl shaped crater collapses by a combination of deep-seated failure and slumping off the crater wall. Structures such as

central peaks may appear. By choosing the rectangular morphology and by not calculating an explicit time history of deformation, the details of the collapse of the crater rim and the development of other structures are by-passed. These features are important and controversial and their incorporation into the plastic model will be discussed in the following section. However, this approach does deal with the major large scale post-impact evolution of the crater.

The computations show that the stability depends on three factors: the angle of internal friction ϕ, a depth/diameter ratio λ, and a dimensionless parameter $\rho gH/c$. This dependence is shown in figure 16 and 17. The type of failure (or lack thereof) may be read as a function of initial λ and $\rho gH/c$ for eight values of ϕ.

For the case of a frictionless plastic material, $\phi = 0$, the depth/diameter ratio plays no role in determining crater stability. No collapse will occur for values of $\rho gH/c$ less than 5.1. For slightly larger values of this parameter the crater will undergo varying degrees of floor failure. When $\rho gH/c$ increases to 6.7, the floor slump reaches the center of the crater. When $\rho gH/c \geq 8.4$, the crater is in full base failure.

Addition of even a small amount of internal friction drastically affects the stability fields. As ϕ increases, the initiation of floor failure occurs at greater values of the strength parameter, $\rho gH/c$. This is easily seen by considering the continuity of η at the floor-rim contact. With equation (2.10b),

FIGURE 16: Crater stability and failure as a function of initial $\rho gH/c$ and λ for four small values of the internal friction angle (rectangular profile). The "canonical" depth/diameter ratio $\lambda = 0.2$ is denoted by a small arrow.

FIGURE 17: Similar to figure 16 but for values of the internal friction angle spanning the range encountered in static tests on terrestrial geologic materials.

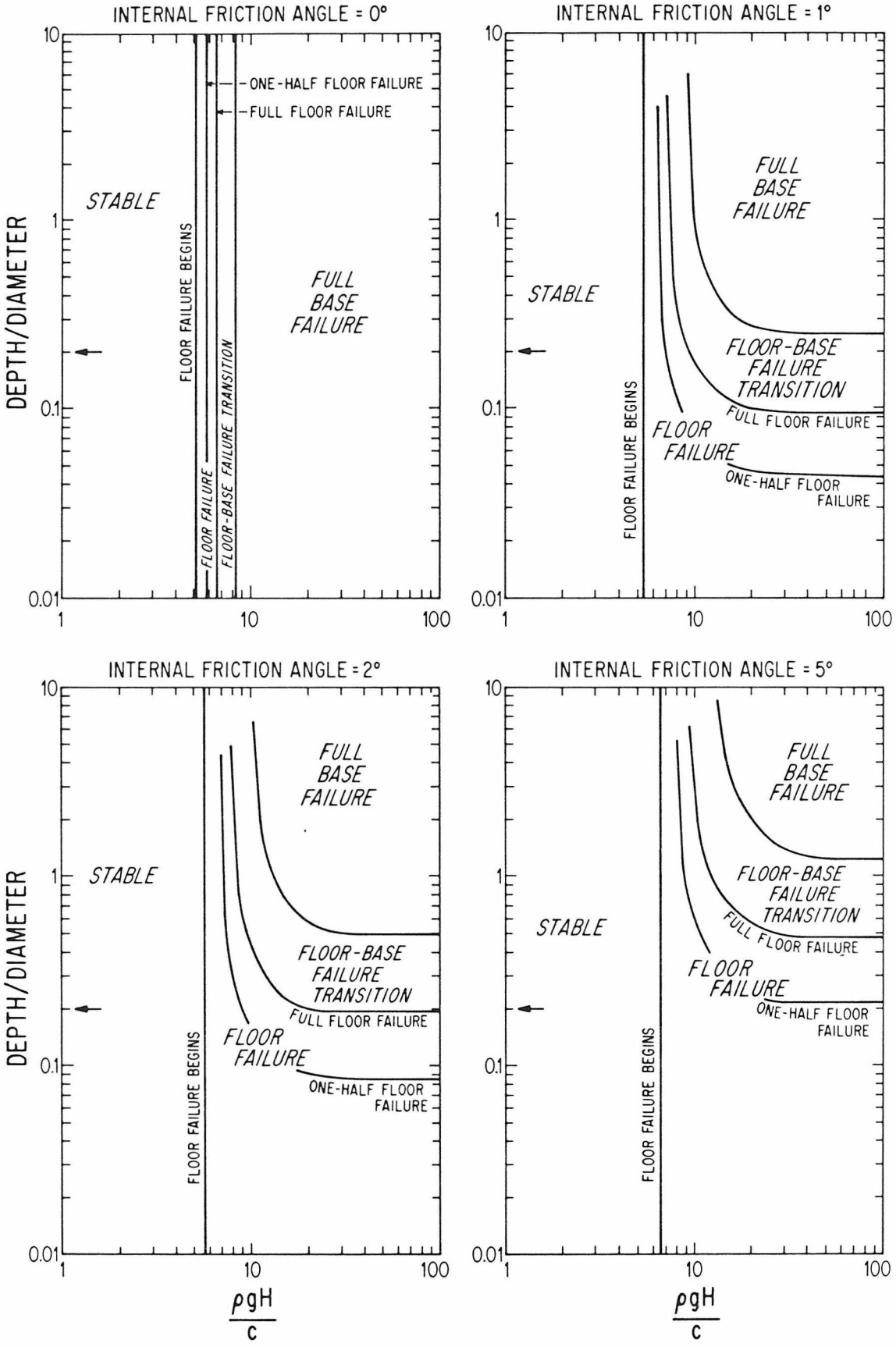
INTERNAL FRICTION ANGLE = 0°
INTERNAL FRICTION ANGLE = 1°
INTERNAL FRICTION ANGLE = 2°
INTERNAL FRICTION ANGLE = 5°
DEPTH/DIAMETER
10
1
0.1
0.01
1
10
100
STABLE
FULL BASE FAILURE
ONE-HALF FLOOR FAILURE
FULL FLOOR FAILURE
FLOOR FAILURE BEGINS
FLOOR FAILURE
FLOOR-BASE FAILURE TRANSITION
FLOOR-BASE FAILURE TRANSITION
FLOOR FAILURE
ρgH / c

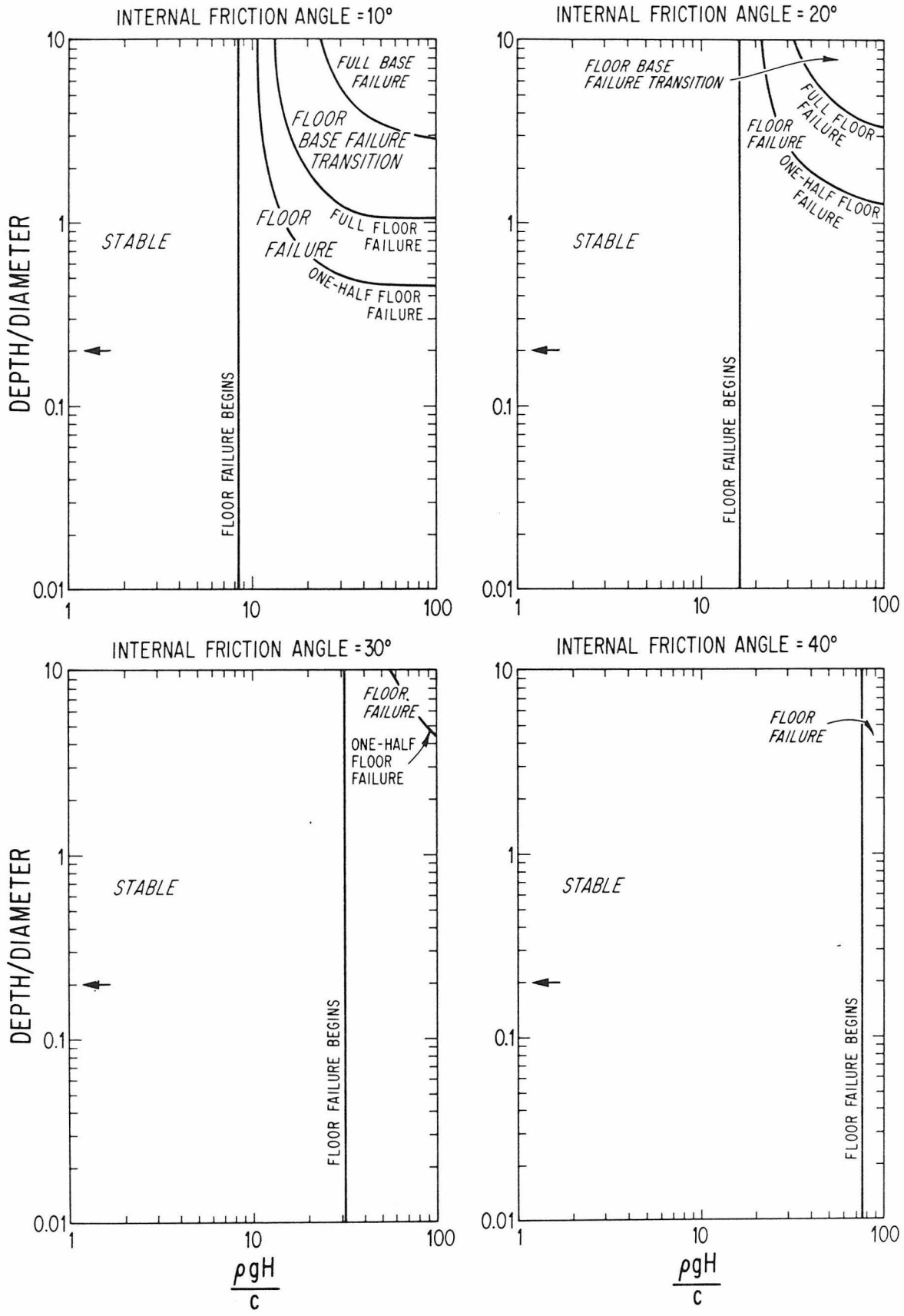
INTERNAL FRICTION ANGLE = 10°
FULL BASE FAILURE
FLOOR BASE FAILURE TRANSITION
FLOOR FAILURE
FULL FLOOR FAILURE
ONE-HALF FLOOR FAILURE
STABLE
FLOOR FAILURE BEGINS
DEPTH/DIAMETER
INTERNAL FRICTION ANGLE = 20°
FLOOR BASE FAILURE TRANSITION
FULL FLOOR FAILURE
FLOOR FAILURE
ONE-HALF FLOOR FAILURE
STABLE
FLOOR FAILURE BEGINS
INTERNAL FRICTION ANGLE = 30°
FLOOR FAILURE
ONE-HALF FLOOR FAILURE
STABLE
FLOOR FAILURE BEGINS
DEPTH/DIAMETER
ρgH / c
INTERNAL FRICTION ANGLE = 40°
FLOOR FAILURE
STABLE
FLOOR FAILURE BEGINS
ρgH / c
0.01
0.1
1
10
100

$$\frac{\operatorname{ctn}\Phi}{2}\ln\frac{Q}{c}\Big|_{z=H,r=D/2^-} = \frac{\operatorname{ctn}\Phi}{2}\ln\frac{Q}{c}\Big|_{z=H,r=D/2^+} + \frac{\pi}{2} \quad , \tag{2.24}$$

which leads directly to

$$\frac{\sigma_{zz}}{c}\Big|_{z=H,r=D/2^+} = \operatorname{ctn}\Phi\left[\left\{\frac{1+\sin\Phi}{1-\sin\Phi}\right\}\exp(\pi\tan\Phi) - 1\right]. \tag{2.25}$$

Values of this function for selected Φ are given in Table 3. Note:

$$\lim_{\Phi\to 0}\frac{\sigma_{zz}}{c}\Big|_{z=H,r=D/2^+} = 2 + \pi \quad . \tag{2.26}$$

The various degrees of floor and base failure only found to occur above certain increasing values of $\rho gH/c$ *and* λ. It is important that for some depth/diameter ratios certain modes of failure are forever out of reach, no matter how weak the material is or how deep the original cavity. Specifically, for $\lambda = .2$ (marked by an arrow on the diagrams) and $\Phi > 2°$ failure cannot reach the crater center. Computations for a range of internal friction values up to 40° demonstrate that the stability fields continue to move in a direction of increasing $\rho gH/c$ and λ. This makes sense physically, as the crater is gathering material strength by virtue of its greater internal friction.

The yield strength of a material possessing internal friction increases proportional to the load normal to the failure surface. Thus craters formed in such a material are inherently stronger than those formed in a frictionless one.

TABLE 3

Critical Rim Load to Initiate Failure

Φ	$\rho gH/c$
0°	5.14
0.25°	5.20
0.5°	5.26
1.0°	5.38
2.0°	5.63
3.0°	5.90
5.0°	6.49
10.0°	8.34
20.0°	16.18
30.0°	30.14
40.0°	75.31
50.0°	266.88
90.0°	∞

A compatible velocity field, described by the same web of characteristics used to determine the stresses, is suggested in fig. 15. The stress solution in the rigid region beyond is indeterminate. This lends a formal non-uniqueness to the problem. However, we may appeal to extremum principles developed for a rigid-plastic body in the absence of body forces (Kachanov, 1974). The extension to include body forces is trivial. Essentially, the power of the *actual* surface forces on given velocities is *greater* than the power developed by the surface forces corresponding to any other *statically admissible* system of yield stresses. Thus the limiting load $(\rho gH/c)^*$ cannot be less than the value of $\rho gH/c$ given by the solution of this chapter. That the strength parameters derived for various modes of collapse are lower bounds only amplifies the conclusion regarding the mechanical weakness of the transient crater. Finally, the similitude of this boundary value problem to the Prandtl solution for die indentation strongly suggests that the stress solution obtained is in fact the correct one.

e) Discussion

The plastic model, even for the simplified rectangular profile, yields insights into cratering phenomena on airless bodies. Nearly all transient craters start with H/D ratios ~.2 (at least those up to 50 km diameter, see section 1d), but only those large enough to be unstable collapse. The flat hummock floors of larger craters are probably due to a full base failure mechanism. If the kink in the lunar depth/diameter curve (figure 6) near 11 km is taken to be the limit of static stability, then for zero internal friction a cohesion strength of less than 2 MPa (20 bars) is required. The determination of $\rho gH/c$ in this estimate uses values for ρ, g, and H from section 2b, but there is an uncertainty as to which critical value of $\rho gH/c$ (and thus mode of failure) is represented by the limiting crater depth of 2.5 km. Full floor failure, developing at $\rho gH/c = 6.7$, is a reasonable choice and corresponds to c = 1.8 MPa (18 bars).

As ϕ increases, the cohesion strength necessary to induce failure becomes even smaller. Yet for internal friction values > 2°, full base or even full floor failure for $\lambda = .2$ cannot occur. Some very minor frictional behavior could explain the slow increase in crater depth for large (> 20 km diameter) craters. The flat floor/terrace wreath morphology is much closer to the rectangular profile crater model than the approximately parabolic transient form. Consequently the final λ and $\rho gH/c$ should reflect similar degrees of collapse as defined in figures 16 and 17. Given Pike's (1974) power law fit

to the depth/diameter data for large fresh lunar craters,

$$H = 1.055\ D^{0.301} \tag{2.27}$$

(with H and D in km); as D varies from 20 to 200 km, H (and in proportion, $\rho gH/c$, c assumed constant) varies from 2.6 to 5.1 km, and λ from 0.13 to 0.026. This variation matches major failure contours in stability diagrams similar to figures 16 and 17 for $\phi < 0.5°$.

A similar stability analysis to that of 2d for craters of parabolic profile complements the preceding solution by providing an explicit description of failure of the crater wall, i.e., the development of wall slumps and terraces. The same hyperbolic nature of the equations that allow the characterization of rim collapse prevent a complete solution from being found, however. Thus ultimately we must return to the rectangular profile for the general picture.

Extension of the parabolic analysis for $\phi = 0°$ (Melosh, 1977) to a frictional material yields no new insights as (1) the effective absence of internal friction has already been established, and (2) inclusion of friction prevents terracing of the rim, at variance with geologic evidence. Terrace development can be summarized as follows. A characteristic solution for the near-rim region is determined for small ($\rho gH/c < 6$) craters which is proved to be stable against the load applied by the rim lying above the ground plane (figure 18). As $\rho gH/c \rightarrow 7$, however, the group of η slip lines contract to form a singular surface (envelope of characteristics). The meaning is clear from studies of failure planes formed in infinite

FIGURE 18: Slip line calculations for craters of parabolic profile, zero internal friction, and depth/diameter ratio $\lambda = 0.2$. Distances are normalized by the crater diameter D. Only the near-rim region is shown. In (a) $\rho gH/c = 4$ and the crater is stable with respect to a rim load generalized from Pike (1977) and Settle and Head (1977). The slope angle at the rim, i, equals 30° for the parabolic geometry. (b) For $\rho gH/c = 8$ the η-slip lines have coalesced to form a characteristic envelope beneath the rim, identified as the fault plane on which the first slump block moves. This singular behavior of the solution occurs for $\rho gH/c \gtrsim 7$.

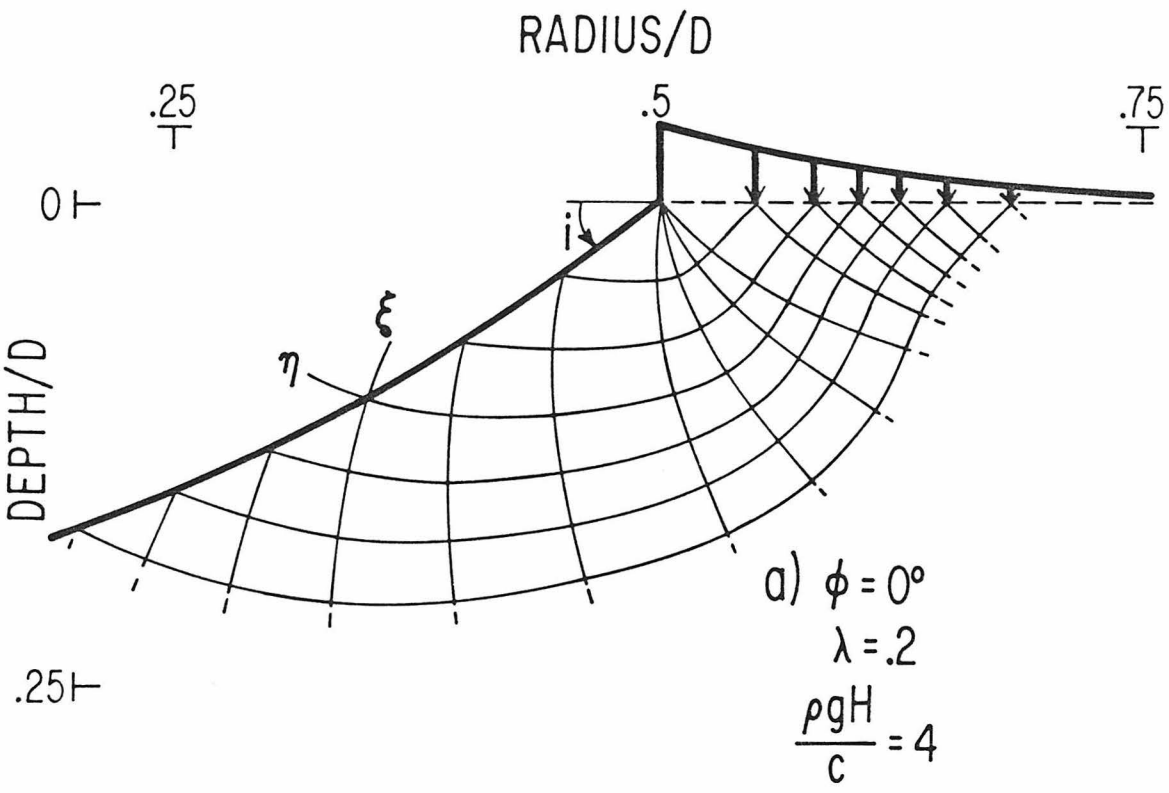
RADIUS/D
.25
T
.5
.75
T
0
i
ξ
η
DEPTH/D
.25
a) ϕ = 0°
λ = .2
ρgH/c = 4

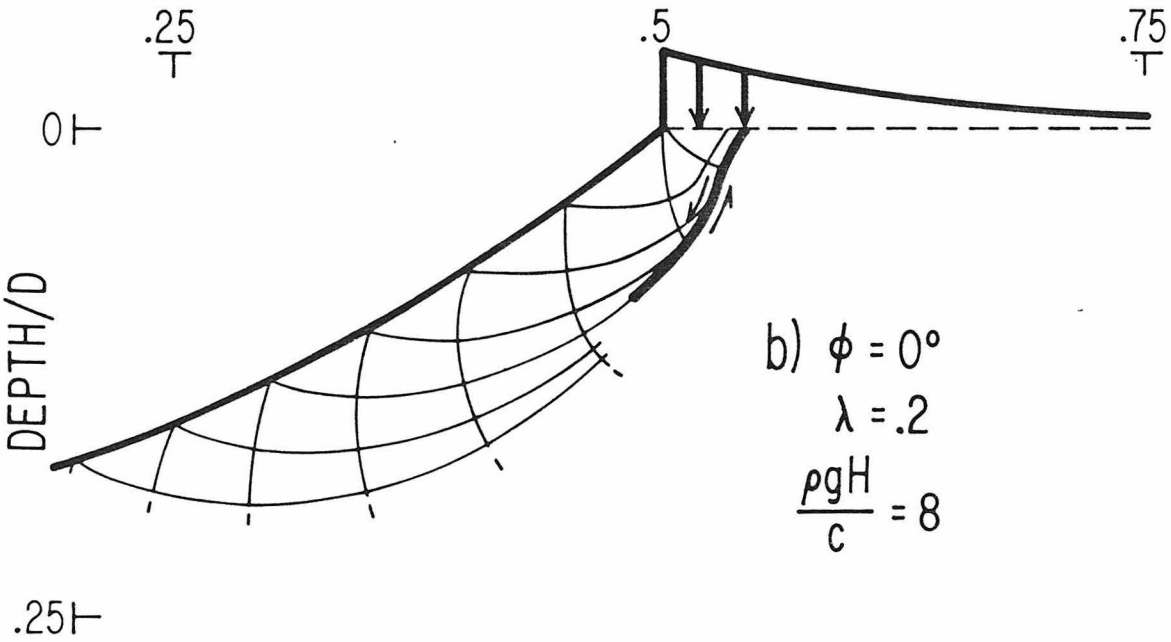
.25
T
.5
.75
T
0
DEPTH/D
.25
b) ϕ = 0°
λ = .2
ρgH/c = 8

cohesive slopes (Sokolovski, 1960). The singular surface develops where the shear resistance of the crater material to failure is first overcome. In the solution, $\sigma_{zz}|_{z=0,r=D/2+W}$ goes null on the critical η-line ($W \equiv$ terrace width). The solution cannot be continued across this surface as the quasi-static equilibrium conditions (2.5) can no longer be satisfied. However, the development of a terrace set, as well as more general modes of failure described in the rectangular analysis, is inferred.

The gentle contour of the transient parabolic rim allows the infinite slope approximation to be made. In this case, failure occurs on a plane at depth $h = c/\rho g \sin i \cos i$, where $i \equiv$ slope angle (Lambe and Whitman, 1979). For a parabolic crater $\tan i\,|_{z=0,r=D/2} = 4\lambda$. The width of an observable slump terrace is $W = h/\tan i = c/\rho g \sin^2 i$. Curiously, no definitive study of terrace widths for planetary surfaces exists. Preliminary measurements on Lunar Orbiter photographs by Melosh (1977) gave 2-4 km irrespective of crater diameter. An unpublished study (Jewitt, personal communication, 1980) of 47 craters, also from Orbiter photos, yielded 115 slump block widths, with a preferred value of 1.3 ± 0.3 km. A secondary cluster of values near 2.3 km is attributed to an observational doubling effect, when the intermediate fault plane is not well exposed. Analysis of the data set by this author has determined that the terrace width distribution is also invariant of terrain type (and crater diameter). For $\lambda = .2$ and $W = 1.3$ km, $c = 2.5$ MPa (25 bars). The agreement between independent estimates for the cohesion strength from

depth/diameter *and* terrace width measurements is gratifying.

The plastic model offers a unified understanding of the morphology of the collapsed crater except in regard to the central peak or peak complex. If peak formation is driven by slump terraces whose toes converge near the center of the crater floor, a possibility mentioned in section 1d, then the inadequacy of using the parabolic boundary value problem to delineate deformation in this region is "at fault." Nevertheless, the origin of the flat floors and surrounding terrace set of large (gravitationally unstable) craters *is* described.

Apparently the material encompassing the newly formed crater possesses low material strength and nearly zero internal friction. These characteristics seem odd, but it is essential that the material behave in this way if the observed slumping is to occur. The substantial plastic deformation that accompanies a hypervelocity impact may lower the cohesion strength, but whether internal friction could be eliminated is another matter. That is, formation of the crater naturally results in a massive envelope of structurally damaged rock as inherent flaws and fractures are activated, grow, and coalesce in response to the shock passage and subsequent large induced strain. This is seen in laboratory studies (Curran *et al.*, 1977) and in the gravitational signature of large, fresh lunar craters (Dvorak and Phillips, 1977). The failure strength characteristics of such a material may be much closer to those of a soil than those of competent rock. Nevertheless, it is expected that a large mass

of nearly fragmented material would still retain "normal" frictional characteristics (ϕ = 30-50°).

The reduction of friction in disrupted geologic media can be accomplished. In terrestrial situations the agent responsible is usually water, acting through pore pressure reduction of normal stress on fault planes. Yet there is no petrological evidence for there *ever* having been water on the moon. Radar measurements (Muhleman, 1972) and exceptionally high seismic Q values (Goins *et al.*, 1979) are also consistent with a dry moon. The absence of water in Mercury is also inferred, both from nebular condensation arguments (Lewis, 1972) and present day optical and thermal similarities to the moon (see Gault *et al.*, 1974). Analogous objections exist with respect to gaseous volatiles.

An intriguing possibility for the moon or Mercury would be melted rock itself, perhaps produced concomitant to the plastic deformation of excavation (Dence and Grieve, 1979). However, the distribution of impact melt at terrestrial impact structures (Grieve *et al.*, 1977; Kieffer and Simonds, 1980) is consistent with a compression/early excavation stage origin. While melt ejection along fissures into the surrounding country rock occurs, it appears not nearly as extensive as would be needed to fluidize the entire slumping region. More field and theoretical work on this topic is clearly needed.

Mechanisms to suppress frictional resistance in dry granular media exist, i.e., dispersive grain flow (Bagnold, 1956) and acoustic fluidization (Melosh, 1979). The latter depends on large amplitude

acoustic waves locally relieving overburden pressure. While energetically favored by several orders of magnitude over Bagnold grain flow, unresolved questions of dissipation remain. Presumably, acoustic Q values will be drastically lowered in melt containing regions, and the acoustic pressure field will be rapidly damped there. Thus fluidization by melt *and* acoustic energy could act simultaneously, but would be spatially separated.

The importance of understanding the role of post-shock material properties (as opposed to pre-impact *in situ* material properties) in crater formation and modification is beginning to be recognized (Cooper, 1977; Swift, 1977). Little data on the characteristics of freshly shocked rock are available. However, certain cratering computations have shown that low yield strengths are required to match the experimentally observed crater size and shape (Maxwell and Seifert, 1974). In such calculations internal friction may not actually be eliminated, but there may be a upper limit on the shear strength to failure. Such a yield criterion, while only slightly different from Mohr-Coulomb, does not fit into the analytic framework of the model. But the fact that even minor amounts of internal friction cannot be tolerated implies that the upper limit itself is only a few tens of bars. Other calculations employ the "Cap" model (Knowles and Brode, 1977), in which the material loses *all* resistance to shear above a certain mean stress.

The slumping of impact features seems to depend on the material strength degradation induced by the shock front(s) propagating through

the target. Thus the zone of plastic failure should be strongly influenced by the extent of the shocked region. As these large craters are formed well out of the regime where impact energy is mainly utilized to overcome cohesion (Holsapple and Schmidt, 1979; Schmidt, 1980), this shocked region will be substantial compared to the crater.

f) Interplanetary Comparisons

The theory of crater collapse can be used to evaluate material strength properties under impact for various planetary surfaces. Comparison of the depth-diameter relation for fresh lunar and mercurian craters (section 1c) determined that the mercurian inflection diameter and slumped depth is 70-80% that of the moon.

The ratio of gravitational accelerations for the two bodies is 2.28 ($g_{\mathbb{Y}} = 370$ g/s^2). This implies that the cohesion strength of the mercurian subsurface is greater by nearly a factor of two in order to compensate. That is, $\rho gH/c \sim 7$ should hold true for the prompt plastic collapse of craters on any planet. Transition diameters for terrestrial impacts in sedimentary and igneous strata are 1.5-2 and 4 km respectively (section 1c), so variations in c of a factor of two *are* plausible.

In a broad sense, terrestrial planet surfaces exhibit two strength classes with respect to impact. "Weak" materials ($c \sim 2.0$ MPa) characterize terrestrial sedimentary rock, lunar mare and highland terrain, and martian rock units where lunar-like craters occur. The respective diameters for "passage" from the simple bowl-shaped morphology are 1.5-2, 11, and 4-5 km, forming ratios nearly in accord with the inverse of surface gravity. "Strong" materials encompass terrestrial crystalline bedrock and both the mercurian *smooth plains* and *heavily cratered terrain*. With due account for the scatter in the mercurian depth-diameter relation, the cohesion strength for the mercurian materials is estimated at $c_{\mathbb{Y}} = 3.2 \pm 0.4$ MPa. The existence

of unshallowed mercurian craters *deeper* than their lunar counterparts is consistent with this greater strength.

The nature of these strength differences is poorly understood. It may be assumed that lower dynamic failure stresses and increased pre-impact crack density lead to reduced cohesion in the mass potentially involved in slumping. This would satisfy intuition regarding the weakness of sedimentary rocks compared to those of igneous origin, and the asymmetric terracing of lunar highland craters. In the latter case, preference for formation is given to those directions involving older brecciated crater rims. These are also topographically elevated, increasing the gravitational potential energy available for collapse. Nevertheless, the derived cohesion strengths (20-35 bars) cannot be predicted given a geology and shock history.

A nonlinear turn-on in the mechanism of acoustic fluidization may account for these cohesion strengths (Melosh, 1979). Viscosities are given in the theory by $\eta \sim \rho\lambda v_p$, where v_p = sound speed in fragmented rock and λ is an effective wavelength for the pressure field. λ is limited by the size distribution of the rubble and thus it is conceivable that increasing post-shock fracture densities (i.e., lowering average "block" size) may enhance fluidization and decrease cohesion.

Finally, it is worth noting that on bodies such as Amalthea ($g \sim 10$ g/cm^2) the simple crater form should persist up to sizes approaching that of catastrophic fragmentation ($\rho gH/c \sim 2$ for the crater described in section 1c). This appears to be the case.

g) Experimental Crater Collapse

An experimental approach to impact crater collapse has three motivations: (1) confirmation of predictions when the experiment conforms to the restrictions of the theoretical model, (2) testing inferences made by linking theoretical elements (e.g., the rectangular and parabolic profiles), and most importantly, (3) relaxing limitations imposed by the theory. Thus the effects of deviation from axial symmetry or non-uniform material properties can be studied. In addition, the collapse could be followed to large strain, *and* the influence of the inertial term could be evaluated for those craters whose transient form is well beyond the stability limit (see section 2b). Both of these effects are potentially important for central peak formation. At the drastically reduced scale of the experiments the surface strength parameter $\rho gH/c$ is kept at the prerequisite values for slumping by simultaneously lowering c (using clay as the "cratered" material) and increasing g in a centrifuge.

The centrifuge operated by Dr. R.F. Scott of the Caltech Civil Engineering Department was used in this study. At an arm radius of 36", accelerations up to 200 G are possible ($1G \equiv 981\ cm/s^2$). Mechanical constraints kept the G level under 100 however, and severely limited the usefulness of the experimental program.

Craters are formed in a mass of kaolinite clay, which exhibits the required plastic properties. Cohesion strengths range from 2.5 to 20 kPa (0.025 to 0.2 bar), depending upon consolidation pressure and time. NaCl (1% by weight) is added to the clay so that the residual

strength along faults in the clay would be definitely less than the initial cohesion. This facilitates observations of collapse by slump block formation, in contrast to a more uniform plastic deformation. $\rho_{clay} = 1.58 \pm 0.16$ g/cm^3. The clay and crater were contained in a right cylindrical aluminum bucket, 20" in diameter and 8"deep, mounted in a swing basket at the end of the centrifuge arm. Figure 19 details the bucket set up. The crater form is provided by a brass template, parabolic in profile, with a diameter and depth of 9.52 and 2.87 cm, respectively. With this scale, edge effects from the bucket can be ignored.

The experiments are conducted in two modes (figure 20). In progressive failure, the crater (with brass template removed) is spun up over a several minute interval to a maximum acceleration. Collapse is rapid compared to this spin up time, so the crater is always near the stability limit. A hub mounted television camera provides continuous monitoring of the crater. In prompt collapse, the crater form is maintained by the brass template (nearly equal the mass to the volume of displaced clay) until the specified G is reached. Then, via a wire harness, a hydraulic pull lifts the brass form away from the crater. Adhesion of this form to the clay surface is prevented by a thin layer of coarse sand. The quasi-state failure of the progressive mode, while not a good analogue for actual crater collapse, provides a useful comparison to the more dynamic nature of the prompt mode.

No wind effects are expected as the air within the aerodynamic housing rotates with the centrifuge. Coriolis forces can be neglected

FIGURE 19: Cross-section of centrifuge bucket set up for consolidation. Filter board and bottom sand provide an evaporation path for excess water in the clay. Blotting paper prevents mixing of clay and sand layers. Top sand determines overburden pressure during consolidation (which may be accomplished statically or in the centrifuge). Crater form is maintained by a brass template. Top sand is removed prior to collapse run.

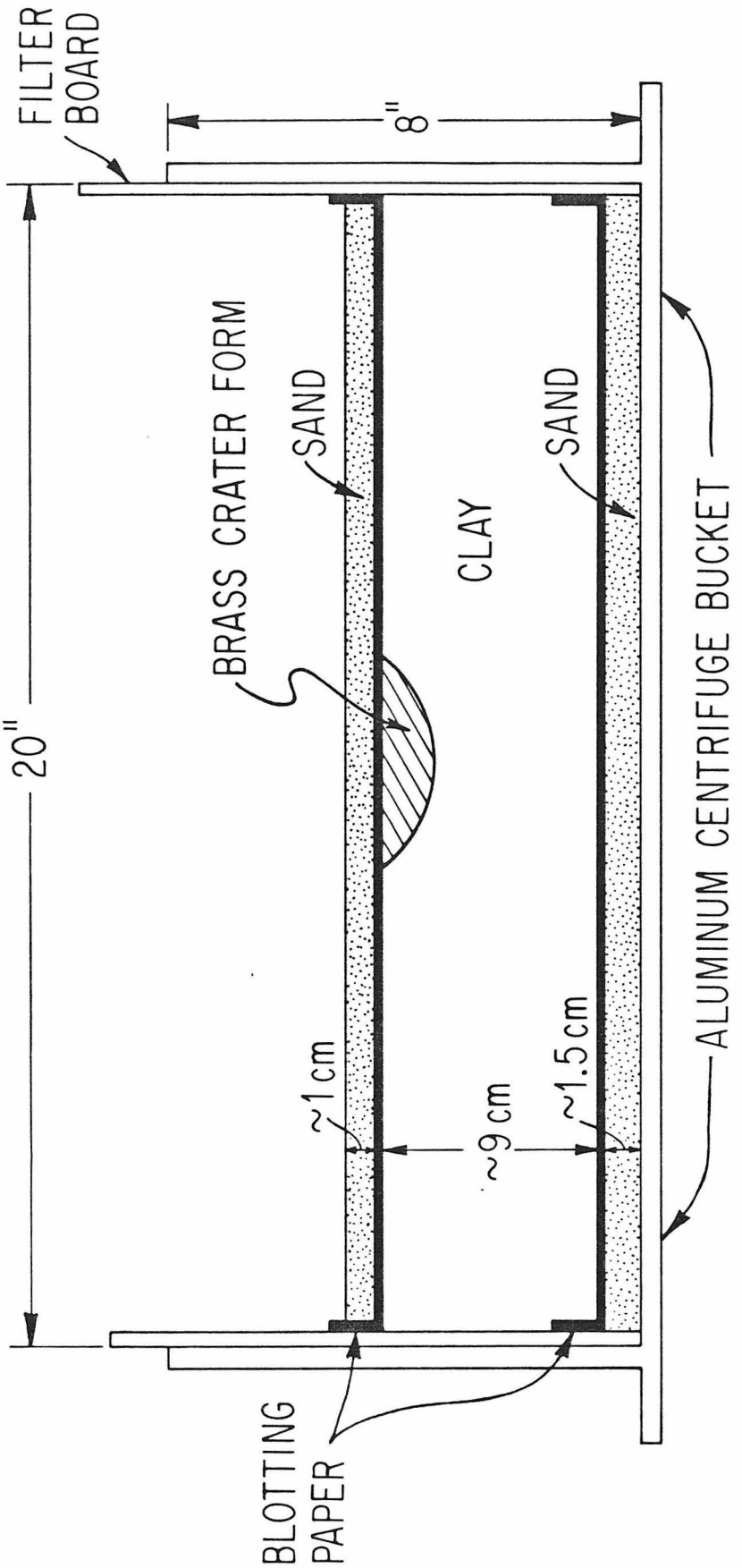
FILTER BOARD
8"
20"
BRASS CRATER FORM
SAND
CLAY
SAND
~1 cm
~9 cm
~1.5 cm
ALUMINUM CENTRIFUGE BUCKET
BLOTTING PAPER

FIGURE 20: The two modes of experimental crater collapse in this study. (a) Progressive failure, in which the clay crater is allowed to yield as the centrifuge spins up to maximum acceleration, shown by the "G-meter." (b) Prompt collapse, where the brass crater form is rapidly lifted from the clay surface *at* maximum G. A thin sand layer prevents induced strain due to withdrawal of the template. Crater deformations in both (a) and (b) are schematic.

a)

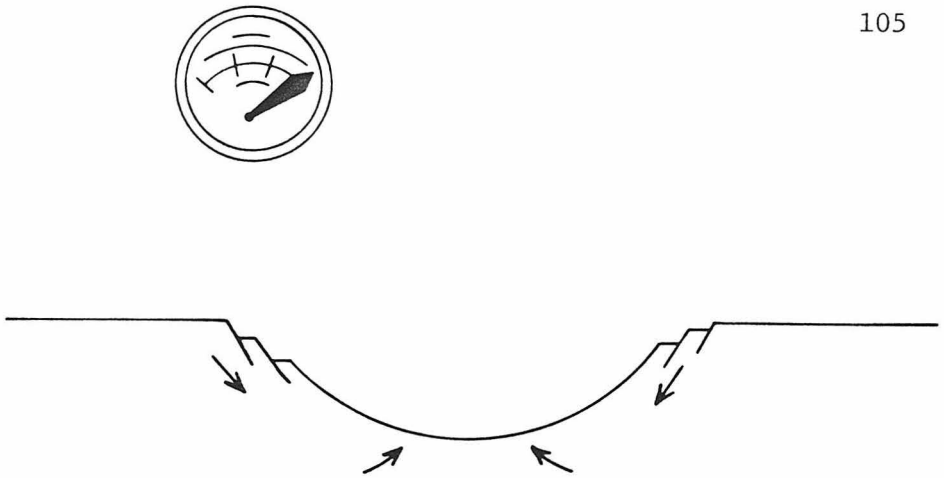

b)

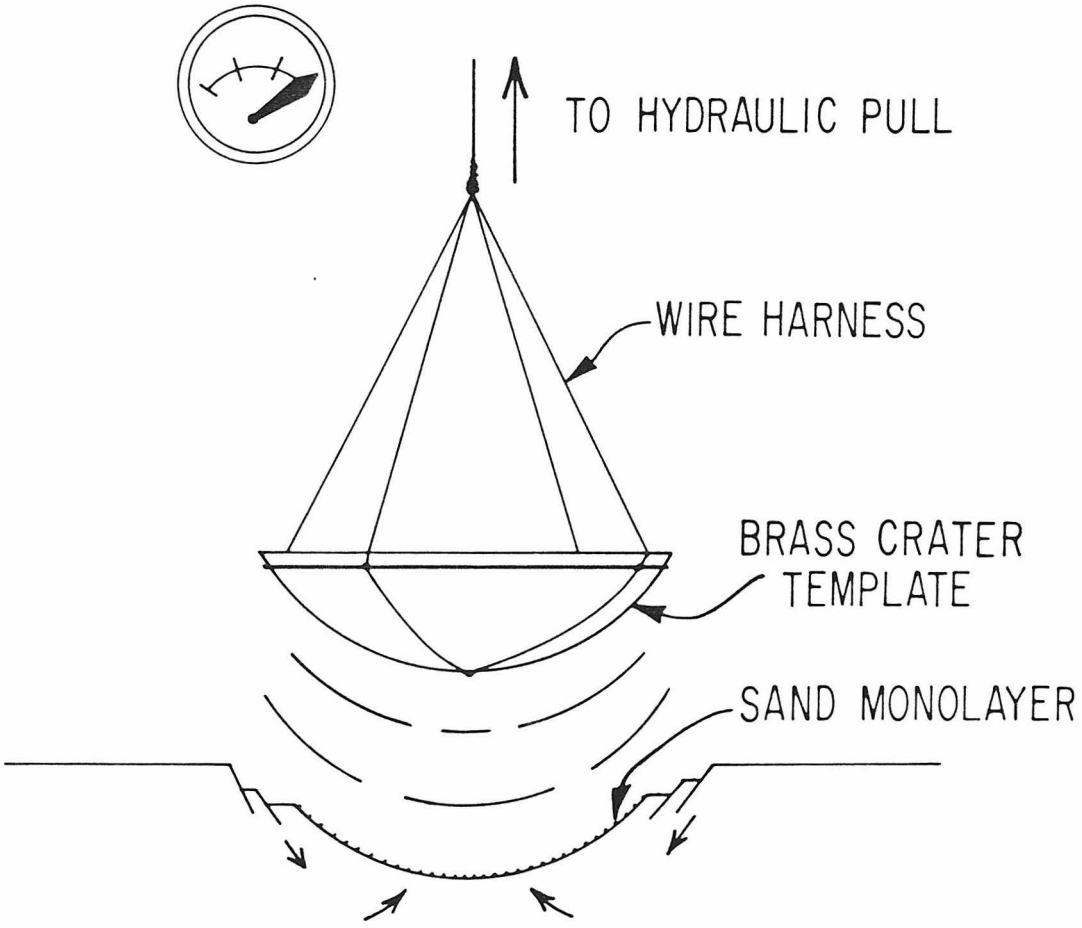
TO HYDRAULIC PULL
WIRE HARNESS
BRASS CRATER
TEMPLATE
SAND MONOLAYER

only if $\Omega v \ll g \equiv \Omega^2 R$, where Ω is the angular velocity of the centrifuge and R is the arm length. As maximum $v \sim \sqrt{gH}$ (free fall), the requirement becomes $\sqrt{H} \ll \sqrt{R}$. At best $\sqrt{H/R}$ is small but non-negligible. Since slump velocities should be substantially less than free fall, Coriolis effects can be ignored. In practice, v was actually limited by the speed of the hydraulic pull ($\sim$2.5 cm/s), so $\Omega v < 10$ cm/s^2.

For the lowest values of c and g $\sim$ 100 G, $\rho gH/c \sim 18$, corresponding to 25-30 km diameter lunar craters. During the course of the experiments, it became apparent that the clay was very prone to overconsolidation during spin up, resulting in a pronounced positive cohesion strength gradient in the clay mass (roughly linear, in proportion to overburden pressure). The problem was more acute for experiments with weaker, more saturated clays. The effectively limited the studies to $\rho gH/c$ values near the stability transition.

The results of 13 experiments (eight progressive failure and five prompt collapse) are given in Table 4. Agreement between theory and experiment is surprisingly good. Craters with initial $\rho gH/c \leqslant 5$ *do not* collapse. Slope failures are observed for $5 \leqslant \rho gH/c \leq 8$. Values inferred by assuming $(\rho gH/c)_{final} = 5.4$ are consistent with the c (cohesion) variation discussed above. For $\rho gH/c \geqslant 8$ full collapse is apparent, although the extreme weakness of the clays necessary to achieve these values, coupled with the evolution of large amounts of water during spin-up, indicate a substantial viscous response. In these experiments, a terrace set does not develop. In its stead a concentric zone of cracks is observed. In general, terrace widths

TABLE 4. EXPERIMENTAL CRATER COLLAPSE RESULT SUMMARY

Run	Type	$\rho gH/c$ [b]	$\rho gH_f/c$ [b]	Outcome	Terraces	Terrace Width W (cm)	$W_{theoretical}$ (cm)	Remarks
J11/1	dynamic	4.4 ± 0.5	-	no collapse	-	-	-	-
J11/2	quasi-static	8.3 ± 1.1[6.7]	5.4 ± 0.7	slope failure?	yes	0.48 ± 0.16	0.58 cm	-
J11/3[a]	dynamic	3.9 ± 0.2(6.3)	(5.4)	slope failure	yes	-	-	discrete partial terrace
J12/1	dynamic	5.0 ± 0.3	-	no collapse	-	-	-	-
J12/3[a]	quasi-static	7.6 ± 0.5[6.6]	7.6 ± 0.5	slope failure	yes	~0.64	0.71 (using surface c)	well developed wall slump, $\lambda = 0.38$
J30/1	dynamic	13.6 ± 3.4	5.4 ± 1.4	collapse (viscous?)	no	-	-	lack of NaCl, consolidation?
J30/2[a]	dynamic	13.2 ± 2.6(10.6)	(5.4)	collapse (viscous?)	no	-	-	"
J30/3[a]	quasi-static	11.2 ± 1.9(7.9)	7.6 ± 1.3(5.4)	slope failure	(cracks)	~0.32	0.42(0.32)	zone of concentric cracking within 1.9 crater radii
F7/1[a]	dynamic	17.9 ± 4.5	~0.0	viscous collapse	(cracks)	0.32 ± 0.08	0.27	collapsed nearly flat
F7/2[a]	dynamic	9.3 ± 1.3	2.6 ± 0.4	collapse	no	-	-	weak zone at depth
F7/3[a]	quasi-static	13.8 ± 2.8	3.9 ± 0.8	collaspe	(cracks)	0.48 ± 0.16	0.34	weak zone at depth, flat floor profile, concentric cracking to 2.7 crater radii
A4/1[a]	dynamic	3.0 ± 0.2	-	no collapse	-	-	-	over-consolidated
A4/2[a]	quasi-static	3.0 ± 0.2(6.9)	(5.4)	slope failure	-	-	-	some fine circumferential cracking not in accord with terrace width theory, $\lambda = 0.26$

[a] Possible interpretational ambiguity due to variable cohesion.

[b] Inferred strength parameters: ( ) from final crater height H_f, [ ] from first failure observed on television monitor. Error quoted is a lower bound from instrumental uncertainty in cohesion measurement.

(or crack spacings) are in rough agreement with theoretical prediction. The terrace wreaths developed in runs J11/2 and J12/3 resulted in an enlargement of the original crater. For J11/2 a diameter increase of ~20% was noted, while for J12/3 (shown in fig. 21) the expansion was 35-40%. This substantiates the arguments of Shoemaker (1962) and Mackin (1969) concerning diameter changes due to slumping.

Centrifuge scaling of this and other geologic phenomena is not new. An unpublished centrifuge crater collapse experiment of D. Gault used layered plasticene clay of unknown strength. The crater was failed in the progressive mode and subsequently cut in half along a vertical plane. Clear development of a terrace set in the rim was coupled with a conspicuous central base failure elevating the entire floor.

Simulations of large scale explosion cratering events, using dry Ottawa sand in the Boeing 600-G centrifuge (Schmidt and Holsapple, 1980), produced no evidence of crater shape change due to slumping. The stability of these craters is in accord with the frictional characteristics of the sand. A smaller, but similar, test series using oil-based clay (Schmidt and Holsapple, 1979) determined a stability threshold at $\rho gH/c \sim 18$. For this clay $\phi = 1.2°$. The largest stable craters ($\rho gH/c = 17$, $\lambda = .33$) and the single slumped example ($\rho gH/c = 18.5$, $\lambda = .24$) lie on a failure contour in the floor-base failure transition region of the stability diagram for $\phi = 1.0°$ (figure 16). A low-G crater, spun up to 500 G, collapsed in the progressive failure mode to near geometric similarity to the dynamically slumped crater, confirming the *existence* of a stability limit.

FIGURE 21: Oblique view of crater collapse experiment J12/3 (progressive failure). A wide zone of terraces formed, with slump toes inside the crater. A single large slump (arrow X) occupies ~45° on the circumference. Cohesion strength test points (arrows Y) surround crater. Central cracking is due to desiccation, as ten days elapsed between the experiment and photo.

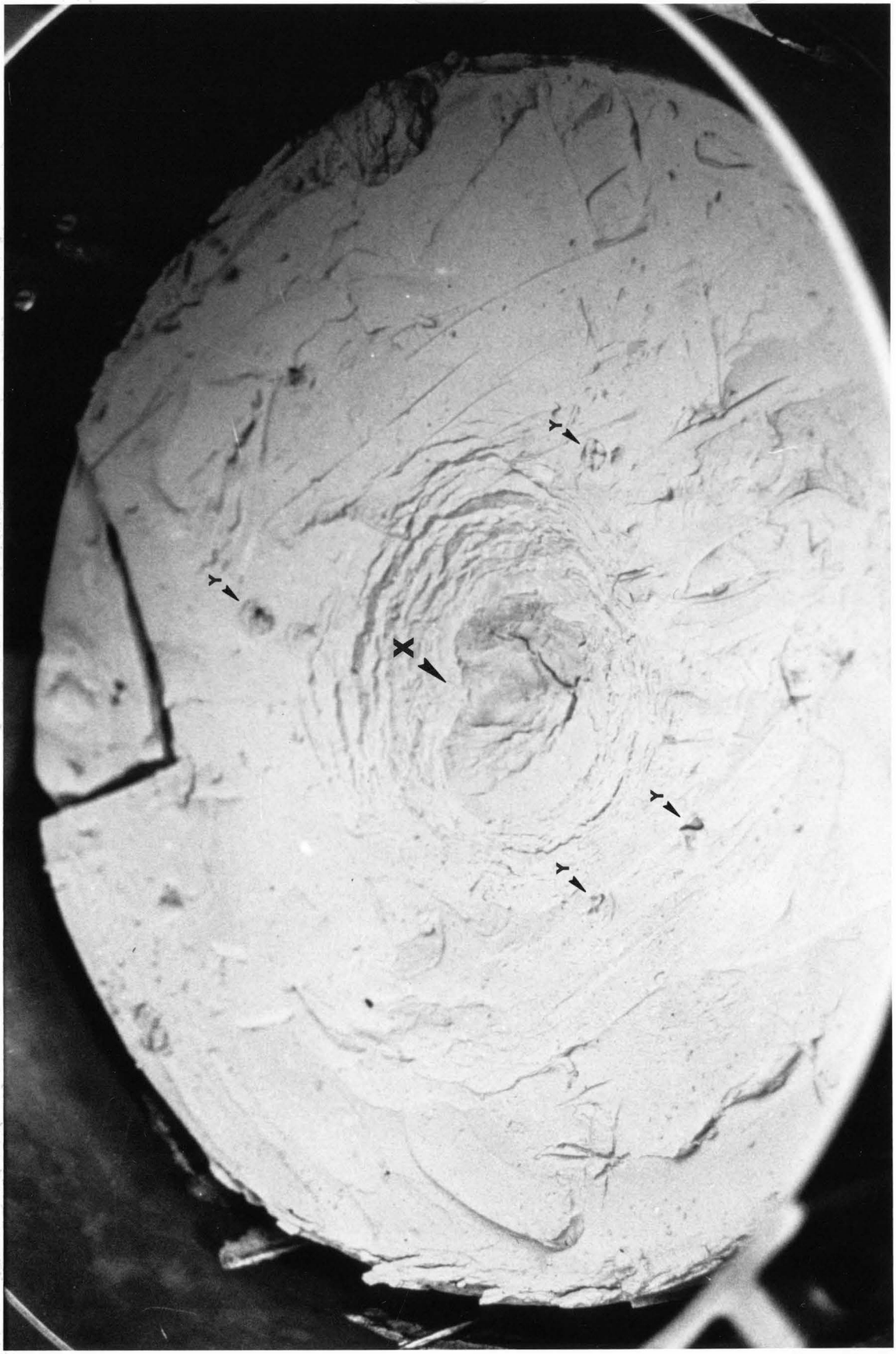

In summary, the experiments validate the theory but complications in *our* test series make more refined analysis difficult. The key to controlling the cohesion strength of the clay is using a stronger material, one that will not actively consolidate during the experiment. A co-requirement would be a centrifuge capable of much higher accelerations.

At present, no meaningful tests of craters formed well beyond the stability limit have been performed. The effects of inertial forces on the morphology of slumping for the largest impact craters remains ill-defined. The effects of large strain in the present experimental series were not surprising. The floors of the collapsed craters showed evidence of compression, i.e., multiple lobate thrusts in the clay and central "lumps." Central peaks were not observed.

h) Central Peaks

The theory of impact crater modification by gravitative adjustment does not explicitly predict the formation of a central peak. At best the central uplift takes the form of a coherent base failure. Scale centrifuge experiments in materials possessing the required plastic properties for collapse and terrace formation (low cohesion and negligible internal friction) substantiate the theory, though the consequences of large inertial forces remain unevaluated. With reference to the discussion of central peak mechanisms in section 1d, it is conceivable that the uniform plastic rheology does not lead to peak development. If uniformity is relaxed, allowing "weaker" material properties near the crater center, then fluidization and hydrodynamic oscillation of the peak region are possible.

An upper limit may be established on the viscosity of such an oscillation by estimating η for critical damping. Approximately $\eta \sim \rho g^{1/2} r^{3/2}$, where r = radius scale of the disturbance in question. More refined consideration (Scott, 1967) adds a factor of $\pi^{-3/2}$. The characteristic timescale is $t \sim \eta/\rho g r \sim r^{1/2} g^{-1/2}$. For lunar values of ρ and g and $r \sim 10$ km (typical of the central peak region of Copernican sized craters), $\eta \sim 10^9$ kg $m^{-1} s^{-1}$ (10^{10} poise) and $t \sim 80$ sec. Such viscosities are high compared to that of molten rock (Clark, 1966), but may be achievable in a clast/melt mixture. Quenching of the melt would occur in under 100 seconds (Kieffer and Simonds, 1980), damping the oscillation and preserving the peak. Alternately, acoustic fluidization viscosities are approximately equal to $\rho \lambda v_p$. With $v_p = 750$m/s

(typical of rock debris [Lambe and Whitman, 1979]), the proper viscosities can be realized as long as $\lambda < 300$ m. The peak material will behave as a viscous fluid (oscillate) until the acoustic field is dissipated. More theoretical and experimental work will be needed to provide estimates of this dissipation.

Clearly, even with these uncertainties, the next logical step in the overall theoretical analysis is incorporating hydrodynamic behavior into the plastic model. This could be accomplished via large scale computer codes (finite elements).

REFERENCES

Bagnold, R.A. (1956). The flow of cohesionless grains in fluids. *Phil. Trans. Roy. Soc. London A 249*, 235-297.

Clark, S.P., Jr. (1966). Viscosity. *GSA Memoir 97*, 291-300.

Cooper, H.F. (1977). A summary of explosion cratering phenomena relevant to meteor impact events. In *Impact and Explosion Cratering* (D.J. Roddy, R.O. Pepin, and R.B. Merrill, eds.), p. 11-44. Pergamon, N.Y.

Cox, A.O., Eason, D., and Hopkins, H.G. (1961). Axially symmetric plastic deformation in soils. *Phil. Trans. Roy. Soc. London A 254*, 1-45.

Curran, D.R., Shockey, D.A., Seaman, L. and Austin, M.(1977). Mechanisms and models of cratering in earth media. In *Impact and Explosion Cratering* (D.J. Roddy, R.O. Pepin, and R.B. Merrill, eds.), p. 1057-1087. Pergamon Press, New York.

Dence, M.R. and Grieve, R.A.F. (1979). The formation of complex impact structures (abstract). In *Lunar and Planetary Science X*, p. 292-294. Lunar and Planetary Institute, Houston.

Dvorak, J. and Phillips, R.J. (1977). The nature of the gravity anomalies associated with large young lunar craters. *Geophys. Res. Lett. 4*, 380-382.

Gault, D.E., Burns, J.A., Cassen, P., and Strom, R.G. (1977). Mercury. *Ann. Rev. Astron. Astrophys. 15*, 97-126.

Goins, N.R., Toksöz, M.N., and Dainty, A.M. (1979). The lunar interior: A summary report. *Proc. Lunar Planet. Sci. Conf. 10th*, 2421-2439.

Grieve, R.A.F., Dence, M.R., and Robertson, P.B. (1977). Cratering processes: As interpreted from the occurrence of impact melts. In *Impact and Explosion Cratering* (D.J. Roddy, R.O. Pepin, and R.B. Merrill, eds.), p. 791-814. Pergamon Press, New York.

Handin, J.A. (1966). Strength and ductility. *GSA Memoir 97*, 223-289.

Hill, R. (1950). *The Mathematical Theory of Plasticity*. Oxford Univ. Press, London. 355 pp.

Holsapple, K.A. and Schmidt, R.M. (1979). A material-strength model for apparent crater volume. *Proc. Lunar Planet. Sci. Conf. 10th*, 2757-2777.

Jaeger, J.C. (1969). *Elasticity, Fracture and Flow, with Engineering and Geological Applications*. Methuen & Co, Ltd., London, 268 pp.

Kachanov, L.M. (1974). *Fundamentals of the Theory of Plasticity*. MIR Publishers, Moscow. 445 pp.

Kieffer, S.W. and Simonds, C.H. (1980). The role of volatiles and lithology in the impact cratering process. *Rev. Geophys. Space Phys. 18*, 143-181.

Knowles, C.P. and Brode, H.L. (1977). The theory of cratering phenomena, an overview. In *Impact and Explosion Cratering* (D.J. Roddy, R.O. Pepin, and R.B. Merrill, eds.), p. 869-895. Pergamon Press, New York.

Lambe, T.W. and Whitman, R.V. (1979). *Soil Mechanics, SI Version*. John Wiley & Sons, New York. 553 pp.

Lewis, J.S. (1972). Metal/silicate fractionation in the solar system. *Earth Planet. Sci. Lett. 15*, 286-290.

Mackin, J.H. (1969). Origin of lunar maria. *Geol. Soc. America Bull. 80*, 735-748.

Malvern, L.R. (1969). *Introduction to the Mechanics of a Continuous Medium*. Prentice-Hall, Inc., Englewood Cliffs, New Jersey. 713 pp.

Maxwell, D.E. and Seifert, K. (1974). Modeling of cratering, close-in displacements, and ejecta. *Report DNA 3628F*, Defense Nuclear Agency, Washington, D.C., 106 pp.

McClintock, F.A. and Walsh, J.B. (1962). Friction on Griffith cracks in rocks under pressure. *Proc. Natl. Congr. Appl. Mech. 4th, Berkeley*, 1015-1021.

McKinnon, W.B. (1978). An investigation into the role of plastic failure in crater modification. *Proc. Lunar Planet. Sci. Conf. 9th*, 3965-3973.

Melosh, H.J. (1977). Crater modification by gravity: A mechanical analysis of slumping. In *Impact and Explosion Cratering* (D.J. Roddy, R.O. Pepin, and R.B. Merrill, eds.), p. 1245-1260. Pergamon Press New York.

Melosh, H.J. (1979). Acoustic fluidization: A new geologic process? *J. Geophys. Res. 84*, 7513-7520.

Melosh, H.J. and McKinnon, W.B. (1979). Theoretical and experimental study of crater collapse (abstract). In *Lunar and Planetary Science X*, p. 830-832. Lunar and Planetary Institute, Houston.

Muhleman, D.O. (1972). Microwave emission from the moon. In *Thermal Characteristics of the Moon* (J.W. Lucas, ed.), p. 51-81. MIT Press, Cambridge, Massachusetts.

Odé, H. (1960). Faulting as a velocity discontinuity in plastic deformation. *GSA Memoir 79*, 293-321.

Pile, R.J. (1974). Depth/diameter relations of fresh lunar craters: Revision from spacecraft data. *Geophys. Res. Lett. 1*, 291-294.

Pike R.J. (1977). Size dependence in the shape of fresh impact craters on the moon. In *Impact and Explosion Cratering* (D.J. Roddy, R.O. Pepin, and R.B. Merrill, eds.), p. 484-509. Pergamon Press New York.

Prager, W. (1954). Discontinuous fields of plastic stress and flow. *Proc. Second United States Nat. Longr. Appl. Mech. (Ann Arbor, Mich., 1954)*, 21-32.

Schmidt, R.M. (1980). Metor crater-implications of centrifuge scaling (abstract). In *Lunar and Planetary Science XI*, p. 984-986. Lunar and Planetary Institute, Houston.

Schmidt, R.M. and Holsapple, K.A. (1979). Centrifuge crater scaling experiment II: Material strength effects. Interim report, Boeing Aerospace Company, Seattle, Washington.

Schmidt, R.M. and Holsapple, K.A. (1980). Theory and experiments on centrifuge cratering. *J. Geophys. Res. 85*, 235-252.

Scott, R.F. (1963). *Principles of Soil Mechanics*. Addison-Wesley Publishing Co., Reading, Mass. 550 pp.

Scott, R.F. (1967). Viscous flow of craters. *Icarus 7*, 139-148.

Settle, M. and Head, J.W. (1977). Radial variation of lunar crater rim topography. *Icarus 31*, 123-135.

Shoemaker, E.M. (1962). Interpretation of lunar craters. In *Physics and Astronomy of the Moon* (Z. Kopal, ed.), p. 283-357. New York & London, Academic Press, 538 pp.

Sokolovski, V.V. (1960). *Statics of Soil Media*. Butterworths Scientific Publications, London. 237 pp.

Swift, R.P. (1977). Material strength degradation effect on cratering dynamics. In *Impact and Explosion Cratering* (D.J. Roddy, R.O. Pepin, and R.B. Merrill, eds.), p. 1025-1042. Pergamon Press, New York.

Terzaghi, K. and Peck, R.B. (1967). *Soil Mechanics in Engineering Practice*, 2nd ed., John Wiley and Sons, New York. 729 pp.

Walsh, J.B. and Brace, W.F. (1964). A fracture criterion for brittle anisotropic rock. *J. Geophys. Res.* 69, 344-3456.

Wu, T.H. (1976). *Soil Mechanics*, 2nd ed., Allyn and Bacon, New York.

III. MULTIRINGED BASINS IN THE SOLAR SYSTEM: A "NEW" PARADIGM

a) Introduction

On the basis of lunar studies, multiringed basins were recognized as major geologic structures (Hartmann and Wood, 1971). The youngest and best preserved of these, Orientale (seen in figure 22), displays a complex, quasi-axially symmetric topography. At least four rings are contained within a diameter of roughly 900 km. The outer ring, or Montes Cordillera, is prevalently asymmetric, with steep inward facing scarps and subdued outer slopes. The inner Montes Rook appears to be a more symmetric, concentric alignment of peaks or massifs.

Such near symmetry is often seen in smaller double ring basins such as Antoniadi and Schrödinger (figure 23) on the moon. As studied by Head (1977), these basins demarcate a transition (near 150 km diameter) from "simpler" craters possessing central peaks. At still greater scales, more rings appear (e.g., Orientale).

The Mariner missions to Mars and Mercury revealed many new multiring structures. The Mercurian double ring basins, Strindberg and Ahmad Baba are seen in figure 24. On Mercury the transition from central peaks to "peak rings" occurs near 100 km diameter (Gault *et al.*, 1975). Understanding the mechanics of ringed basin formation has proven difficult, however, largely due to degradation of topography by repeated bombardment, volcanic activity, and other obscuring processes described in section 1e.

FIGURE 22: The Orientale basin, located near the western limb of the moon, is characterized by three major mountain rings or scarps: Montes Cordillera, 930 km diameter (arrow A), outer Montes Rook (arrow B), and inner Montes Rook (arrow C). Also prominent are the radially lineated ejecta blanket (Hevelius Formation) and central flood basalts (Mare Orientale). A less prominent inner ring can also be seen (white arrow). *Lunar Orbiter photograph IV-187-M.*

FIGURE 23: The double-ring basins Schrödinger and Antoniadi near the south pole of the moon, 320 and 140 km in diameter, respectively. The outer "rings" correspond to zones of terrace slumping similar to that of Theophilus (figure 8), Brahms (figure 10) and other large craters on the moon and Mercury. The inner rings are annular groupings of peaks. Schrödinger is partially filled with a smooth, plains-forming unit. Floor fractures are evidence of tectonism subsequent to filling. The younger Antoniadi also contains a small (vestigal?) central peak. *Lunar Oribter photograph IV-8-M.*

FIGURE 24: The double-ring basins Strindberg (185 km diameter) and Ahmad Baba (130 km), in the *intercrater plains* NE of Caloris. Distinctive secondary crater chains and *smooth plains* fill are observable. The origin of the inner rings, like those of Schrödinger and Antoniadi remains unexplained. *Mariner 10 frame FDS 150* (orthographic projection).

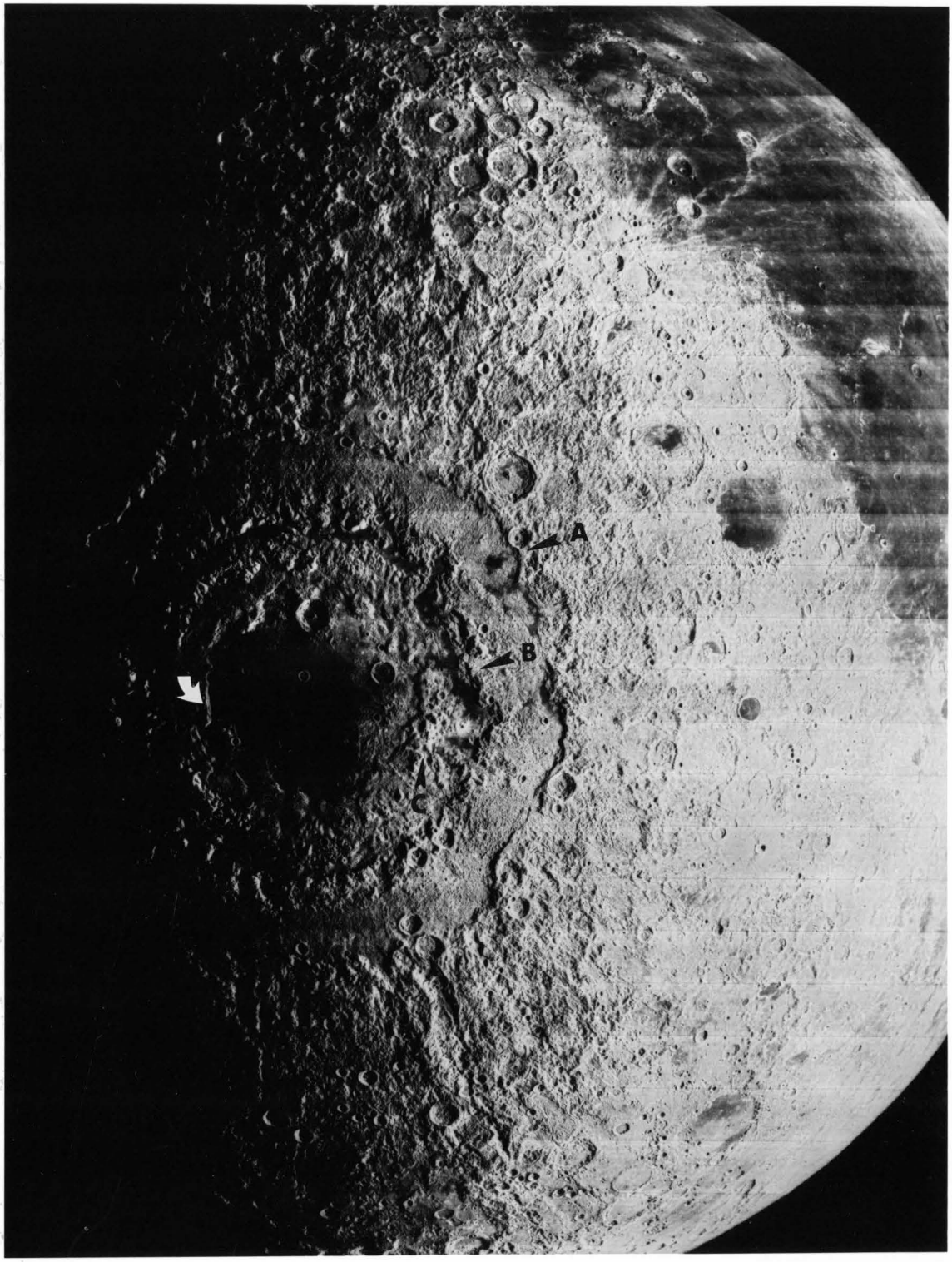
A
B
C

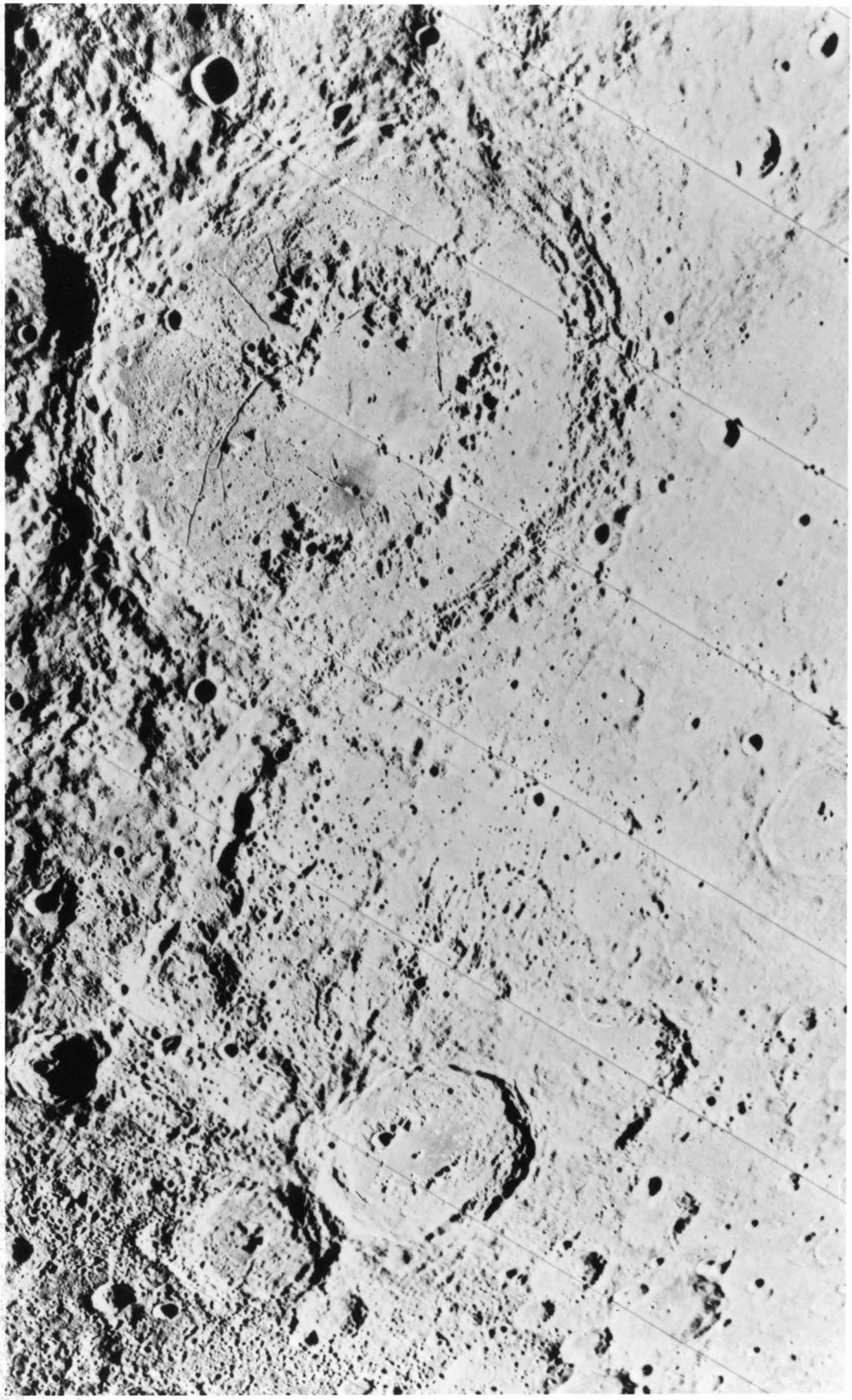

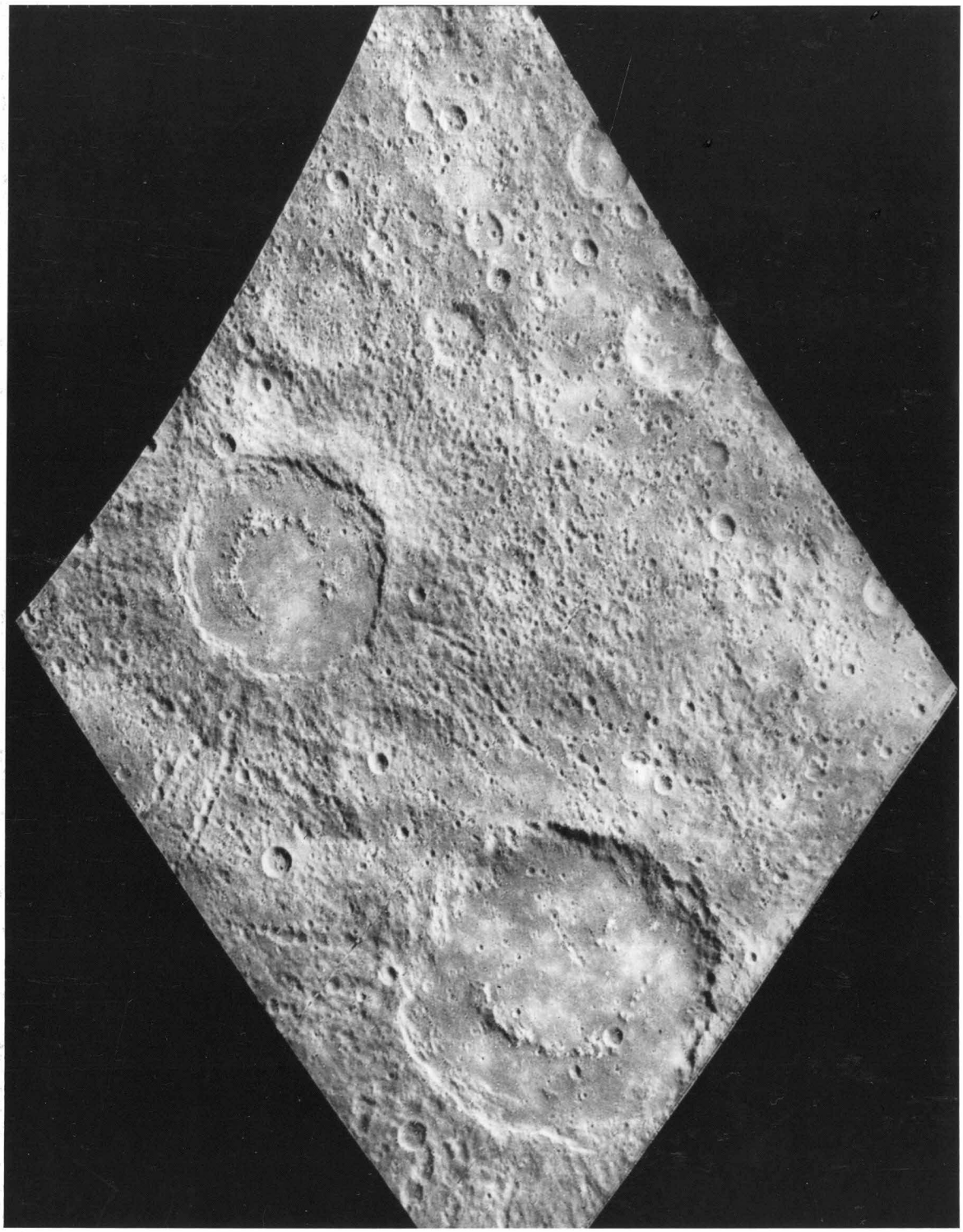

The varied and complex topographies associated with "ring" structures warrant a consideration of more than one generating mechanism. The paradigm of the multiringed basin is that there are (at least) *three valid models of ring formation.*

Rings can be produced late in the cratering process by gravitative adjustment toward equilibrium of the region surrounding the transient cavity. A concentric outer fault scarp or series of scarps develops. The critical difference between this type of scarp formation and slope instability or terrace formation is a sufficient decrease of strength with depth. Theoretical analysis of this ring formation mechanism (Melosh and McKinnon, 1978) is presented in section 3b.

Clear planetary examples (on the basis of morphology) of this type of ring would be the Cordilleran scarp of Orientale and the main scarp of the young basin on Ganymede (Gilgamesh, see figure 34), recently imaged by Voyager 2 (Smith *et al.*, 1976b). On such a scale the decrease in strength with depth is most likely related to thermal structure. The higher the internal temperature gradient, the more rapid the approach to a sizable fraction of the melting temperature with depth. The resulting lowered yield strengths and viscosities at a given depth lead to closer ring spacing. This may account for the difference in ring spacing and morphology between Gilgamesh and the older ring systems on Ganymede and Callisto. In general, planetary heat flow and thermal gradient should decline with time, and the lithosphere should thicken. This connection between lithosphere

evolution and multiringed basins is developed in detail in section 3c, with particular reference to Ganymede and Callisto.

The Prairie Flat explosion crater is illustrative of a second type of ring. Formed in alluvium (saturated at depth) by a 500 ton surface tangent TNT sphere, the resulting crater contained four concentric anticlines or rings (Roddy, 1977a). It is suggested that the floor materials fluidized and formed rings physically analogous to the hydrodynamic rings of Baldwin (1972) and Van Dorn (1968). However, the low viscosities required by the hydrodynamic model have thus far hindered its acceptance in geologic settings where there is no obvious fluid element. If the discussion of the origin of central peaks (section 2h) is applicable, then a similar hydrodynamic mechanism for peak-rings on the moon and elsewhere is possible. However, the origin of peak-rings is still quite uncertain, and will not be discussed further.

The nested ring model (Hodges and Wilhelms, 1978) relies on mechanical strength and/or shock impedance discontinuities at depth in the target which inhibit growth of the transient cavity below said discontinuties. Experimental realization is straightforward using unconsolidated/consolidated layering (Piekutowski, 1977). Small (<200 m) benched craters formed in mare regolith are almost certainly "nested" (Quaide and Oberbeck, 1968). Impact into sedimentary or volatile strata overlying competent igneous rock may also fulfill the physical criteria for this model. However, it is not clear whether

the subtle differences between igneous silicate lithologies will suffice. Furthermore, nested development of the great solar system basins implies massive gravitative adjustment.

Impact energy and geometry (effective depth of burst), planetary geologic structure, and gravity all play major roles in the formation of multiple rings. Some basins furnish clear examples to test detailed theory, others remain obscure, and a great deal of work remains. The three formation schemes are not exclusive. Combined hydrodynamic and gravitative adjustment have been proposed for Orientale (Roddy, 1977a; Head, 1977). Indeed, the pitted craters on Mars (Wood *et al.*, 1978) and Ganymede (Passey and Shoemaker, 1980), often resembling double ring basins, may require new mechanisms to account for their occurrence.

b) The Mechanics of Ringed Basin Formation

1. Introduction

Lunar basins are impact features which exhibit two or more concentric scarps or mountainous rings. They are generally larger than 300 km in diameter, although smaller examples are known. One of the rings is presumably the rim of the impact crater which formed the basin. The origin of the other rings is a much debated subject. Many authors have suggested that the rings are fault scarps produced by rapid collapse of the transient crater or by later collapse associated with magmatism (see the reviews of Hartmann and Wood [1971] or Howard *et al.*, [1974] for original references). Van Dorn (1968) proposed a "frozen tsunami" model, likening multiple rings to gravity waves produced by impact in an inviscid fluid. Others suggested that the rings reflect layering of material properties in the moon (Wilhelms *et al.*, 1977, and references therein).

The ratios of the radii of the rings has often been said to be a multiple of 2 or $\sqrt{2}$ (Baldwin, 1963; Hartmann and Wood, 1971), although there is considerable scatter in this relation (Howard *et al.*, 1974). On the other hand, there is evidence that the ratios of ring radii decrease with increasing basin size (Head, 1977).

In this letter we investigate the mechanics of ring formation by collapse or slumping. Two classes of models are presented in order to broaden the range of plausible mechanisms. In both classes, strength or resistance to deformation decreases with

depth. If this decrease is rapid enough,in either set of models, at least one concentric fault scarp forms. The ratio between the scarp radius and the crater radius varies between 1.2 and about 2.7 depending upon the model, and is thus in the range of observed radius ratios.

2. Extrusion Flow Models

The simplest way to model a decrease of strength with depth is by a two layer approximation. An upper layer, of thickness t, is treated as a thin, brittle, elastic plate. Below this layer is either a half-space (fig. 25a) or a thin layer (thickness d, $d/D \ll 1$; fig. 25b) of weaker or more deformable material.

Excavation of a crater of depth h and diameter D in the upper layer produces a free surface of zero pressure on the crater floor. Material distant from the crater at the same depth h is subject to a pressure ρgh, where ρ is the layer's density and g is the acceleration of lunar gravity. This pressure difference drives weak material in the lower layer toward the crater. The weak material is thus extruded out the crater floor, contributing to the filling of the initial cavity. As this material moves toward the crater it exerts a shear stress $\sigma^{b}_{rz}(r)$ on the base of the elastic plate. Since the shear stress on top of the plate must vanish, this basal traction is balanced by the radial stress $\sigma_{rr}(r)$ and the hoop stress $\sigma_{\varphi\varphi}(r)$ in the plate. The radial stress $\sigma_{rr}(\frac{D}{2})$ on the inner wall of the crater must also vanish, so that σ_{rr} starts from zero at radius $r = \frac{D}{2}$, then generally becomes tensional, reaching a maximum before it declines at large radius ($\sigma_{rr}(r) \sim 1/r^2$ for $r \gg \frac{D}{2}$; a consequence of axial symmetry). A concentric tension crack or normal fault (depending upon depth) should form where $\sigma_{rr}(r)$ first reaches the tensile strength of the elastic layer, which for simplicity we shall take to coincide with the tensional maximum of $\sigma_{rr}(r)$, at radius r_{max}. The hoop stress $\sigma_{\varphi\varphi}$ does

FIGURE 25: Schematic diagram of the major features of the extrusion flow models. In model (a) a fluid half space underlies a thin elastic slab of thickness t. The fluid flows toward the crater cavity (radius $\frac{D}{2}$), exerting shear stress $\sigma_{rz}^{b}(r)$ on the base of the elastic plate. Stress equilibrium requires that this be balanced by stresses $\sigma_{rr}(r)$ and $\sigma_{\varphi\varphi}(r)$ in elastic plate. The magnitude of these stresses are shown in the inset. σ_{rr} is tensional, while $\sigma_{\varphi\varphi}$ is compressive. The first tension crack or normal fault forms where σ_{rr} reaches its maximum value. Model (b) is similar, except that the fluid is confined to a thin layer of thickness d.

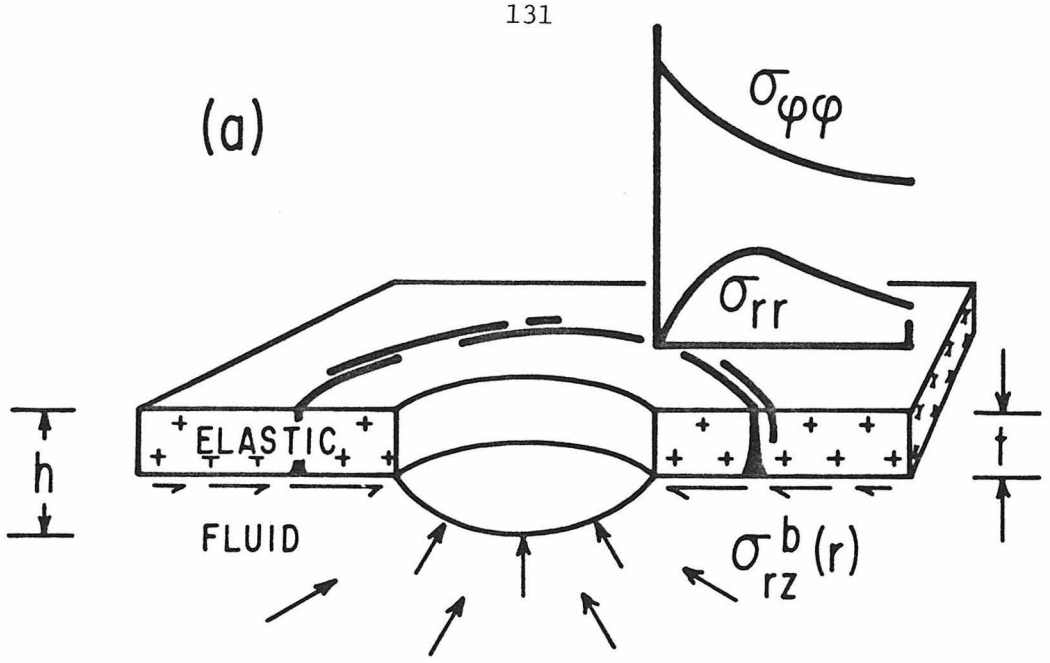
(a)
$\sigma_{\varphi\varphi}$
σ_{rr}
ELASTIC
FLUID
h
t
$\sigma^{b}_{rz}(r)$

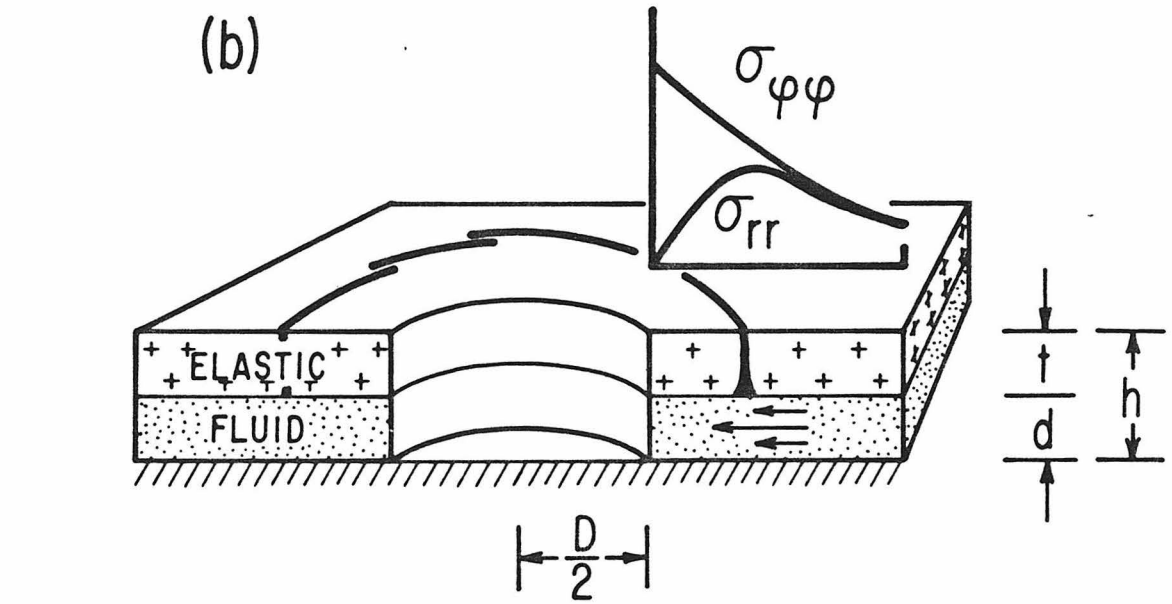
(b)
$\sigma_{\varphi\varphi}$
σ_{rr}
ELASTIC
FLUID
t
d
h
D/2

not vanish on the crater wall, is usually compressional, and also declines as $1/r^2$ for large radius (see insets in figs. 25a and 25b).

The basal shear stress $\sigma_{rz}^{b}(r)$ depends upon the rheology and nature of the flow in the layer beneath the crater. For example, the flow in a newtonian viscous half-space (viscosity η) beneath the crater approximates a dipole pattern, with

$$v_r = v_o\left(\frac{h}{r}\right)\cos\theta, \quad v_\theta = \frac{v_o}{2}\left(\frac{h}{r}\right)\sin\theta \tag{3.1}$$

where v_r and v_θ are flow velocities in a spherical (r, θ, φ) coordinate system, and $v_o = \rho g h^2/6\eta$. This flow pattern produces a shear stress on the base of the elastic plate which depends upon $1/r^4$;

$$\sigma_{rz}^{b}(r) = -\frac{\rho g h}{2}\left(\frac{h}{r}\right)^4 \tag{3.2}$$

Other rheologies, such as the power law creep which is likely to occur in the earth's mantle (Weertman and Weertman, 1975), change this radius dependence, as will other flow patterns. We can investigate a suite of these models by supposing a general relation

$$\sigma_{rz}^{b}(r) = -S\left(\frac{D}{2r}\right)^n \tag{3.3}$$

where S is a constant with dimensions of stress and n gives a general power law dependence of basal shear stress on radius (n=4 for extrusion from a newtonian half-space). Application of the equilibrium equations

for a thin elastic plate yields the radial stress in the plate

$$\sigma_{rr}(r) = \frac{DS}{2t}\left(\frac{2+\upsilon-n}{n^2-4n+3}\right)\left[\frac{(D/2r)^{n-3}-1}{(2r/D)^2}\right] \tag{3.4}$$

where υ is Poisson's ratio (equal to .25 in this work), and tensional stress is positive. Caution must be exercised for n=1 and 3, where (4) does not apply and logarithmic terms appear. This stress is largest at radius

$$r_{max}2/D = \left(\frac{n-1}{2}\right)^{1/n-3}. \tag{3.5}$$

Several values of $r_{max}2/D$ and $\sigma_{rr}(r_{max})$ are given in Table 5a. It appears that powers near 4 give values of $r_{max}2/D$ close to the observed ranges for multiple rings. The ratio $r_{max}2/D$ in (5) is not necessarily independent of crater radius, $\frac{D}{2}$, since the power n may itself be a function of D.

The dependence of σ_{rz}^{b} (r) on radius can also be evaluated for the extrusion of a newtonian fluid from a thin layer (fig. 25b) by the presence of the overburden ρgh. In this case σ_{rz}^{b} (r) is proportional to the modified Bessel function K_1 $(2r/\sqrt{3}\ d)$. Values of r_{max} and σ_{rr} (r_{max}) for several different layer thicknesses d/D are given in Table 5b).

Consideration of the $\sigma_{rr}(r_{max})$ values in Table 5 shows that the maximum tension is of order ρgh. Thus, if stresses of a few hundred bars are required to initiate fracture, the transient

TABLE 5

Results of Extrusion Flow Models

(a) Power Law Extrusion

Exponent n	r_{max} 2/D	$\sigma_{rr}(r_{max})/(\frac{DS}{2t})$
3	1.65	.0690
4	1.50	.0864
5	1.41	.0859
6	1.36	.0814
7	1.32	.0761

(b) Thin Layer Extrusion

Thickness, d/ D	r_{max} 2/D	$\sigma_{rr}(r_{max})/\rho gd$
.05	1.20	.763
.10	1.30	.558
.15	1.42	.426
.20	1.55	.330
.25	1.63	.257

crater must be at least a few tens of km deep, implying minimum diameters of hundreds of km. Moreover, since slumping quickly reduces the crater depth to a few km (Melosh, 1977), extrusion flow and ring formation must occur rapidly: slow isostatic adjustment of a crater a few km deep does not generate enough stress to produce concentric fractures.

This model does not adequately address the formation of more than one concentric fracture. If the first fracture relieved all of the tensional stress σ_{rr} (r) at r_{max}, then we could begin a new stress balance with σ_{rr} (r) = 0 at r_{max} instead of $\frac{D}{2}$, thus producing a second ring at a radius with the same ratio to r_{max} as $r_{max}^{2/D}$. However, there is little justification for this, since the first fracture will not relieve all of the stress.

3. Plastic Failure Models

Herein we examine ring formation by studying the gravitationally induced mechanical failure of large lunar craters for which the strength of the material surrounding the transient cavity decreases continuously with depth. The crater is considered to be a cylinder of depth h and diameter D. Owing to the axial symmetry of the situation the analysis is confined to an r-z plane. The moon's curvature is neglected. We utilize the mathematical theory of plasticity and assume the Tresca-Saint Venant yield criterion, i.e. the material possesses a cohesion strength c but no internal friction.

We have previously applied such a plastic analysis to craters formed in a half-space of uniform material properties (Melosh, 1977; McKinnon, 1978). An example calculation is shown in fig. 26a. Because the stress field is determined by a hyperbolic system of equations, solutions may be found by the method of characteristics. The form and extent of these intersecting sets of characteristics or slip lines are determined by the boundary conditions. In this case the crater floor is assumed to be failing and the principal stress direction is taken to be vertical under the crater rim at $z = h$, $r > \frac{D}{2}$. The zone which actually collapses is determined by the calculated vertical stress under the crater rim. Failure occurs when this stress is exceeded by the overburden pressure ρgh. The slip lines are also characteristics

FIGURE 26: Slip line field under a crater with a rectangular profile, depth/diameter ratio h/D = .1 and surface strength parameter $\rho gh/c_o$ = 100. Distances are normalized by the crater diameter D. The numerical calculations employed a much finer grid than that shown above. In (a) the strength gradient is zero. The extent of failure is given by the region under the crater rim where the calculated vertical stress is less than the overburden pressure ρgh (vertical arrows). (b) With a sufficiently negative strength gradient (here $\alpha = -0.6$) a singular surface in the slip line field forms under the rim, leading to normal faulting at the surface. The formation of these discontinuities, however, prevents the extension of the solution beyond the first model ring. In both cases the form of the slip line field is not a function of the depth/diameter ratio.

SLIP LINE FIELDS/RECTANGULAR BASIN PROFILE

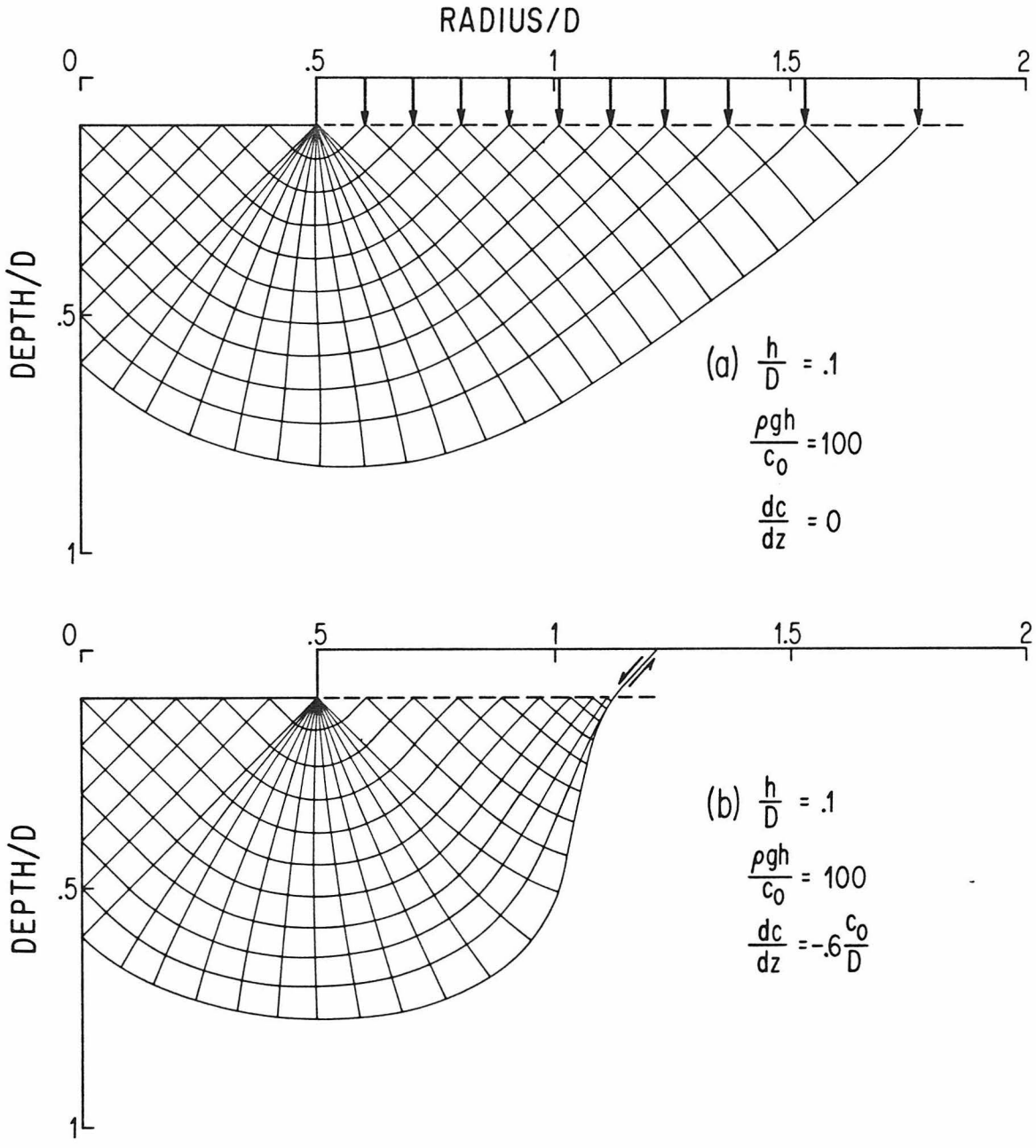

of the velocity field and represent possible faults since velocities may be discontinuous across them (Cox *et al.*, 1961; Kachanov, 1974).

We suppose that the cohesion decreases linearly with depth

$$c = c_o \left\{ 1 + \frac{\alpha}{D} (z - h) \right\} , \quad z > h \tag{3.6}$$

where $\alpha c_o/D$ is the strength gradient. This dependence is only a rough approximation to that of the real lunar crust, where strength is probably a complex function of depth. Friction is neglected because its inclusion prevents the collapse of large lunar craters (McKinnon, 1978), in contradiction to the observed evidence of slumping (Howard, 1974; Pike, 1977).

The effect of this strength decrease on the slip line field is apparent in fig.26b. For small negative values of the strength gradient the field contracts, particularly under the rim. When the strength gradient is sufficiently negative a singular surface develops where the slip lines run together, forming an envelope of characteristics. We interpret this envelope as the trace of a normal fault concentric to the crater. A similar singularity arises close to the rim crest for a crater of parabolic profile, representing the formation of the first slump terrace (Melosh, 1977).

The calculated ratio of the outer ring radius to the transient cavity radius is given in fig. 27 for a range of values of α and $\rho gh/c_o$, where c_o is the cohesion strength

FIGURE 27: Contours of the outer ring radius/transient crater radius ratio as a function of surface strength parameter $\rho gh/c_o$ and non-dimensional strength gradient $\frac{dc}{dz}\frac{D}{c_o}$ $(=\alpha)$ for h/D = .1. The dashed contour (~2.7) represents the maximum ring ratio for which an outer scarp may form. Ratios for basins formed at different scales with the same strength gradient (and constant c_o) lie on straight lines through the origin (dotted example). The stippled region in the lower left corner represents the stability transition of simple craters (model rectangular profile and $\frac{dc}{dz} = 0$) as discussed in Melosh (1977) and McKinnon (1978). The craters are stable for $\rho gh/c_o \leq 5.1$ and in full failure for $\rho gh/c_o \geq 8.4$. The lunar transient crater diameter scale at the top assumes $c_o \sim 20$ bars (see text).

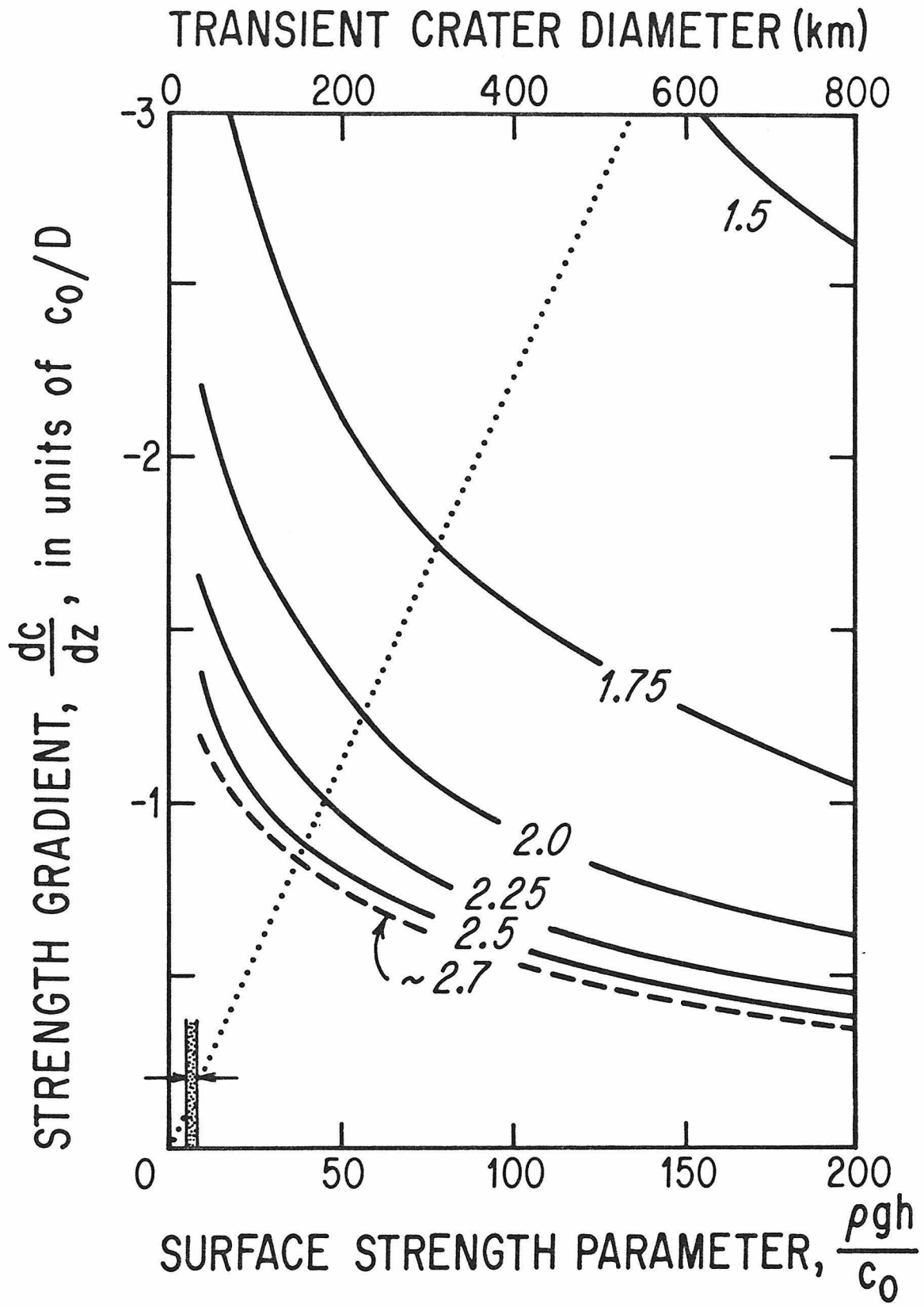
TRANSIENT CRATER DIAMETER (km)
0
200
400
600
800
-3
-2
-1
0
50
100
150
200
1.5
1.75
2.0
2.25
2.5
~2.7
STRENGTH GRADIENT, dc/dz, in units of c0/D
SURFACE STRENGTH PARAMETER, ρgh/c0

at the depth of the crater floor. The onset of ring formation is indicated. The ratios of ring radii decrease as either $\rho gh/c_o$ or α increase in magnitude. The depth/diameter ratio h/D does not play an explicit role in the slip line integration but does affect the ring ratios as the characteristic envelope is extended upwards through the rim region at an angle of 45° to the vertical (see fig.26b). Altering the depth/diameter ratio from 0.1 as illustrated in fig.27 would change all the ring ratio values by an identical amount.

Curves of constant strength gradient are straight lines through the origin of fig.27 (see dotted example) provided c_o is constant at all scales. On such a curve the smallest basins would have ring ratios between 2.0 and 2.7. Model basins with ring ratios near 2.7 have incipient characteristic envelopes forming at the edge of the slip line field and as such a recognizable fault scarp may not develop. Most of the ring ratios are between 2.0 and 1.5, clustering near 1.5 for the largest basins.

Care is recommended when attempting to plot lunar basin values on this figure. Transient cavity radii are usually inflated. It has been estimated that large lunar craters such as Copernicus owe up to one quarter of their present rim diameters to slumping (Shoemaker, 1962; Mackin, 1969). And lateral inhomogeneities in the lunar crust and upper mantle at the time of basin formation

will be reflected in varying strength gradients. There may also be a dependence of the strength gradient on crater size and differences in the ring ratios arising from using a rectangular crater profile rather than a parabolic one.

The $\rho gh/c_o$ scale in fig. 27 (bottom) is transformed to a transient crater diameter scale (top) for the moon assuming $c_o \approx 20$ bars. Cohesion strengths of this order are indicated by our previous analyses of crater slumping at smaller scales (and zero strength gradient). Limits on the stability of craters of rectangular profile are noted in the lower left hand corner of the diagram.

For larger basins the toe of the ring slump may thrust through the crater floor, forming an inner ring. In addition, once the first ring is in motion other outer concentric scarps may form. Our model cannot predict more than one ring fault as the development of the singular surface in the slip line field prevents the solution from being continued to the other side.

4. Discussion

The two classes of models presented above are very different in their basic approach. The one feature they have in common is the decrease of strength with depth. The extrusion flow models approximate this decrease by discrete layers: an elastic layer overlies a fluid or deformable layer. The plastic models assume a continuous (linear) decline. Concentric fault scarps develop about the initial crater in both models when the crater size and rate of decrease of strength with depth are large enough. Thus we believe that the formation of multiple rings about large lunar (or mercurian or martian) craters is due to the same cause: the strength of these planet's lithospheres decreases with depth.

The nature of this "strength" is problematic. In our previous work on the slumping of craters we showed that the sudden onset of slumping at ca. 15 km diameter on the moon, the flat floors of larger craters, and the 2 to 4 km widths of the slump terraces can all be explained by assuming a plastic yield criterion with cohesion $c_o \sim 20$ bars. It is remarkable that cohesions of this order also give an accurate estimate of the size at which multiple rings appear (150 - 300 km diameter, see fig.27). These results are obtained, however, only if very low values of internal friction ($< 2°$ in the case of slumping craters) are assumed. Such low internal friction might be a result of the dynamics of shock, unloading,and consequent relief of

overburden around the crater. The fact that multiple rings, forming up to 2.5 crater radii from the crater rim, require the same strength characteristics argues for a widespread relief of overburden pressures shortly after the impact. The mechanics of this process have not yet been worked out, so it is not clear what is implied by "decrease of strength with depth". Nevertheless, it appears that the plastic failure model provides a unified description of crater collapse from the smallest (15 km) to the largest (several hundred km) diameter craters.

Another view of the decrease of strength with depth may be taken. This view is motivated by the extrusion flow models. The temperature in a planet increases with depth, making its interior more deformable than its outer crust. The earth, for example, possesses a layer of low viscosity, the asthenosphere, at depths between 70 and ca. 200 km. Its effective viscosity is about 10^{19} - 10^{21} poise, at a stress level of a few bars. However, at the kilobar stress levels induced by a large impact crater cavity (initially about 20 km deep for a 100 km diameter crater), the viscosity of hot mantle material depends strongly upon stress (Weertman and Weertman, 1975). The effective viscosity at these stresses may be as low as 10^{13} - 10^{15} poise, resulting in Maxwell times of seconds to minutes. On this time scale the asthenosphere would flow as a viscous fluid, fulfilling the approximations

of the extrusion model. Concentric fractures may then develop as described above. This process could act in any planet with a large enough internal temperature gradient.

Extrusion flow may have caused the well-known concentric fissures about the Snowball explosion crater (Roddy, 1977b). The fluid element in this system was probably a stratum of water-saturated sand which fluidized after the explosion (a fact attested to by numerous sand blows and clastic dikes. See Jones [1977]).

Much work remains to be done before a full understanding of multiple rings is attained. However, we believe that our simple models demonstrate that multiple rings are due to gravitative collapse of the transient crater in the presence of decreasing strength with depth.

c) Evolution of Planetary Lithospheres: Evidence from Multiringed Basins on Ganymede and Callisto

1. Introduction

The recognition of multiring basins as major geological structures may be traced as far back as Gilbert's (1893) treatise on lunar physiography. Critical analysis has often focused on Orientale, the youngest and best preserved lunar multiring basin (e.g., Moore *et al.*, 1974). Such basins have also been found on Mars, Mercury, and the earth, but erosion, volcanic infilling, and burial have obscured fundamental understanding. The recent Voyager images have revealed exceptionally well preserved basin-ring systems on Ganymede and Callisto (Smith *et al.*, 1979a, 1979b). The systems observed on these objects are better developed and more extensive than any previously known. These newly discovered ring structures may thus significantly improve our understanding of large scale impact processes and ring formation mechanisms.

The hypervelocity collision of a massive object with a planetary target of sufficient self-gravity results in a complex, crudely axially symmetric structure. The variety of the observed ring structures suggests that no one physical mechanism can produce them all. Some rings form relatively symmetric annular swells, such as the inner rings of Schrödinger (moon) or Ahmad Baba (Mercury). The origin of these structures (termed peak rings by Head [1977]), which probably arise within the transient cavity of the crater, has been discussed

by Dence and Grieve (1979), Croft (1979), and McKinnon and Melosh (1980). In this paper discussion will be restricted to rings which form beyond the transient rim. On terrestrial planets such rings are asymmetric, with steep inward facing scarps and gentle outer slopes. On Ganymede and Callisto the morphology is more varied and the number of rings greater. The original crater has little topographic expression, usually only a central albedo feature (or palimpsest). All these characteristics are exhibited by the great Valhalla basin on Callisto (figure 28).

The purpose of this paper is to clarify the formation mechanism of these rings. To do this we must consider the planetary structural unit in which they form: the lithosphere. In turn we infer constraints on the lithospheric evolution of the two bodies. Both the thickness of this lithosphere and the viscosity of the underlying "fluid" asthenosphere must be defined appropriately with respect to the stress and strain rate regime of a basin-forming impact, as discussed in the following section.

The pattern of outer ring formation on the terrestrial planets has been theoretically examined by us (Melosh and McKinnon, 1978). Here the asymmetric rings are considered to be due to normal faulting. The sense of motion on these faults is to move crustal blocks radially inward toward the site of the impact crater (which is consequently partially filled), coupled with a rotation such that the basinward side of the scarp is downthrown. This is a direct consequence of the

FIGURE 28: The Valhalla basin-ring system on Callisto. A central high albedo palimpsest (∿600 km diameter) is surrounded by over two dozen "rings" extending up to ∿2000 km from the basin center. *Voyager 1 frame FDS 16422.11.*

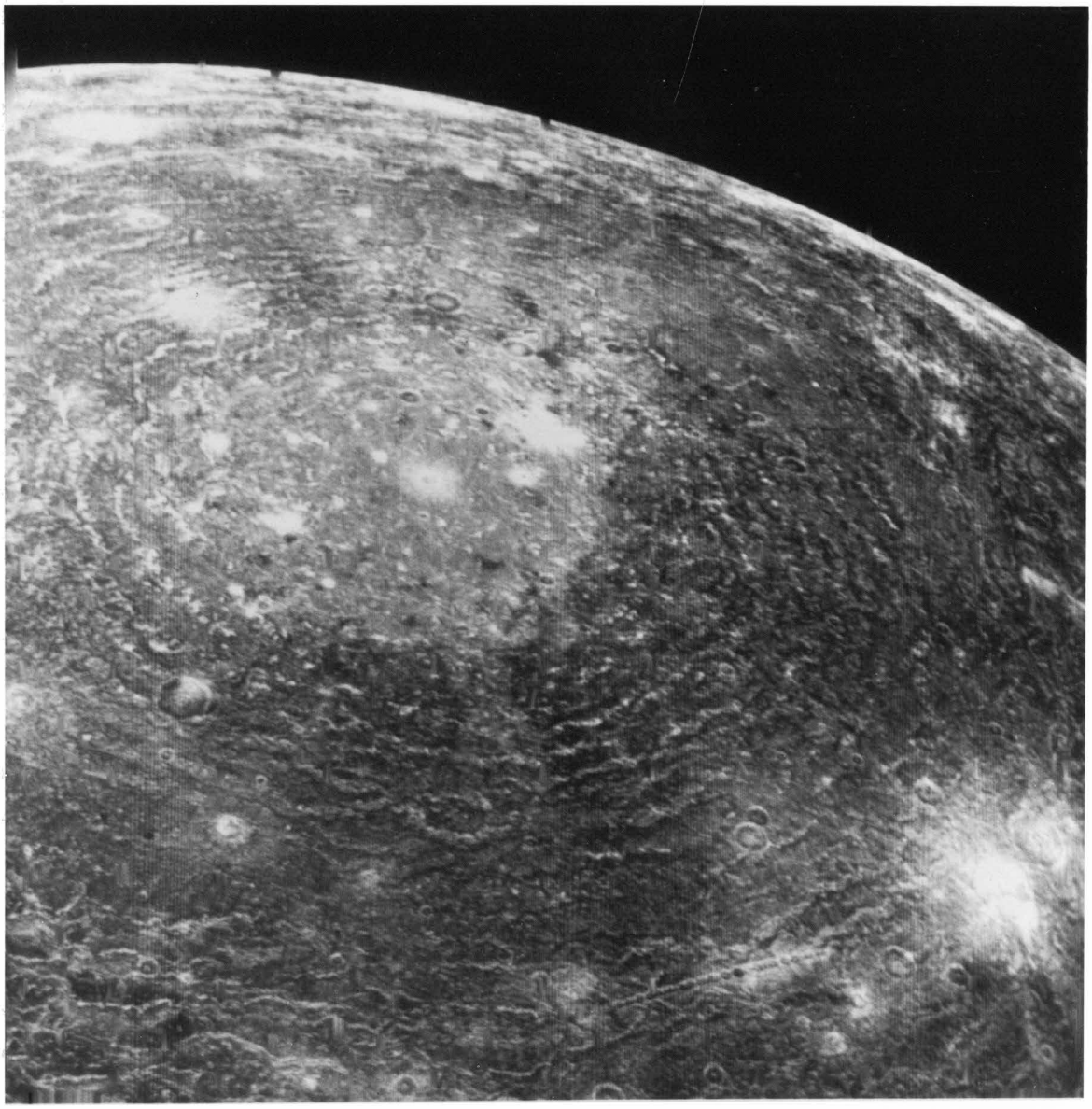

collapse of a crater when the excavation depth is commensurate with the lithosphere thickness. Traction on the base of the lithosphere, caused by the flow of deeper lying asthenospheric material towards the crater cavity results in radial extensional stress and concentric normal faults (i.e., the multiple rings).

In this section we semi-quantitatively extend the theory to very thin lithospheres. The number and spacing of the rings is a function of the crater diameter, lithosphere thickness, and lithosphere strength. When the lithosphere is very thin and weak, mechanical coherence is lost, and it is fractured and faulted in a multiply concentric pattern by the inward movement of asthenospheric material. The pattern of extension may change from normal and/or tensional faulting to graben formation with increasing distance from the original crater. Ring spacing should also increase, since the driving forces decrease with distance from the crater.

If the asthenosphere is very fluid (low viscosity), tsunami-like oscillations of the transient cavity propagate in the manner of Baldwin (1972) and Van Dorn (1968). The resulting stresses and strains should produce a pattern of radial and concentric fractures in a thin lithosphere. On the other hand, if the lithosphere is too thick, then multiple rings cannot form around a crater.

Interpretation of observed ring structures focuses on two units of Ganymedian heavily cratered terrain, Galileo Regio and Marius Regio (which may be preserved remnants on an ancient basin-ring system),

the young basin on Ganymede (Gilgamesh), the Valhalla basin, and a large (∿800 km diameter), newly discovered basin on Callisto. The picture of planetary thermal evolution that emerges involves a rapid lithospheric thickening (or downward migration of isotherms) at the end of terminal bombardment for Ganymede and an earlier "freezing down" for the lithosphere of Callisto. In addition, we infer that by the time of ring formation, solidification of the water mantles of the two bodies was essentially complete. While even small (< 50 km diameter) craters on the two planets are affected by the near surface temperature distribution via viscous degradation (Passey and Shoemaker, 1980), the multiringed basins, as the largest scale of impact feature, offer the deepest impact sampling of the planetary thermal regime.

2. Influence of thermal structure on rheology

We pose the question: To what extent does planetary thermal structure influence the formation of a large impact crater or basin? In terms of the compression or excavation stage (Gault *et al.*, 1968; Kieffer and Simonds, 1980), the influence is weak. Material strength effects are relatively unimportant at these large scales, and crater growth is limited only by gravitational work and dissipation, either viscous or frictional (Holsapple and Schmidt, 1979; Schmidt, 1980). We therefore expect a *transient* crater form approaching the traditional bowl shape, an aspect ratio (diameter/depth) $D/H \gtrsim 5$, a raised rim, and a spreading curtain of ejecta.

As excavation ends and the modification stage begins particle velocities decrease and deviatoric stresses decline to values on the order of lithostatic pressures appropriate to the transient crater. Since 70 km ≃ 100 MPa = 1 kbar on Ganymede (∿80 km on Callisto), craters several hundred kilometers across and tens of kilometers deep generate many hundred bars of stress. The rheological response of ice at these stresses as a function of temperature may be determined by the use of a deformation map. Based on an unpublished figure of M.F. Ashby, the map in figure 29 depicts the *dominant* steady-state creep mechanisms for ice of 1 cm grain size as a function of temperature and shear stress. Here only temperatures between 100 K and melting have been retained. Contours of strain rate ($\dot{\varepsilon}$) were derived from low pressure (1 bar $< \tau <$ 100 bar) and high temperature ($0.8\ T_m < T < T_m$)

FIGURE 29: Deformation map for ice of 10 mm grain size, derived from an unpublished figure of M.F. Ashby, and rheological zonation of an ice lithosphere in response to driving stresses of basin collapse (see text for discussion). Contours of strain rate are given as functions of temperature and shear stress. Dividing shear stress or normalized shear stress by 2x strain rate gives viscosity or Maxwell time, respectively. Terrestrial glacial ice is notoriously non-newtonian. The high deviatoric stresses due to the transient basin cavity (stippled) allow warm ice mantles to deform as viscous fluids on the time scale of collapse. A fluid asthenosphere/elastic lithosphere model is thus mechanically appropriate. For definiteness, the base of the lithosphere is established where the Maxwell time $\lesssim$1 s for several hundred bars of shear stress ($T \geqslant 240$ K). Note 10^2 kPa = 1 bar.

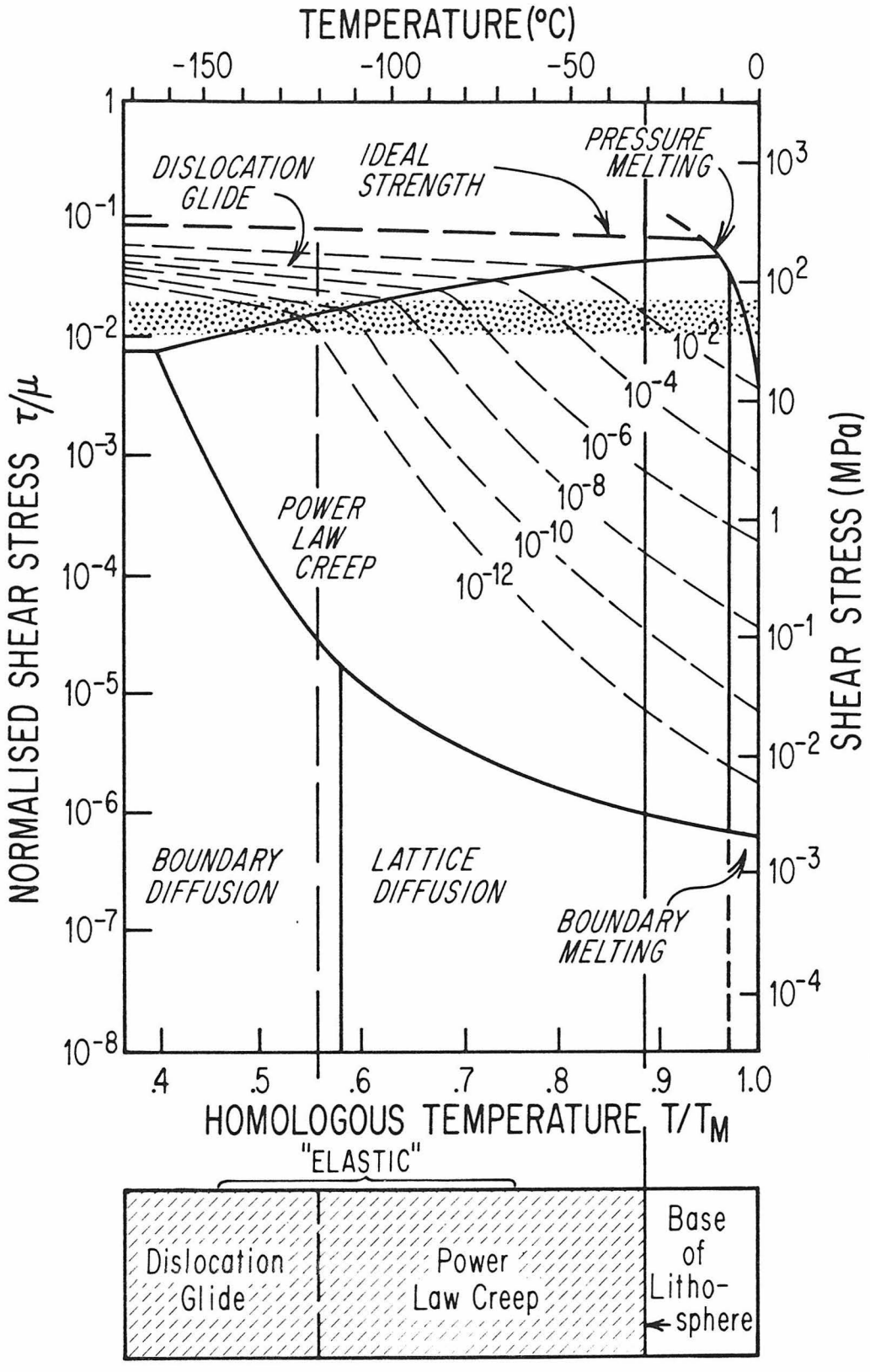

Rheological Zonation of the Lithosphere Due to Prompt Collapse of Transient Basin Cavity

data (e.g., Barnes *et al.*, 1971; and see Weertman, 1973 and Langdon, 1973). The stress regime set up by the transient cavity is indicated by a general stippling. The appropriate time scale to consider is that of prompt collapse, as penecontemporaneous slumping, wall failure, and floor failure are observed for terrestrial impacts (Grieve *et al.*, 1977; Kieffer and Simonds, 1980), and inferred for lunar craters on the basis of impact melt topology and from ejecta draping escarpments (Howard and Wilshire, 1975; Schultz, 1976). The free-fall time $\sqrt{2H/g}$, where g is the surface gravitational acceleration, serves as a lower limit to the prompt collapse time scale. As g = 142 cm/s^2 on Ganymede and 121 cm/s^2 on Callisto, this time is a few hundred seconds. The Maxwell relaxation time $t_m = \tau/2\mu\dot{\varepsilon}$, where μ is the shear modulus and τ is the applied shear stress, is defined as the length of time required for nonrecoverable creep to equal the elastic strain. Thus from figure 29, for the elevated stresses appropriate to the collapse of the transient crater, Maxwell times of less than 1 sec are possible for $T \gtrsim 240$ K. Thus the interior of an ice mantle planet (such as JIII or JIV [Cassen *et al.*, 1980]) need not be liquid to flow as a fluid under basin collapse stresses; the temperature need only be near the solidus. This statement, of course, can be generalized to other materials and other planets.

Using the Maxwell time criterion we analyze the collapse of the transient crater by a two-layer mechanical model of the behavior of the upper mantles of Ganymede and Callisto. Temperature is assumed to increase monotonically with depth. For $T \gtrsim 240$ K

(very short Maxwell times) the ice acts as a fluid on a time scale longer than a few seconds. The region below this approximate isotherm is termed the asthenosphere (see figure 29). The lithosphere lies between this isotherm and the surface ($T \sim 100$ K). Strain rates due to basal glide/dislocation climb (power law creep) or dislocation glide are low enough (large Maxwell times) that the lithosphere behaves elastically under prompt collapse. The lithosphere cannot match the large strains generated in the asthenosphere however, and fails in either a brittle or plastic manner.

It should be carefully noted that the definition of lithosphere and asthenosphere here is mechanical and depends upon time scale. It is not the same as conventional specification involving low stress and *geologic* time, nor is the lithosphere a thermal boundary layer.

Figure 29 should not be taken as the final word on ice rheology for large impacts. The purpose of this section is mainly to motivate the lithosphere/asthenosphere concept. As experiments and theory advance, figure 29 can be substantially updated. The boundary between the power law and glide regions is not well characterized and a lowering of the Peierls' stress could lead to an enlargement of the subsolidus temperature range which defines the asthenosphere. Other factors may affect the details, but not the concept. Saline contaminants, distributed interstitially or in brine pockets, act to decrease the viscosity (Reynolds and Cassen, 1979) and mechanical strength (Schwarz and Weeks, 1977). Rigorously speaking, the viscosities referred to in this paper are effective viscosities, $\eta = \eta_{eff} = \tau/2\dot{\varepsilon}$. Increased

hydrostatic pressure, working through the activation volume for diffusion (negative for ice I [Weertman, 1973]), lowers both the viscosity and the melting point. The effect, while small, is greatest for depths in excess of 100 km (Consolmagno and Lewis, 1976), where driving stresses from only the largest basin-forming impacts are expected to be important. The rheology of high pressure phases of ice, stable at depths below ∿150 km, is unknown and will not be considered further. Finally, a smaller grain size, which may not be unreasonable (Kuon and Jonas, 1973), affects viscosity by enhancing diffusional (Nabarro-Herring and Coble) creep. The line defect mechanisms are not sensitive to grain size, however, and probably dominate creep for the modification of basin scale impacts. None of these caveats seriously affect the viability of the lithosphere/asthenosphere rheological model.

3. Towards a theory of impact ring generation

As the basin cavity collapses, deformation concentrates in the asthenosphere defined above. We have previously analyzed such collapse assuming that excavation penetrates the lithosphere (Melosh and McKinnon, 1978). Driven by gravity, the asthenosphere flows as a viscous fluid towards the crater. A combination of this "extrusion" and rim slumping due to local gravitational instability of the crater walls fills the crater. The flow exerts a shear stress on the base of the lithosphere, which we model as a thin, brittle plate, and creates a state of radial tension. It is clear that the basal shear declines with radial distance from the crater. Thus, since the radial stress must approach zero at both the cavity rim and far away from the crater, a tensional maximum occurs at some intermediate distance. A compressional "hoop" stress accompanies the tensional radial stress. The absolute value of the "hoop" or circumferential stress is always greater than the radial stress. Thus a compressive hydrostatic state of stress is maintained in the lithosphere.

The observables are not stresses, of course, but the tectonic or fault patterns surrounding planetary impact basins. These are evaluated via the faulting criteria of E.M. Anderson (1951). When the hydrostatic stress is sufficiently compressive, planes of shear failure should develop at acute angles to the maximum compressive principal stress direction (circumferential) and parallel to the intermediate principal stress direction (vertical). We take as the formation radius (of the incipient shears) that of maximum radial

tension, as confining pressure and potential frictional effects are minimized there. Development of the fractures relieves the positive circumferential stress, which was solely a geometrical effect, a consequence of axial symmetry. Asthenospheric yielding continues apace, but now the lithosphere breaks along a circumferential line of intersecting shear planes and is downdropped and rotated toward the basin cavity. This *normal* fault is the asymmetric ring. Figure 30 depicts various modes of possible multiring basin genesis. The above description is illustrated by 30c. The figure is strictly schematic, with details such as rim slumping and ejecta still in motion omitted for clarity.

The full solution to the flow pattern in the asthenosphere, with stress and temperature dependent rheology, is formidable. It is therefore interesting to note that if simple newtonian viscosity is assumed, formation of the outer ring is predicted at 1.5 crater radii, close to the $\sqrt{2}$ spacing so often claimed.

Ring spacing is sensitive to lithosphere thickness. Examination of basin collapse for thicker lithospheres (unpierced by excavation), in which yielding of the lithosphere is determined by the use of a plastic potential (Kachanov, 1974) and parameterized by a cohesion strength that decreases linearly with depth, has shown that development of concentric normal ring faults at greater than two crater radii are *possible* (Melosh and McKinnon, 1978). The spacing increases with lithosphere thickness. The reason is straightforward: more lithosphere is available to distribute the applied shear. In planetary terms,

FIGURE 30: Ring formation as a function of lithospheric thickness (schematic). (30a) A very thin lithosphere fragments in response to collapse and continued oscillation of a transient cavity (dots) formed in a low viscosity asthenosphere (e.g., a liquid water mantle). (30b) For a fluid asthenosphere of sufficient viscosity (e.g., subsolidus ice) driving stress is due to collapse only. The lithosphere rifts in a multiply concentric manner. Radial extension features are supressed by compressive hoop stress. Tension cracks, normal faults, or graben may form depending on driving stress, asthenospheric strain, and ring curvature (see text). Spacing decreases away from basin center. (30c) For thicker lithospheres one or very few rings (actually irregular, steep inward facing scarps due to normal faulting) form. Deformation of the rim region is omitted for clarity. (30d) If the lithosphere is too thick, then there is no ring formation outside the transient cavity (dots). Crater collapse in the ultimate lithosphere, an elastic-plastic half-space, leads to "normal" large crater morphology, here represented by rim terraces, flat floor, and central pit.

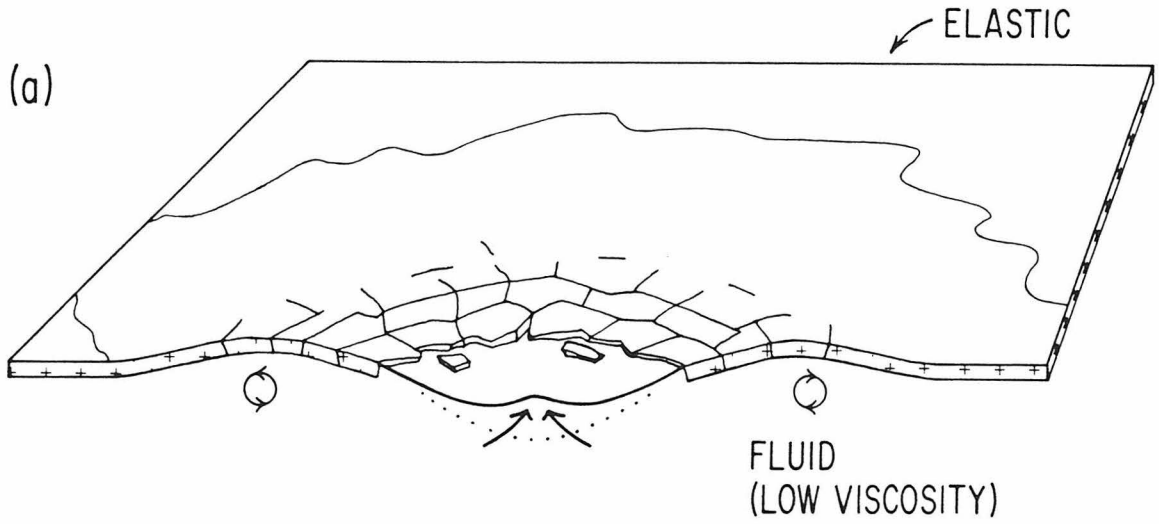
(a)
ELASTIC
FLUID
(LOW VISCOSITY)

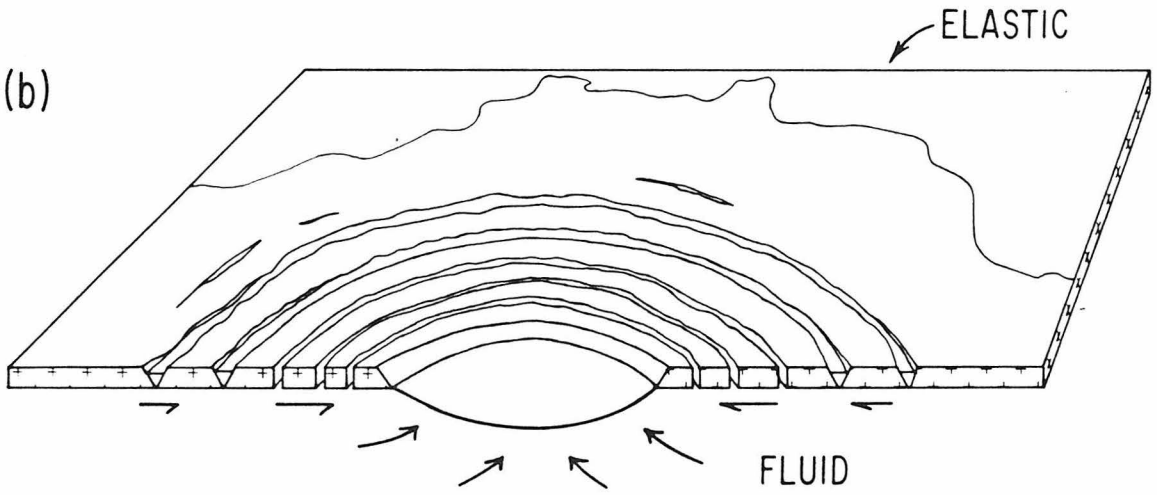
(b)
ELASTIC
FLUID

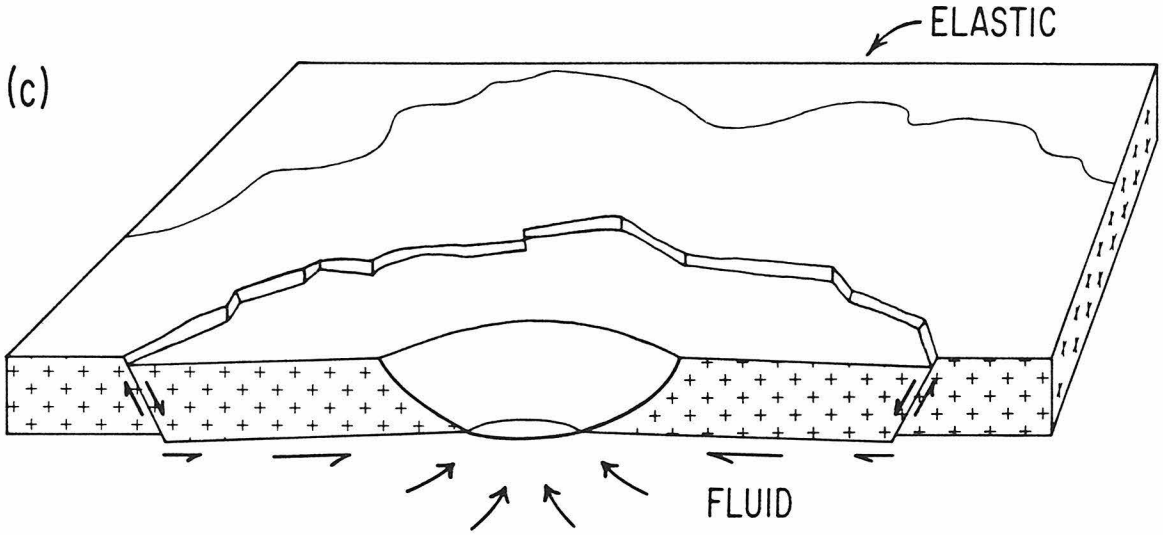
(c)
ELASTIC
FLUID

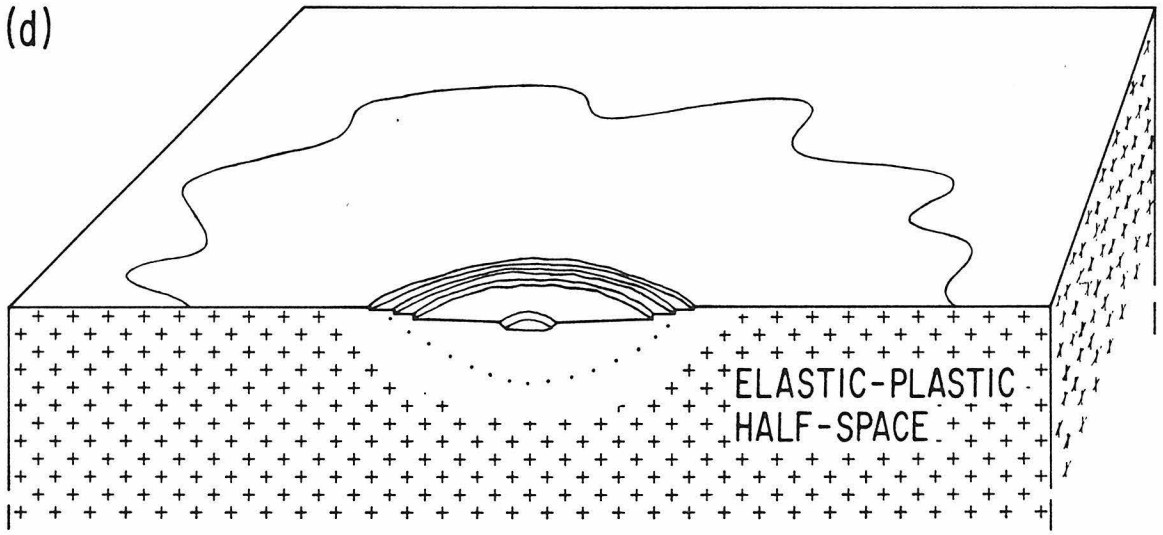
(d)
ELASTIC-PLASTIC
HALF-SPACE

the lower the temperature gradient, the deeper the extent of the strong layer or lithosphere, and the wider the ring spacing for a given scale of impact. Such relatively thick lithospheres may explain the ∿2 ring ratio for such basins as Grimaldi on the moon (Dvorak and Phillips, 1979).

If the lithosphere is too thick, outer ring formation does not take place. Collapse results in the more traditional morphology of figure 30d, i.e., uplifted flat floor, central pit, peak or peak ring, and slumped terrace wreath. Faulting outside the crater is confined to the rim region. In fact, the theoretical upper limit on the ring ratio for these lithospheres (the elastic-plastic half-space being the end member) may not be observable, but may be constrained by the zone of shock reduced material strength (deduced by Melosh [1977], McKinnon [1978], and Croft [1979]) surrounding the crater.

Our original thin lithosphere model does not prohibit formation of more than one ring, though the evaluation of stresses in a fractured lithosphere is non-trivial. However, the stresses imposed by the asthenospheric flow should everywhere exceed the strength of a *very thin* lithosphere. A multiply concentric ring pattern may then develop.

Consider such a pervasively faulted lithosphere of thickness t. We require the stress state to conform to a plastic yield limit. Therefore, we fix the radial stress at a maximum radial tension, τ_c. Stress equilibrium requires

$$\sigma_{rr,r} + (\sigma_{rr} - \sigma_{\phi\phi})/r + P_r/t = 0 \quad , \qquad (3.7)$$

where ϕ is the circumferential direction and P_r is the stress applied to the lithosphere. Let $P_r = -S(R/r)$, where R is the transient cavity radius, S is a constant having the dimensions of stress, and n describes a general power law behavior of the basal shear due to asthenosphere flow. The solution is simply

$$\sigma_{rr} = \tau_c \quad , \quad \sigma_{\phi\phi} = \tau_c - S(R/r)^n (r/t) \quad . \qquad (3.8)$$

$\sigma_{\phi\phi}$ should be compressive near the crater but will approach zero at a critical radius $r_c = R(SR/\tau_c t)^{1/n-1}$. For $r > r_c$ (provided $r_c > R$), $\sigma_{rr} > \sigma_{\phi\phi} > \sigma_{zz}$, and graben may nucleate. Once initiated, propagation in the ϕ-direction to form a concentric system is possible.

We do not know what value τ_c will reach, although we reason that it will be a small fraction of ρgt. This is because crevasse formation in response to tension acts to concentrate stress in the lower lithosphere. Graben spacing is in general controlled by lithosphere strength *and* thickness, assuming that the scale of graben formation is much larger than the average fracture scale. Driving stress decreases with radial distance, and we expect a concomitant increase in graben spacing.

The approximate solution above has a limited domain of applicability. Impacts of such magnitude as to cause lithospheric failure near 90° from "ground zero" could occur. As the radius of curvature

in the plane of the shell becomes infinite there, the hoop stress can be neglected and the general response to radial tension will be graben formation.

For $r < r_c$, significant circumferential compressive stress is present, leading to further movement along faults oblique to the radial direction. Normal faulting in the manner of thick lithosphere is possible, as well as concentric splitting, as radial strain is concentrated close to the crater.

In essence, strain instead of stress boundary conditions must be used close to the crater for the case of very thin lithospheres ($t << H$). For extremely thin lithospheres ($t <<< H$), strain is entirely determined by asthenospheric relaxation of the transient cavity and the lithosphere is passively rifted and dragged in by the flow. Nevertheless, compressive hoop stress supresses extension in the circumferential direction, and a pattern of multiple concentric fractures results. Low angle strike-slip faults may connect these concentric fractures, breaking the lithosphere near the crater into a large number of interdigitating blocks.

Figure 30b schematically illustrates the failure of a very thin lithosphere due to basin impact. A transition from lithospheric splitting to graben formation is shown, as well as an increase in intergraben spacing.

The preceding implicitly assumes a lithospheric response to transient cavity *relaxation* only, i.e., asthenospheric viscosities are such that the system is overdamped. This requires $\eta > \pi^{-3/2} \rho g^{1/2} r^{3/2}$

(Scott, 1967), where ρ = density and r = radius scale of disturbance. For ρ = 1 g/cm^3, g = 140 cm/s^2, and r = 150 km, $\eta \sim 10^{10}$ kg m^{-2} s^{-1} (10^{11} poise). Viscosities in the subsolidus asthenosphere of figure 29 are 10^9 - 10^{10} kg m^{-2} s^{-1}. Thus damping may be close to but not quite critical. Shear stress decreases as the crater shallows, however, and the effective viscosity should increase. Nevertheless, central oscillation of large impact structures on Ganymede and Callisto may be possible, especially in the presence of unequilibrated impact melt.

If the asthenosphere is predominantly liquid water, oscillatory behavior beyond the crater rim *must* be considered. The system is severely underdamped and a series of large amplitude waves should propagate radially outward from the cavity region (see Strelitz, 1979). A schematic travelling wave crest is shown in figure 31. The upward and outward phase of the particle motion induces circumferential and radial membrane tensions of comparable magnitude in the lithosphere. The lithosphere responds by fracturing in a concentric *and* radial pattern, i.e., a general disruption (as exemplified by explosions in river ice [Gaffney, 1980]). In figure 30a, a crater in low viscosity material collapses centripetally. The rim region, instead of stabilizing, continues to propagate outward, breaking up the (very) thin lithosphere.

Figure 30 provides a baseline for evaluating the response of a planet to basin scale impact as a function of rheological structure.

FIGURE 31: Response of thin lithosphere/asthenosphere to propagation of surface waves. Depending on type, the wave crest travels at the group or phase velocity. Particle trajectories are generally cyclic. Circumferential tension is coupled to phases of radial compression and vertical strain, leading to radial extension features.

HYDRODYNAMIC PROPAGATION

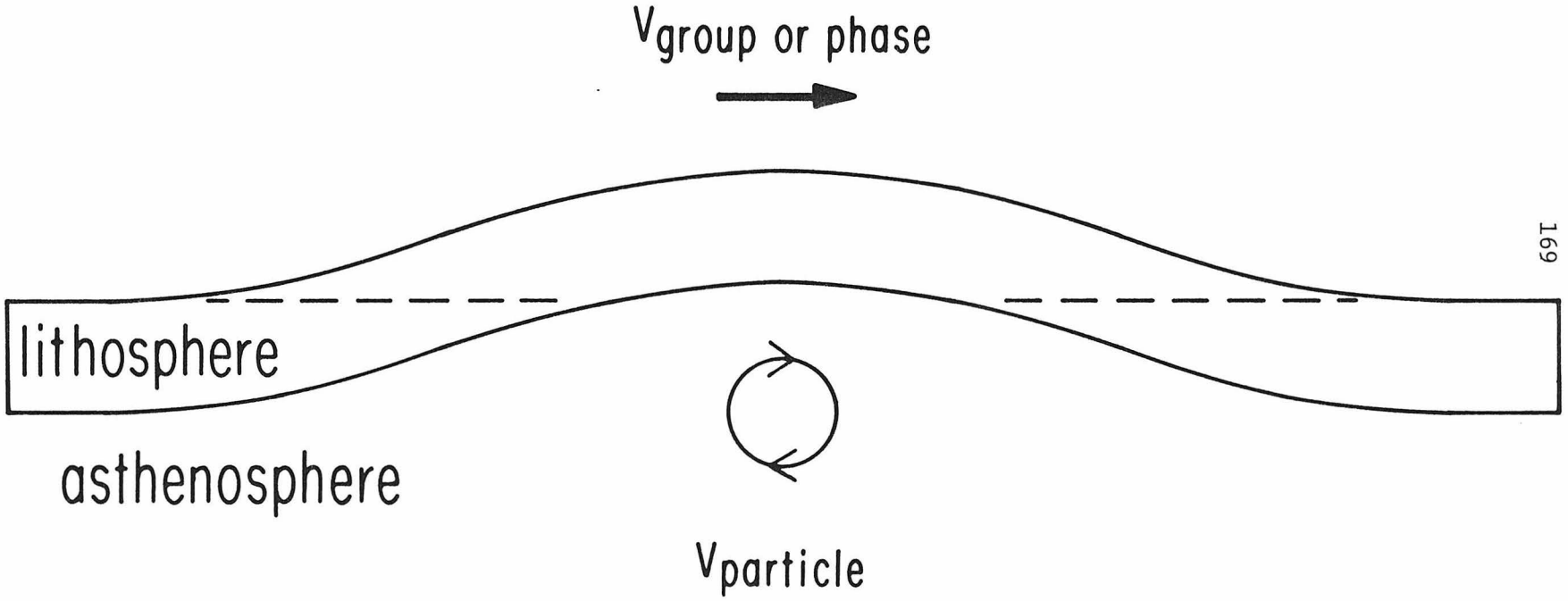

While by no means complete, we may draw several important conclusions as concerns the thermal state of Ganymede and Callisto at the time of basin formation.

4. Ringed basins on Ganymede and Callisto

i) Galileo Regio

The unit of ancient heavily cratered terrain on Ganymede, Galileo Regio (figure 32a), contains a pervasive system of rimmed furrows, describing regularly spaced, parallel to subparallel arcs (Smith *et al.*, 1979b; Lucchitta, 1980). A similar morphology is observed in adjacent Marius Regio to the west although *there* the pattern becomes indistinct to the southeast. This obscuration may be due to ejecta, either locally derived or from the basin scale impact proposed to generate this "ring system." Alternately, the furrows may not be impact related. Galileo Regio is thus a crypto-ringed basin Whatever the origin, the pattern is *tectonic*, and due to extension of the crust.

The extension took place before the period of grooved terrain formation, as evidenced by the abrupt transection relationships of the two units (see figure 32a, arrow). Extension must be prompt if basin related. Rapid formation is supported by the lack of furrow continuity across superposed craters (which apparently include nearly all craters in Galileo Regio, making them younger than the ring system [Smith *et al.*, 1979b]). There is, within the large palimpsest seen in figure 32a (top) and close-up in figure 33, a lineament which crosses the central region (figure 33, arrow) and presumably the original crater. Thus some reactivation of the extensional grid

FIGURE 32: Voyager images of portions of the Galileo Regio and Valhalla ring systems (centered near 8°N, 124°W and -10°S, 38°W, respectively). (32a) Comprising a unit of Ganymede's dark, heavily cratered terrain, Galileo Regio is dominated by arcuate rimmed furrows, interpreted here as graben. The unit is sharply truncated by grooved terrain (arrow). The large fresh pitted crater at right is 63 km in diameter. *Frame FDS 20638.33.* (32b) This section of the Valhalla basin-ring complex (centered near -10°S, 38°N) bears the greatest resemblance to the furrows of Galileo Regio. The rings transect palimpsests (example P, ∿100 km diameter) and craters (e.g., arrow X, ∿45 km diameter). One section of the rim of this crater is seen within the "furrow" (arrow R), thus the rings are graben. Tensional splitting of the two crater halves may also be ruled out planimetrically. *Frame FDS 16421.36* (filtered version).

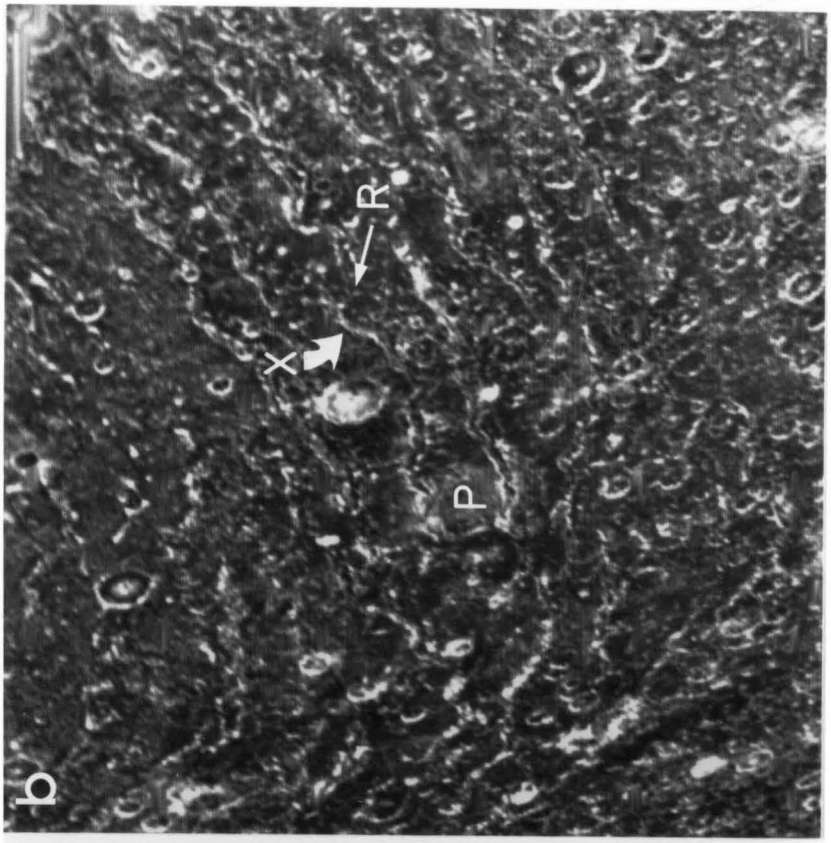
R
X
P
b

FIGURE 33: Voyager 2 image (centered near 19°N, 129°W) of large palimpsest in Galileo Regio. This impact feature is notable for a faint but recognizable lineament crossing the crater center (arrows), probably due to a reactivation of adjacent graben. *Frame FDS 20638.29.*

occurred. This may have been associated with grooved terrain formation, and would be due to renewed extension in any case.

If the furrows or rings are of impact origin, it is unlikely that they are analogous to tension cracks, i.e., due to lithospheric splitting, subsequent asthenospheric rafting, and filling with fresh asthenospheric material (ice). As furrows average 10 km in width and 50 km in separation, implied strains perpendicular to the strike of the furrows (radial) are ∿25%. Strains of this magnitude lead to enormous compressive stress in the circumferential direction,

$$\sigma_{\phi\phi} \sim E\zeta/a \tan(r/a) \quad , \tag{3.9}$$

where ζ = radial displacement, E = Young's modulus and a = planetary radius. For $E \sim 10^3 - 10^4$ MPa ($10^4 - 10^5$ bar) (Gold, 1977; Schwarz and Weeks, 1977), and $\zeta \sim 100$ km, $\sigma_{\phi\phi}$ ∿ thousands of bars even as r/a approaches $\pi/2$. Decoupled concentric zones of lithosphere, elastically unstable at these stresses, would buckle and fail brittlely, leading to a much more irregular pattern than observed. Of course, this objection is eliminated if the crack-ring system was split into wedges (of less than π in angular measure) prior to extension, but evidence for such later lithospheric motion has been shown to be weak.

A graben origin for the rings presents none of the above difficulties and is theoretically justifiable in terms of very thin lithosphere impact tectonics. The small wavelength irregularity of the graben may be due to nucleation in a thoroughly faulted lithosphere, as

discussed in the last section. The raised rims are probably yet another manifestation of viscous relaxation, over geologic time *within* the lithosphere, as has been proposed by Shoemaker (1980).

Independent of mode of origin, graben width may be used to estimate lithosphere thickness. If the graben are formed of intersecting normal faults of canonical 60° dip, then the ∿10 km width implies a lithosphere thickness of ∿10 km. We invoke the lithosphere/asthenosphere boundary as the mechanical discontinuity containing the graben vertices. Of all geometric corrections possible (see McGill and Stromquist, 1979), dip angle is the most severe. If steeper dips than 60° (common terrestrially) apply to the Galileo Regio graben, then our lithosphere thickness estimate is raised. However, it is mechanically implausible for t to be greater than the graben spacing (∿50 km).

ii) Gilgamesh

The Gilgamesh basin (figure 34) postdates formation of the Galileo Regio ring system, perhaps by several hundred million years (Smith *et al.*, 1979b). The central smooth depression (∿150 km diameter) is surrounded by several rings more characteristic of terrestrial planet basins. Most prominent is an irregular inward-facing scarp at ∿3 basin radii (arrows A). A discontinuous outer scarp is also seen (arrows B). Several approximately concentric lineaments lie with the main ring (e.g., white arrow), suggestive of further unresolved

FIGURE 34: Voyager 2 image of the multiringed basin Gilgamesh, on Ganymede (centered at -59°S, 130°W). Central flat-floored area (150 km diameter) is surrounded by blocky massifs, hummocks, and ejecta. Highly irregular scarp-rings are noted: outer discontinuous ring (arrows B), main ring (arrows A), and possible ring remnant (white arrow). Other short ~ concentric scarps are observable *Frame FDS 20638.14.*

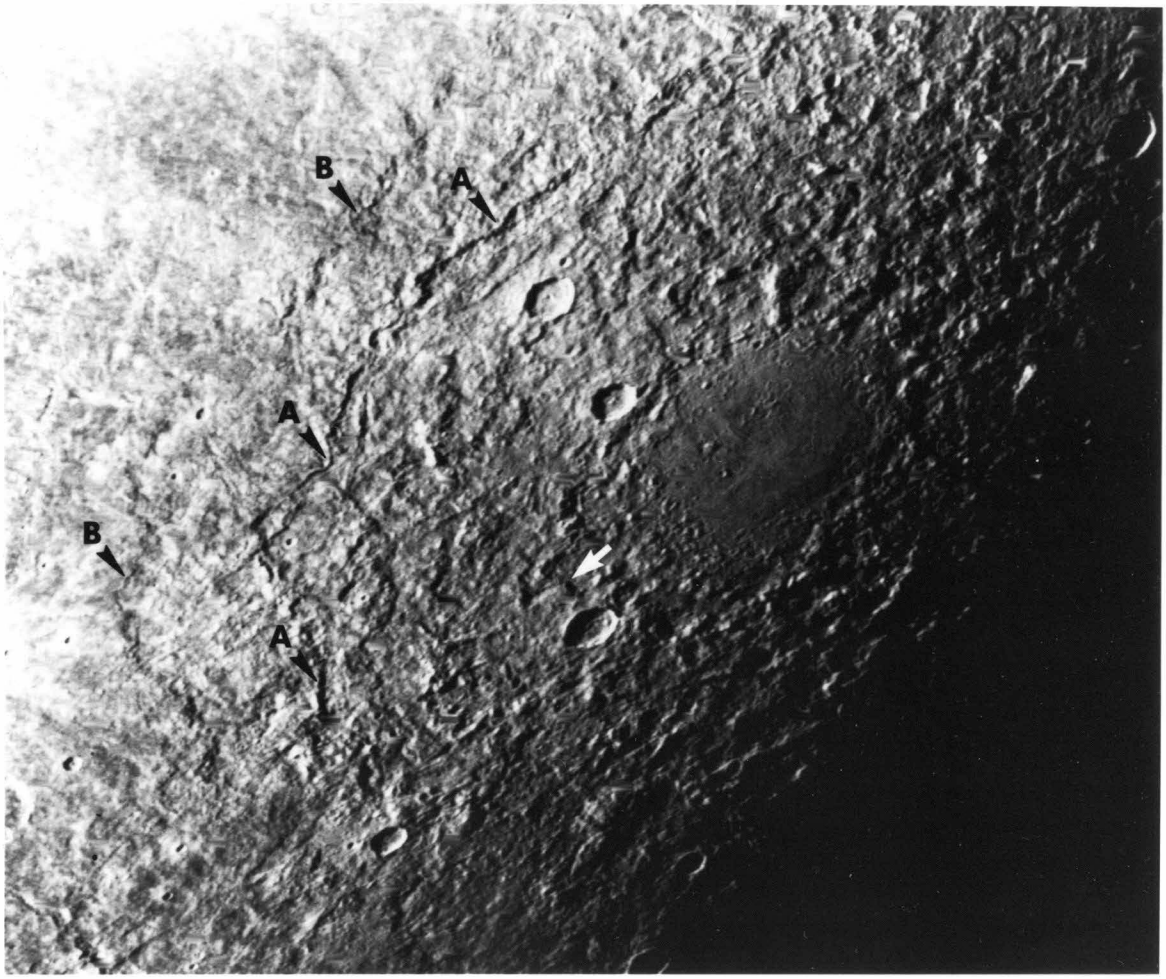
B
A
A
B
A

rings. The irregular scarp-like habit of these rings is indicative of the presence of a thicker lithosphere. A minimum estimate of one additional scarp between the main ring and the crater proper (inferred to be associated with the flat-floored basin center) gives a maximum ring ratio of ∿2. A theoretical estimate of lithosphere thickness (Melosh and McKinnon, 1978) gives t ∿ 75 km, subject to uncertainties in the cohesion strength of ice under impact. This is an upper limit. We take the transient depth (∿30 km) as the lower limit.

Other, tentatively identified multiringed basins on Ganymede (Malin, 1980) will not be discussed.

iii) Valhalla

There is no question as to an impact origin for the rings surrounding the central palimpsest of the Valhalla basin on Callisto (figure 28). Located up to 2000 km from the basin center, the rings are morphologically variable (Hale, 1980), and show little evidence for radial extensional strain exceeding a few percent. Figure 35 details the transection of impact craters by the rings in the northern quadrant of Valhalla. Only about a third of the craters observed postdate basin formation (Smith *et al.*, 1979b). The rings have been interpreted as flat-topped ridges (Smith *et al.*, 1979b). In figure 35a the presence of high albedo material within the crater (arrow), and adjacent to the ring, implies a reworking of the crust or flooding

FIGURE 35: Filtered Voyager 1 images of portions of the northern quadrant of the Valhalla basin-ring system (centered at 40°N, 34°W and 50°N, 50°W, respectively). (35a) Ring (or flat-topped ridge) cuts through a 40 km diameter crater (arrow) which appears to be "flooded." Within measurement error, there is no detectable ellipticity change in comparison with neighboring craters. Large strain would be manifested as such. *Frame FDS 16424.46.* (35b) An incipient ring is observed splitting a 60 km diameter crater. Crater slice appears rotated with respect to the main section. However, consideration of the uneven rim at the eastern edge (arrow, and also see frame FDS 16424.50 to eliminate reseau) shows there is no significant ellipticity change compared to nearby craters in full frame (not shown). *Frame FDS 16424.48.*

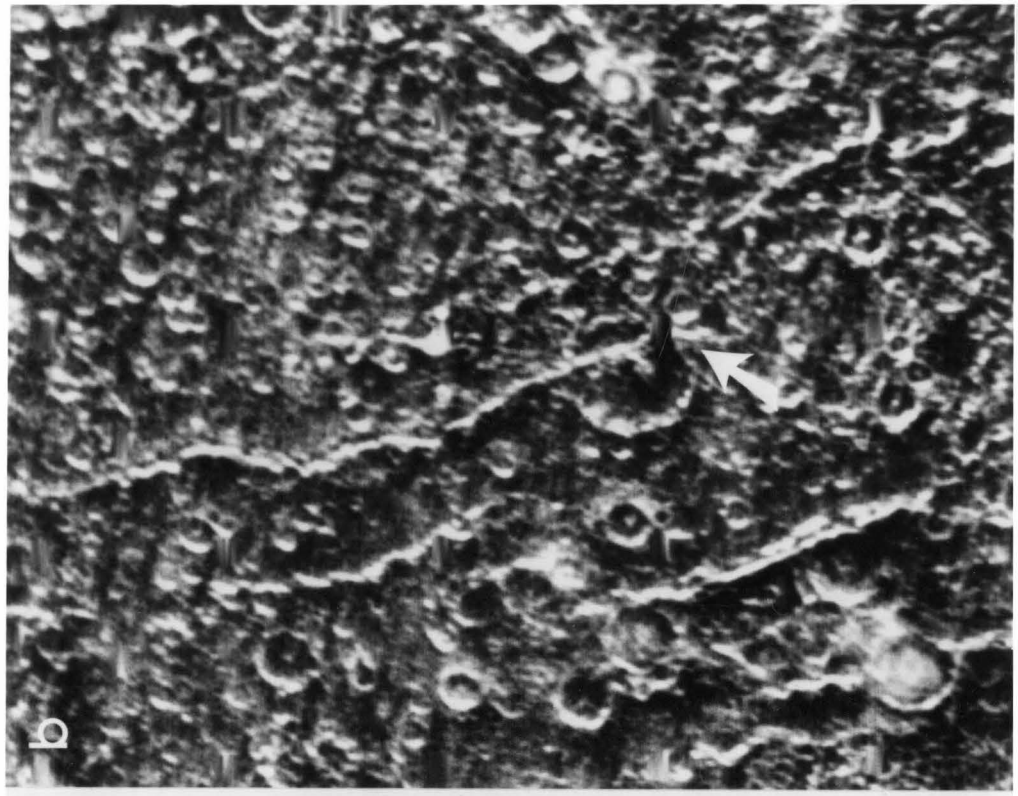
b

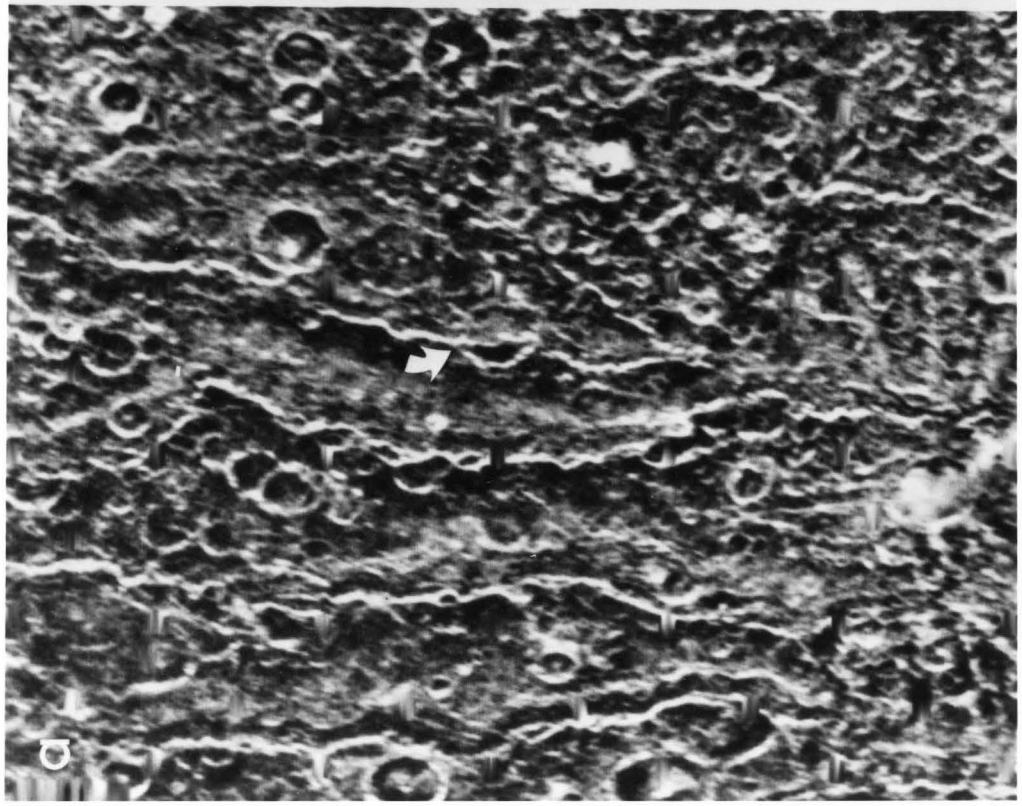
a

linked to ring generation. A 60 km crater appears split by an incipient "ridge" (figure 35a) whose terminus lies ∿30 km outside the rim.

Portions of the Valhalla ring system are clearly analogous to the furrows of Galileo Regio and are seen to be graben on the basis of transection relationships with older craters (figure 32b). Inter-graben spacing in this image is about 70 km. The best developed graben have widths of 15 to 20 km. Northeast of an ∿100 km diameter palimpsest (P), an approximately 45 km diameter crater (arrow X) is bisected by one of the ring graben. The northeast portion of the downdropped rim is still recognizable (arrow R). Interpretation of this double lineament as a tension crack is incompatible with the observed crater geometry. Lithosphere thickness at the time of ring formation is estimated at 15-20 km. Again, larger graben dip angles will increase this estimate.

Ring spacing increases with greater radial distance (fig. 28). This is also characteristic of the large multiringed basin Asgard (refer to Smith *et al.*, 1979b, fig. 28). Such an increase is expected as asthenosphere flow is weaker farther from the transient basin cavity.

iv) Unnamed Basin

A major multiringed basin, previously unrecognized, was discovered near the southern limit of Voyager 1 coverage of Callisto (figure 36). The ring system is degraded and hence presumably ancient, with a

FIGURE 36: Voyager 1 image of the southern limb of Callisto, and simplified sketch map of same region. Taken from a range of 350,000 km (and centered near -50°S, 30°W), it reveals a previously undetected multiringed structure (∿800 km diameter). Only Valhalla and Asgard are larger (on Callisto). At least ten bright rings or ring segments can be identified, with a central palimpsest of less than 200 km diameter extent. The rim diameter of the large, fresh, bright rayed crater Adlinda, whose ejecta overlaps the ring system, is near 150 km (see text), making the central craters of both impact structures comparable in scale. Adlinda, though, is much younger. *Frame FDS 16418.14* (filtered version).

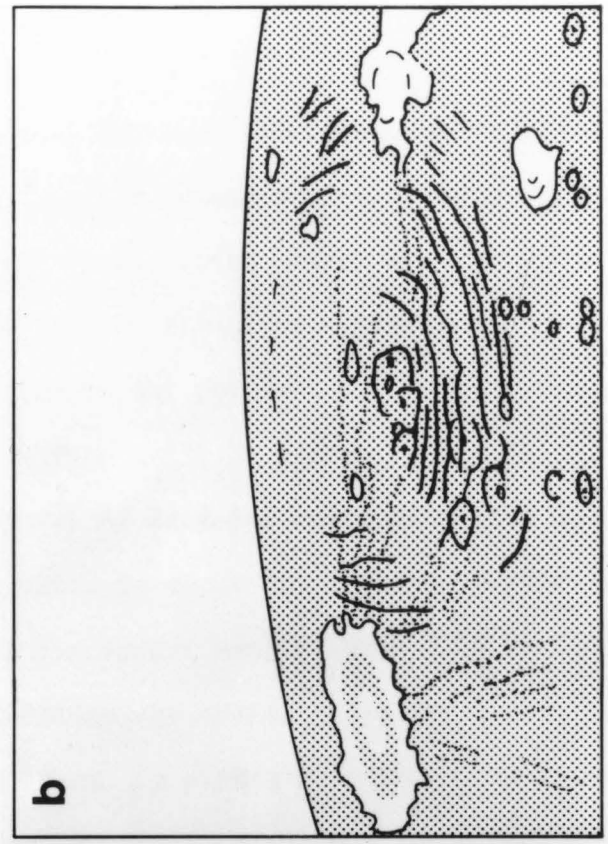
b


a

diameter of about 800 km. The rings appear as wavy concentric, bright lines (or line segments), becoming obscured to the east by ejecta from the fresh, bright rayed crater Adlinda. No further topographic relief or structure can be discerned at this resolution. A central crater is not obvious, but is constrained by the observed rings to lie within a 100 km radius.

The diameter of Adlinda, measured to the outer limit of the continuous ejecta, is about 280 km. The crater itself probably circumscribes the darker central ring (150 km diameter), as mature craters on Callisto are characterized by bright cores and rims, and dark floors. Thus, to within a factor of two, the central craters of Adlinda and the ringed basin *are the same size*. The ancient basin has at least ten rings associated with it. Adlinda, clearly much younger, has none.

5. Discussion

We may use the above descriptions to compare the thermal evolution of Ganymede and Callisto. By contrasting graben widths for Valhalla and Galileo Regio, Callisto's lithosphere thickness is found to be 1.5-2.0 times that of Ganymede *at the time of ring formation*. Crater density measurements of Strom *et al.* (1980) show Callisto to be three times as cratered as the oldest terrains on Ganymede (e.g., Galileo Regio). In addition, gravitational focusing by Jupiter enhances crater production by a factor of two relative to Callisto (Smith *et al.*, 1979b). Thus, in a normalized sense, Callisto is *six* times as cratered as Ganymede's dark ancient units. As the Valhalla ring system predates only one third of the observed craters, and Galileo Regio predates nearly all, there are *twice* as many superposed craters (normalized) on the Callistoan rings. Therefore, although the formation of the rings of Valhalla occurred earlier in the era of "terminal bombardment," Callisto was thermally more advanced. Critical isotherms had evolved to a greater depth and the lithosphere was thicker.

This conclusion is not sensitive to the mode of origin of the Galileo Regio rings, all that is required is an extensional tectonic regime. The large scale regularity of this fault system is frightening by terrestrial planet standards. It is apparently a young, uniform lithosphere. In fact, the above crater counts show that the first recorded tectonic event in the history of Ganymede *is* the formation

of these rings. Perhaps such regularity is not surprising for a freshly formed lithosphere.

The comparison of Ganymede and Callisto is also consistent with the observed long-lived tectonic activity on Ganymede, and regolith characteristics of the two bodies. There is no reason to suspect that the present crusts of Ganymede and Callisto are primordial. Both satellites are most likely to be partially or completely differentiated. Therefore the presence of silicate material on their surfaces is essentially due to meteoritic contamination. The lower albedo of Callisto compared to Ganymede's ancient cratered terrain (see Smith *et al.*, 1979a, fig. 12) is indicative of greater elapsed time since the stabilization of their respective crusts.

The concentric nature of the ring systems examined herein is accounted for by the theory of prompt basin collapse. No radial extension features or regions of general disruption are observed. Thus we may rule out hydrodynamic propagation (figure 30a) as the causative mechanism for the rings. This apparently eliminates the possibility that the mantles of Ganymede and Callisto were liquid at the time of formation. Lifetimes of liquid water mantles (Parmentier and Head, 1979; Cassen *et al.*, 1980) on Ganymede and Callisto (generally $< 5 \times 10^8$ years) are such that this result is quite plausible. This does not obviate consideration of zones of partial melt (slush) or brine acting as sources of magma (water). We note in passing that Europa may be a better candidate for such hydrodynamic rings (Cassen *et al.*, 1979).

For Ganymede, downward migration of isotherms continued throughout the waning stages of terminal bombardment, as evidenced by the greater estimates of lithosphere thickness for Gilgamesh. A similar but more advanced state of thermal evolution for Callisto is inferred at this time. Studies of viscous degradation of smaller impact features on Ganymede (<50 km diameter) by Passey and Shoemaker (1980) indicate a viscosity increase for the upper lithosphere during this era. Cooling of the mantle not only leads to lithosphere growth, but to a lower average temperature within the crust (or any spatially fixed unit).

The striking difference in morphology between Adlinda and the adjacent unnamed ringed basin on Callisto may be explained in terms of lithosphere evolution. The ring system dates to a time when the lithosphere was thin enough to allow formation of a multiple set of rings, spaced 30-40 km apart. Adlinda is a recent crater, and the lithosphere is too thick for development of even a single ring (at this scale of impact). The impact defined lithosphere is probably greater than 150 km at present.

The picture of lithosphere evolution from basin structure can be substantially improved. Portions of both satellites remain to be imaged. Several ring structures on Callisto were observed at poor resolution. Interpretation of portions of the Valhalla ring system remains problematical. It is clear that the small vertical topographic scale (a few hundred meters) is due to the low yield strength of ice

in both brittle and ductile failure. As such it is important to consider erosional modification to the primary ring structure. Proton and heavy ion sputtering of ice may be able to degrade topography of this scale (Lanzerotti *et al.*, 1978). Sublimation of ice may be significantly enhanced by the presence of dark fines. Mass loss rates may again be comparable to topography when integrated over geologic time (see Watson *et al.*, 1961). Thus what appear to be bright flat-topped ridges (Valhalla) may be remnants of an original ice filling of ring fractures. It is possible that differential sublimation, driven by strong albedo contrasts, left the ridges high standing. However, a full treatment of sputtering, sublimation, atmospheric transport, loss to the Jovian magnetosphere, etc. is beyond the scope of this paper.

Nevertheless, the better imaged ring systems contribute much needed information on planetary thermal state and lithosphere thickness (though for these bodies *krystallosphere* is probably a better term) as a function of time. The level of discrimination of key features is high for multiringed basins on Ganymede and Callisto, compared to their terrestrial planet counterparts. Rapid thermal evolution, coupled to ice rheology, accounts for the persistence of very thin lithospheres into terminal bombardment, and rapid thickening in the waning stages. This may not be entirely coincidental.

REFERENCES

Anderson, E.M. (1951). *The Dynamics of Faulting*. Oliver and Boyd, Edinburgh. 206 pp.

Baldwin, R.B. (1963). *The Measure of the Moon*. Univ. of Chicago Press, Chicago, Illinois. 488 pp.

Baldwin, R.B. (1972). The tsunami model of the origin of ring structures concentric with large lunar craters. *Phys. Earth Planet. Interiors 6*, 327-339.

Barnes, P., Tabore, D., Walker, F.R.S. and Walker, J.C.F. (1971). The friction and creep of polycrystalline ice. *Proc. Roy. Soc. Lond. A324*, 127-155.

Cassen, P., Peale, S.J. and Reynolds, R.T. (1980). On the comparative evolution of Ganymede and Callisto. *Icarus 41*, 232-239.

Cassen, P., Reynolds, R.T. and Peale, S.J. (1979). Is there liquid water on Europa? *Geophys. Res. Lett. 6*, 731-734.

Consolmagno, G.J. and Lewis, J.S. (1976). Structural and thermal models of icy Galilean satellites. In *Jupiter* (T. Gehrels, ed.), p. 1035-1051. Univ. of Arizona Press, Tucson.

Cox, A.D., Eason, D. and Hopkins, H.G. (1961). Axially symmetric plastic deformation in soils, *Phil. Trans. Roy. Soc. Lond. A254*, 1-45.

Croft, S.K. (1979). Interplanetary basin ring spacing: Consequence of gravity vs. strength scaling (abstract)? In *Lunar and Planetary Science X*, p. 245-247. Lunar and Planetary Institute, Houston.

Dence, M.R. and Grieve, R.A.F. (1979). The formation of complex impact structures (abstract). In *Lunar and Planetary Science X*, p. 292-294. Lunar and Planetary Institute, Houston.

Dvorak, J. and Phillips, R.J. (1979). Grimaldi: Bouguer gravity. Submitted to *J. Geophys. Res.*

Gaffney, E.S. (1980). Craters in ice and floating ice. Paper presented at IAU Colloquium No. 57, The Satellites of Jupiter, 13-16 May 1980, Kailua-Kona, Hawaii.

Gault, D.E., Quaide, W.L. and Oberbeck, V.R. (1968). Impact cratering mechanics and structures. In *Shock Metamorphism of Natural Materials* (B.M. French and N.M. Short, eds.), p. 87-99. Mono Book Co., Baltimore.

Gault, D.E., Guest, J.E., Murray, J.B., Dzurisin, D. and Malin, M.C. (1975). Some comparisons of impact craters on Mercury and the Moon. *J. Geophys. Res. 80*, 2444-2460.

Gilbert, G.K. (1893). The moon's face; a study of the origin of its features. *Bull. Phil. Soc. Wash. 12*, 241-292.

Gold, L.W. (1977). Engineering properties of fresh-water ice. *J. Glaciol. 19*, 197-212.

Grieve, R.A.F., Dence, M.R. and Robertson, P.B. (1977). Cratering processes: As interpreted from the occurrence of impact melts. In *Impact and Explosion Cratering* (D.J. Roddy, R.O. Pepin and R.B. Merrill, eds.), p. 791-814. Pergamon Press, New York.

Hale, W. (1980). A comparison of multiringed features on Callisto and the moon: Valhalla and Orientale. Paper presented at IAU Colloquium No. 57, The Satellites of Jupiter, 13-16 May 1980, Kailua-Kona, Hawaii.

Hartmann, W.K. and Wood, C.A. (1971). Moon: Origin and evolution of multi-ring basins. *Moon 3*, 3-78.

Head, J.W. (1977). Origin of outer rings in lunar multi-ringed basins. Evidence from morphology and ring spacing. In *Impact and Explosion Cratering* (D.J. Roddy, R.O. Pepin and R.B. Merrill, eds.), p. 563-573. Pergamon Press, New York.

Hodges, C.A. and Wilhelms, D.E. (1978). Formation of lunar basin rings. *Icarus 34*, 294-323.

Holsapple, K.A. and Schmidt, R.M. (1979). A material-strength model for apparent crater volume. *Proc. Lunar Planet. Sci. Conf. 10th*, 2757-2777.

Howard, K.A. (1974). Fresh lunar impact craters: Review of variation with size. *Proc. Lunar Sci. Conf. 5th*, 67-79.

Howard, K.A., Wilhelms, D.E. and Scott, D.H. (1974). Lunar basin formation and highland stratigraphy. *Reviews Geophys. and Space Phys. 12*, 309-327.

Howard, K.A. and Wilshire, H.G. (1975). Flows of impact melt at lunar craters. *J. Res. U.S. Geol. Survey 3*, 237-251.

Jones, G.H.S. (1977). Complex craters in alluvium. In *Impact and Explosion Cratering* (D.J. Roddy, R.O. Pepin and R.B. Merrill, eds.), p. 163-183. Pergamon Press, New York.

Kachanov, L.M. (1974). *Fundamentals of the Theory of Plasticity*. MIR Publishers, Moscow. 445 pp.

Kieffer, S.W. and Simonds, C.H. (1980). The role of volatiles and lithology in the impact cratering process. *Rev. Geophys. Space Phys. 18*, 143-181.

Kuon, L.G. and Jonas, J.J. (1973). Effect of strain rate and temperature on the microstructure of polycrystalline ice. In *Physics and Chemistry of Ice* (E. Whalley, S.J. Jones and L.W. Gold, eds.), p. 370-376. Univ. of Toronto Press, Canada.

Langdon, T.G. (1973). Creep mechanisms in ice. In *Physics and Chemistry of Ice* (E. Whalley, S.J. Jones and L.W. Gold, eds.), p. 356-361. Univ. Toronto Press, Canada.

Lanzerotti, L.J., Brown, W.L., Poate, J.M. and Augustyniak, W.M. (1978). On the contribution of water products from Galilean satellites to the Jovian magnetosphere. *Geophys. Res. Lett. 5*, 155-158.

Lucchitta, B.K. (1980). Observations on Ganymede I: Cratered terrain. Paper presented at IAU Colloquium No. 57, The Satellites of Jupiter, 13-16 May 1980, Kailua-Kona, Hawaii.

Mackin, J.H. (1969). Origin of lunar maria. *Geol. Soc. America Bull. 80*, 735-748.

Malin, M.C. (1980). Fables in Ganymede tectonics from morphologic studies. Paper presented at IAU Colloquium No. 57, The Satellites of Jupiter, 13-16 May 1980, Kailuna-Kona, Hawaii.

McGill, G.E. and Stromquist, A.W. (1979). The grabens of Canyonlands National Park, Utah: Geometry, mechanics, and kinematics. *J. Geophys. Res. 84*, 4547-4563.

McKinnon, W.B. (1978). An investigation into the role of plastic failure in crater modification. *Proc. Lunar Planet. Sci. Conf. 9th.*, 3965-3973.

McKinnon, W.B. and Melosh, H.J. (1980). Multiringed basins in the solar system: A "new" paradigm. In *Lunar and Planetary Science XI*, p. 708-710. Lunar and Planetary Institute, Houston.

Melosh, H.J. (1977). Crater modification by gravity: A mechanical analysis of slumping. In *Impact and Explosion Cratering* (D.J. Roddy, R.O. Pepin and R.B. Merrill, eds.), p. 1245-2160. Pergamon Press, New York.

Melosh, H.J. and McKinnon, W.B. (1978). The mechanics of ringed basin formation. *Geophys. Res. Lett 5*, 985-988.

Moore, H.J., Hodges, C.A. and Scott, D.H. (1974). Multiringed basins - illustrated by Orientale and associated features. *Proc. Lunar Sci. Conf. 3rd*, 71-100.

Parmentier, E.M. and Head, T.W. (1979). Some possible effects of solid-state deformation on the thermal evolution of ice-silicate planetary bodies. *Proc. Lunar Planet. Sci. Conf. 10th*, 2403-2419.

Passey, Q.R. and Shoemaker, E.M. (1980). Craters and basins on Ganymede and Callisto: Morphological indicators of crustal evolution. Submitted to *The Satellites of Jupiter* (D. Morrison, ed.). Univ. of Arizona Press, Tucson.

Piekutowski, A.J. (1977). Cratering mechanisms observed in laboratory-scale high-explosive experiments. In *Impact and Explosion Cratering* (D.J. Roddy, R.O. Pepin and R.B. Merrill, eds.), p. 1245-1260. Pergamon Press, New York.

Pike, R.J. (1977). Size dependence in the shape of fresh impact craters on the moon. In *Impact and Explosion Cratering* (D.J. Roddy, R.O. Pepin and R.B. Merrill, eds.), p. 489-509. Pergamon Press, New York.

Quaide, W.L. and Oberbeck, V.R. (1968). Thickness determinations of the lunar surface layer from lunar impact craters. *J. Geophys. Res. 73*, 5247-5270.

Reynolds, R.T. and Cassen, P.M. (1979). On the internal structure of the major satellites of the outer planets. *Geophys. Res. Lett. 6*, 121-124.

Roddy, D.J. (1977a). Large-scale impact and explosion craters: Comparisons of morphological and structural analogs. In *Impact and Explosion Cratering* (D.J. Roddy, R.O. Pepin and R.B. Merrill, eds.), p. 185-246. Pergamon Press, New York.

Roddy, D.J. (1977b). Tabular comparisons of the Flynn Creek impact crater, United States, Steinheim impact crater, Germany, and Snowball explosion crater, Canada. In *Impact and Explosion Cratering* (D.J. Roddy, R.O. Pepin and R.B. Merrill, eds.), p. 127-162. Pergamon Press, New York.

Schmidt, R.M. (1980). Meteor crater-implications of centrifuge scaling (abstract). In *Lunar and Planetary Science XI*, p. 984-986. Lunar and Planetary Institute, Houston.

Schultz, P.H. (1976). *Moon Morphology*. Univ. Texas Press, Austin.

Schwarz, J. and Weeks, W.F. (1977). Engineering properties of sea ice. *J. Glaciol. 19*, 499-531.

Scott, R.F. (1967). Viscous flow of craters. *Icarus 7*, 139-148.

Shoemaker, E.M. (1962). Interpretation of lunar craters. In *Physics and Astronomy of the Moon* (Z. Kopal, ed.), p. 283-357. Academic Press, New York & London.

Shoemaker, E.M. (1980). Geologic history of Ganymede. Paper presented at IAU Colloquium No. 57, The Satellites of Jupiter, 13-16 May 1980, Kailua-Kona, Hawaii.

Smith, B.A., Soderblom, L.A., Johnson, T.V., Ingersoll, A.P., Collins, S.A., Shoemaker, E.M., Hunt, G.E., Masursky, H., Carr, M.H., Davies, M.E., Cook, A.F., Boyce, J., Danielson, G.E., Owen, T., Sagan, C., Beebe, R.F., Veverka, J., Strom, R.G., McCauley, J.F., Morrison, D., Briggs, G.A. and Suomi, V.E. (1979a). The Jupiter system through the eyes of Voyager 1. *Science 204*, 13-32.

Smith, B.A., Soderblom, L.A., Beebe, R., Boyce, J., Briggs, G., Carr, M., Collins, S.A., Cook, A.F., Danielson, G.E., Davies, M.E., Hunt, G.E., Ingersoll, A., Johnson, T.V., Masursky, H., McCauley, J., Morrison, D., Owen, T., Sagan, C., Shoemaker, E.M., Strom, R., Suomi, V.E. and Veverka, J. (1979b). The Galilean satellites and Jupiter: Voyager 2 imaging science results. *Science 206*, 927-950.

Strelitz, R. (1979). Meteorite impact in the ocean. *Proc. Lunar Planet. Sci. Conf. 10th*, 2799-2813.

Strom, R.G., Woronow, A. and Gurnis, M. (1980). Crater populations on Ganymede and Callisto. Submitted to *J. Geophys. Res.*

Van Dorn, W.G. (1968). Tsunamis on the moon? *Nature 220*, 1104-1107.

Watson, K., Murray, B.C. and Brown, H. (1961). The behavior of volatiles on the lunar surface. *J. Geophys. Res. 66*, 3033-3045.

Weertman, J. (1973). Creep of ice. In *Physics and Chemistry of Ice* (E. Whalley, S.J. Jones and L.W. Gold, eds.), p. 320-337. Univ. of Toronto Press, Canada.

Weertman, J. and Weertman, J.R. (1975). High temperature creep of rock and mantle viscosity. *Ann. Rev. Earth Planet. Sci. 3*, 293-315.

Wilhelms, D.E., Hodges, C.A. and Pike, R.J. (1977). Nested-crater model of lunar ringed basins. In *Impact and Explosion Cratering* (D.J. Roddy, R.O. Pepin and R.B. Merrill, eds.), p. 539-562. Pergamon Press, New York.

Wood, C.A., Head, J.W. and Cintala, M.J. (1978). Interior morphology of fresh martian craters: The effects of target characteristics. *Proc. Lunar Planet. Sci. Conf. 9th*, 3691-3709.

IV. CALORIS: RING LOAD ON AN ELASTIC LITHOSPHERE

a) Introduction

The Caloris basin on Mercury (figure 37) is defined by the outline of the Caloris Montes scarp, with a radius of 650 km. Within the basin lies a plains unit that has subsided and undergone compressional tectonics as revealed by the ridge pattern throughout the basin. Subsequently this unit was uplifted and extended, as evidenced by the graben and graben-like fissures that form a rough concentric pattern within the basin. Beyond the basin rim lie the *smooth plains*, emplaced over the usual impact derived units in a annulus ~2 basin radii wide (actually inferred from images of half the basin and supplementary radar data [Zohar and Goldstein, 1974]). From their distribution, extent, and youth (younger than the central plains), they are thought to be volcanic (Strom *et al.*, 1975).

Caloris is positioned close to the axis of minimum moment of inertia, i.e., the long axis responsible for the tidal resonant locking with the sun at perihelion (Goldreich and Peale, 1966). This led Melosh and Dzurisin (1978) to propose that an uncompensated mass or mascon is associated with the basin. As the basin floor appears to be in extension, the mascon could not be centrally concentrated as with the lunar maria, but may be associated with the smooth plains surrounding the basin. This work examines the effects of such an annular load and concludes that it drove the extension and uplift within the basin and contributed to the compressive tectonics outside.

FIGURE 37: Caloris Basin, Mercury. A discontinuous annulus of ejecta of the *Caloris group* surrounds the basin (1300 km diameter measured to the Caloris Montes rim) and is overlain by vast tracts of *smooth plains* (Guest and Greeley, 1979; Schaber and McCauley, 1980). These plains are thought to be younger than the *Caloris floor plains* (Trask and Guest, 1975). A tectonic pattern of ridges, scarps, lineaments, and troughs are observed on all units. *Mariner 10 photomosaic.*

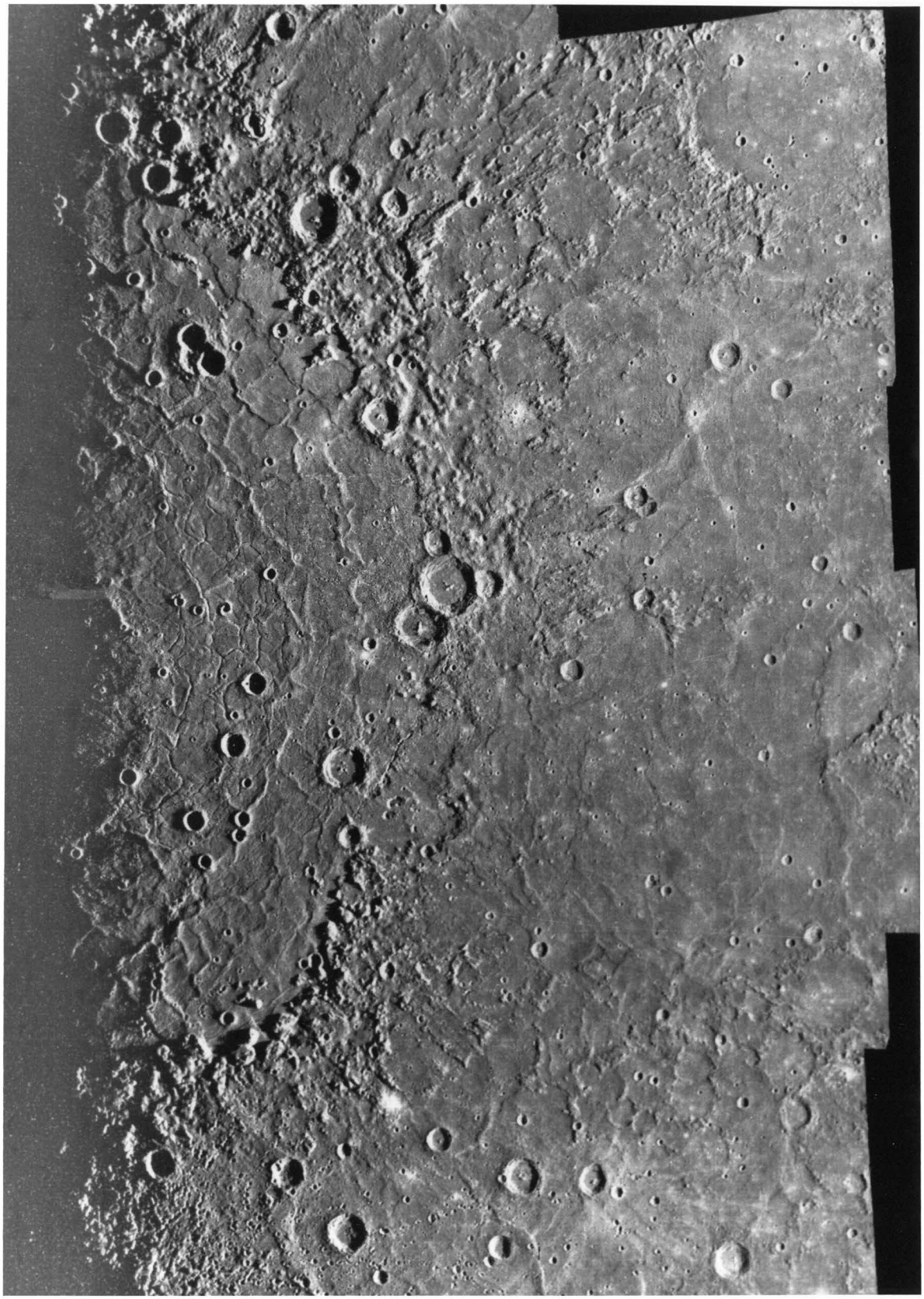

b) Mathematical Formulation

The mechanical analysis is formulated in terms of an elastic lithosphere floating on a planetary interior whose rheological response over geologic time is that of a fluid (figure 38). Details are given in the appendix. Cylindrical symmetry is assumed for simplicity. The analytic form of the load

$$\sigma_{zz}\Big|_{z=0} = -L(r/2a)^4 \exp\{-r^2/2a^2 - 2\} \qquad (5.1)$$

nicely approximates the smooth plains distribution, peaking at $r = 2a$ (where $\sigma_{zz}|_{z=0} = -L$, compression being negative). The basin radius is a. The lithosphere thickness is H. As the two-layer approximation is mechanical, not compositional, no density contrast $\Delta\rho$ is assumed. The iron core of the planet, $\sim$600 km down (Solomon, 1976) is treated as part of the fluid interior in this problem.

With the boundary conditions suitably defined; loaded on top, stress free on the bottom; the elastic solution in the lithospheric plate can be found. Buoyancy is properly taken into account. Curvature is parameterized, as liquid reaction dominates the problem. Computation of stresses and elastic strains allows an evaluation of surface tectonic style, gravity anomalies, etc. *as a function of lithospheric thickness.*

Physical constants appropriate for Caloris are used, i.e., density $\rho = 3$ g/cm^3, gravitational acceleration $g = 370$ cm/s^2, Young's modulus $E = 8 \cdot 10^{11}$ dyne/cm^2, and planetary radius $R = 2440$ km.

FIGURE 38: Ring load geometry. Floating elastic lithosphere of thickness H responds to annular load of smooth plains, analytically approximated by a quartic polynomial weighted Gaussian (half-width 2a). Maximum load is L. Surface displacement is $u_z(r)$.

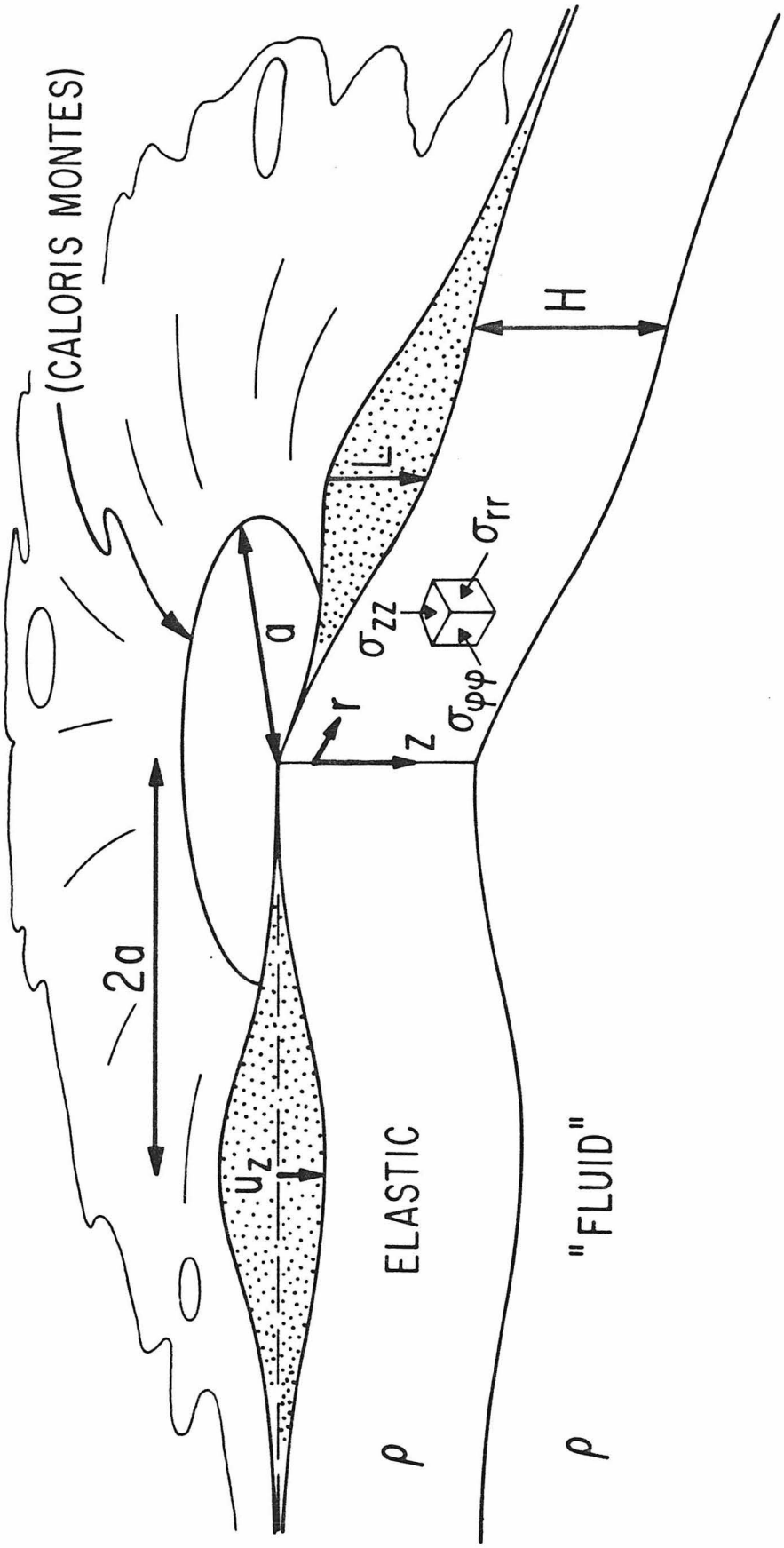
(CALORIS MONTES)
H
L
a
2a
σ_{rr}
σ_{zz}
$\sigma_{\varphi\varphi}$
r
z
u_z
ELASTIC
"FLUID"
ρ
ρ

c) Analysis

The calculations of $\sigma_{rr}|_{z=0}$ and $\sigma_{\varphi\varphi}|_{z=0}$, together with the given load, can be used to determine the tectonic response of the surface using the faulting criteria of E.M. Anderson (1951). The ring load determines up to *seven* tectonic provinces symmetric about the basin center. Figure 39 shows the more important of these. In general, there is a zone of normal faulting within the basin, and thrust faulting under the principal area of the ring load.

The distribution of these provinces as a function of radial distance and lithospheric thickness is given in figure 40a. The tectonic patterns *do not* appear to be a strong function of lithospheric thickness *except* that for H/a > .3 the concentric graben are suppressed in favor of radial normal faults. Even so, close to the basin center the directional control is weak, as lim $r \to 0$ ($\sigma_{rr} = \sigma_{\varphi\varphi}$). The lack of control via lithospheric thickness is due the fact that Caloris is of such a scale that isostatic compensation is very effective.

In examining the tectonic provinces it is also necessary to keep in mind the magnitude of the stresses available for faulting. The relationship between the "shearing stress intensity" (or square root of the second invariant of the stress deviator) T, and the maximum shear stress τ_{max}, is

$$\tau_{max} \leq T \leq \frac{2}{\sqrt{3}} \tau_{max} \quad , \qquad (5.2)$$

FIGURE 39: Generalized surface tectonic style for region inward of 2.5 basin radii. The extent of the central concentric and radial normal fault provinces depends on lithosphere thickness.

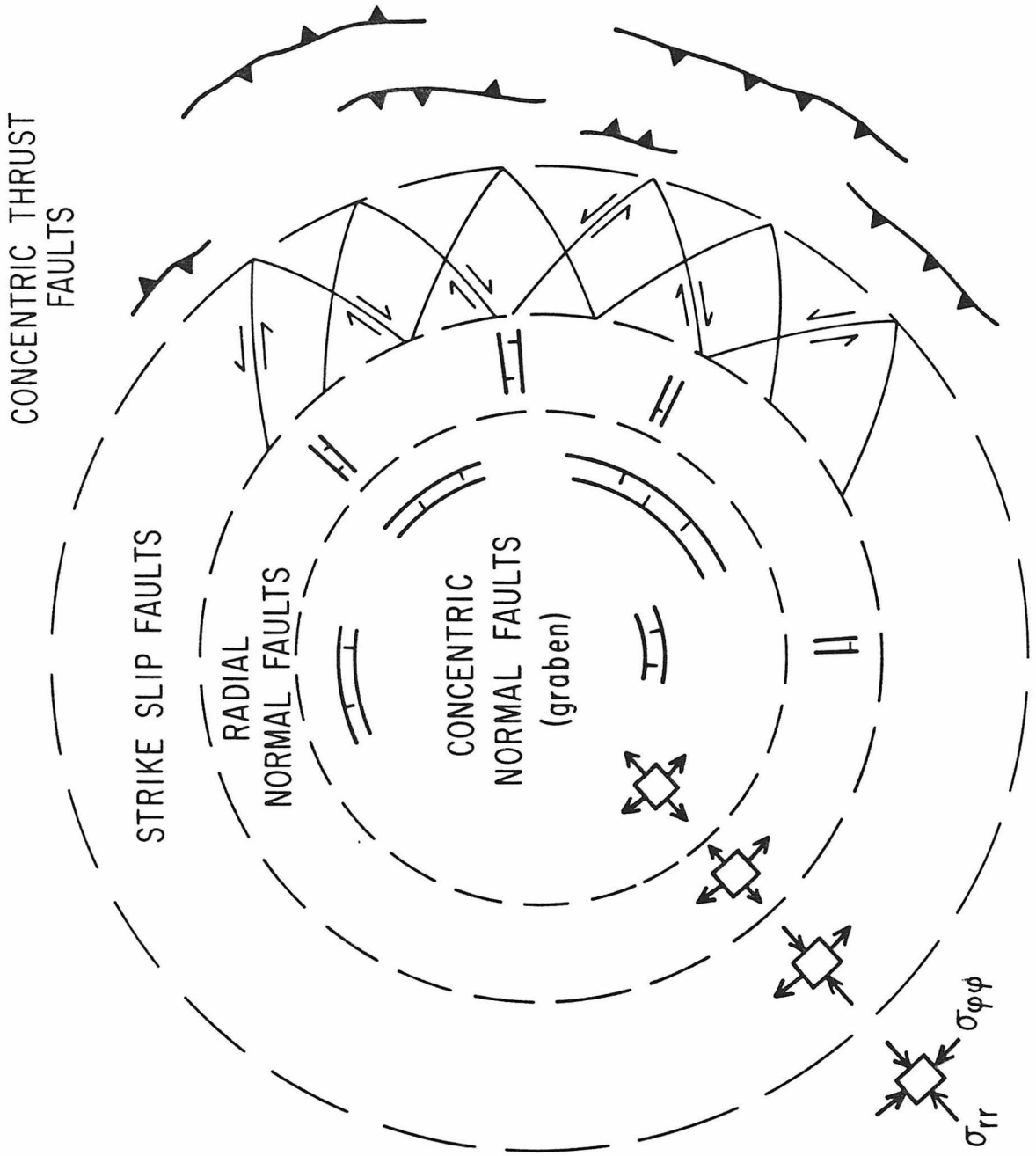
CONCENTRIC THRUST FAULTS
STRIKE SLIP FAULTS
RADIAL NORMAL FAULTS
CONCENTRIC NORMAL FAULTS (graben)
$\sigma_{\varphi\varphi}$
σ_{rr}

FIGURE 40: (a) Surface tectonic style and (b) surface shearing strength intensity T, as a function of radial distance and lithosphere thickness normalized to the basin radius. Calculations are appropriate for Caloris.

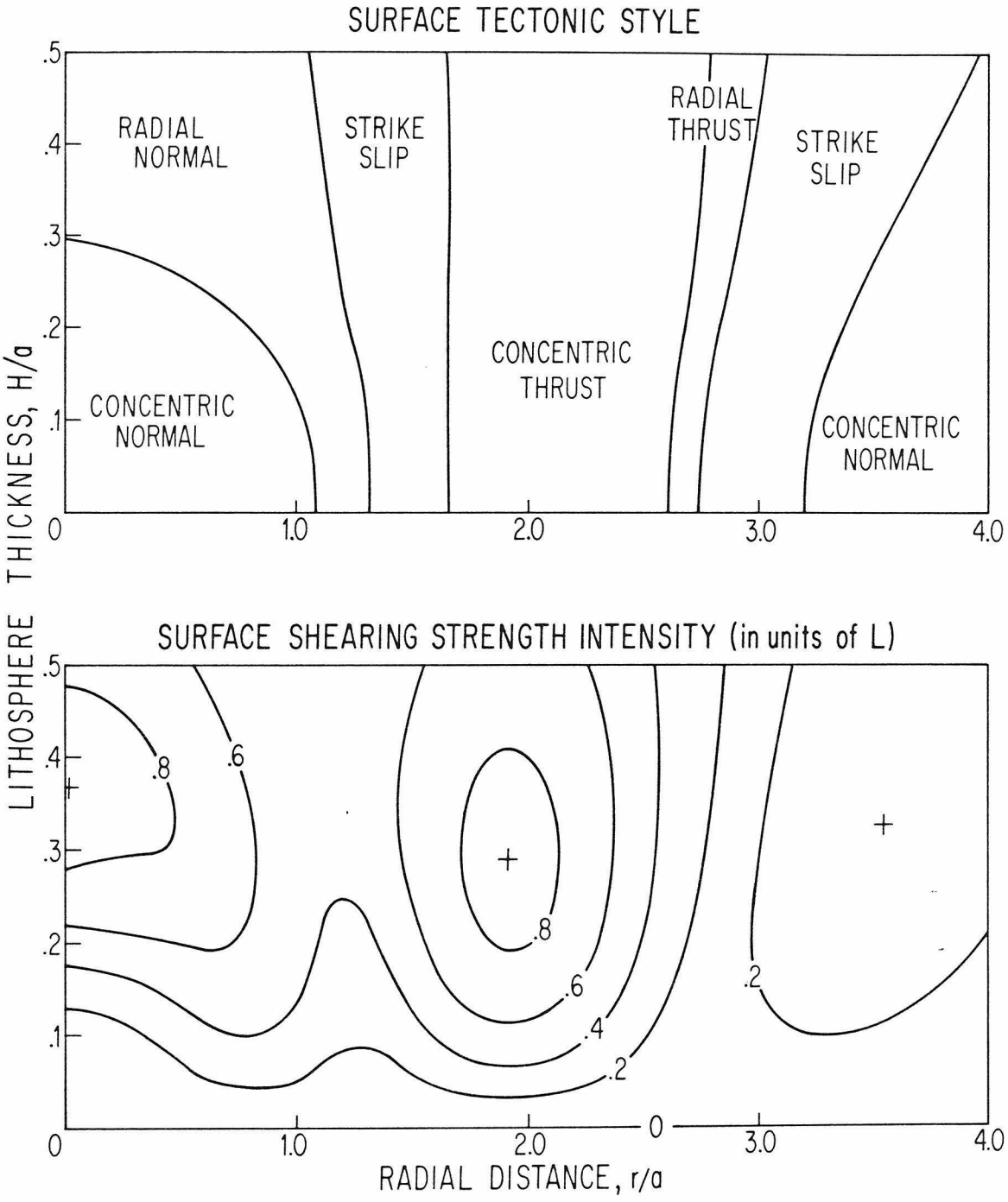
SURFACE TECTONIC STYLE
RADIAL NORMAL
STRIKE SLIP
RADIAL THRUST
STRIKE SLIP
CONCENTRIC NORMAL
CONCENTRIC THRUST
CONCENTRIC NORMAL
LITHOSPHERE THICKNESS, H/a
.5
.4
.3
.2
.1
0
1.0
2.0
3.0
4.0
SURFACE SHEARING STRENGTH INTENSITY (in units of L)
.8
.6
.4
.2
0
RADIAL DISTANCE, r/a

with

$$T \equiv \sqrt{I_2(D_\sigma)} = \frac{1}{\sqrt{6}}\sqrt{(\sigma_{rr}-\sigma_{zz})^2 + (\sigma_{rr}-\sigma_{\phi\phi})^2 + (\sigma_{\phi\phi}-\sigma_{zz})^2 + \sigma_{rz}^2} \quad . \tag{5.3}$$

Geologically useful yield conditions, such as that of Tresca-St. Venant or Von Mises' describe the onset of failure as occurring when T or τ_{max} reaches some fraction of the yield stress (defined as the maximum available deviatoric stress, $\sigma_1 - \sigma_3$):

$$\tau_{max} = \sigma_s/2 \qquad \text{(Tresca-St. Venant)} \tag{5.4a}$$

$$T = \sigma_s/\sqrt{3} \qquad \text{(Von Mises')}, \tag{5.4b}$$

where $\sigma_s \equiv$ the yield stress. Consequently T is related to σ_s by

$$.5\ \sigma_s \leq T \leq .577\ \sigma_s \quad . \tag{5.5}$$

The point is that for different "standard" yield formulations, T is approximately half the yield strength.

Laboratory experiments on the failure of intact rocks measure multi-kilobar yield strengths (Handin, 1966), yet when the terrestrial lithosphere as a whole is considered the yield strengths appear much lower, on the order of a few hundred bars (Chinnery, 1964; McGarr and Gay, 1978). Thus, if this holds true for the inferred silicate lithosphere of Mercury, then T needs only be on the order of a couple of hundred bars to initiate faulting.

In figure 40b T is contoured as a function of radial distance, r/a, and lithospheric thickness, H/a. It is clear that for very

thin lithospheres, a great deal of support for the load is isostatic. The greatest stresses are seen to occur in an intermediate range ($H/a \sim .4$). In terms of radial distance there are two main regimes of stress concentration, the inner extensional zone and the compressive zone under the ring. An outer zone of stress concentration ($r/a \geq .3$) is weak compared to the main two and is thus much less likely to be observed. Faulting is more likely to be realized inward of three basin radii. The inner strike slip zone (fig. 40a) will also experience lower stress due to the ring load than adjacent regions.

As an example assume a ring load peak of 5 km. For Mercury this results in $\sim$ 500 bars. If the lithosphere is $\sim$ 200 km thick (i.e., $H/a \sim .3$), then shearing stress intensities greater than 200 bar will be generated inward of $r = 2.5a$. Strom *et al.* (1975) give a minimum lower thickness to the plains surrounding Caloris of 10 km based on photogeology. It is clear that such an amount of plains material is partly basin ejecta (analogous to the Cayley or Hevelius Formations on the moon) and partly volcanic in origin. Estimates of the purely volcanic contribution to lunar mascon loading (e.g., De Hon, 1979) tend to be much thinner. Nevertheless, such thicknesses make it possible to initiate fracture and faulting even if the Mercurian lithosphere is relatively thin.

Examining the shearing strength intensity, T, as a function of radial distance and depth in the lithosphere, shows that stress concentrates near the top and bottom of the lithospheric plate.

FIGURE 41: (a) Surface displacement and (b) uncompensated surface load as a function of normalized lithosphere thickness and radial distance. Contours are in units of $L/\rho g$ and L, respectively. In 41b dashed contours are negative, indicating (contribution to) a gravity minimum. Flexure of thinner lithospheres results in a slight central positive.

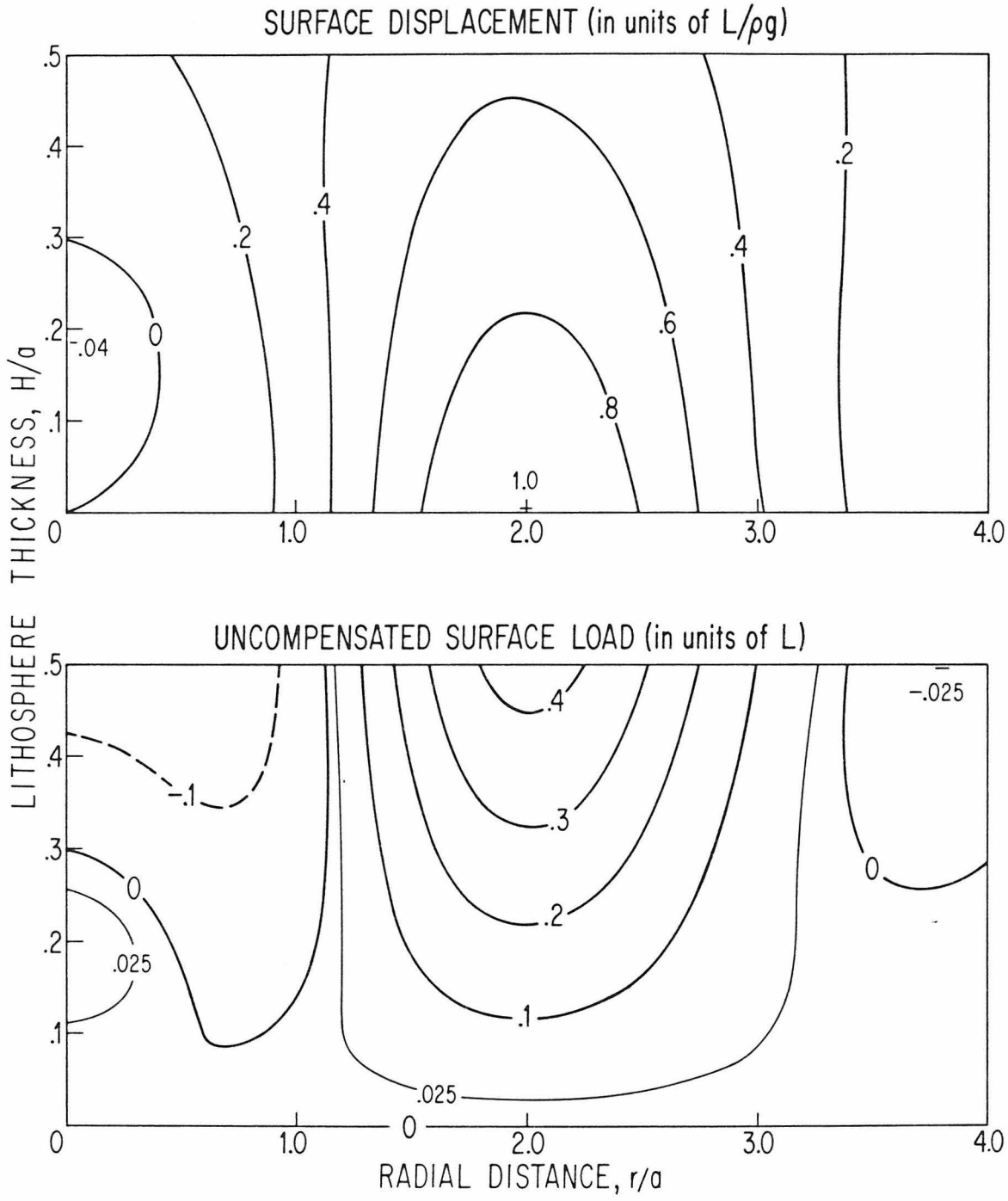
SURFACE DISPLACEMENT (in units of L/ρg)
LITHOSPHERE THICKNESS, H/a
.5
.4
.3
.2
.1
0
.2
.4
.2
.4
.6
.8
1.0
-.04
0
1.0
2.0
3.0
4.0
UNCOMPENSATED SURFACE LOAD (in units of L)
-.1
.4
.3
.2
.1
.025
0
-.025
0
RADIAL DISTANCE, r/a

This is expected when the lithosphere is thin compared to the load dimension, and justifies the application of Anderson's faulting criteria at the upper surface. Brittle failure is more likely to occur near the top of a real lithosphere than at the bottom.

In figure 41a the surface displacement is contoured as a function of radial distance and lithosphere thickness. This displacement (u_z in figure 38) is positive for vertically down, and is given in units of $L/\rho g$, or the isostatic deflection. Thus as the lithospheric thickness goes to zero, the surface deflection mirrors the applied ring load. In general there is a major depression under the ring load, and a relative depression of the basin center. For thinner lithospheres ($H/a < .3$) the basin center is elevated.

From the surface displacement the uncompensated surface load may be computed (fig. 41b). This load contributes to the free air gravity anomaly. The ring load itself is a large positive, the mascon referred to in the introduction. The basin center is an uncompensated gravity low, except for thinner lithospheres ($H/a < .3$) where the very center becomes slightly positive.

d) Comparison to Caloris

Figures 42a and 42b are maps from Strom *et al.* (1975) detailing the tectonic structure near Caloris and in the Caloris hemisphere (as viewed outgoing from the planet). Figure 42b reveals a broad region of fractures and graben with a statistically concentric trend. Outside the basin rim there is a pronounced radial pattern or "lineation." This is considered to be due to emplacement of basin ejecta. The outer zone of compressional features is best seen in figure 42a. Centered at $r \sim 2a$, the dominant trend of the scarps and ridges is concentric, although there are groups of radial and sub-radial trends. These sub-radials may be indicative of strike-slip motion as suggested by Tjia (1970).

The tectonic structure outside the basin is quite complex, however, and may reflect the existence of residual stresses *and* tectonic fabric (zones of weakness) on a regional *and* global scale. Thus what is seen could reflect earlier small basin formation, earlier small mascon loading, the dynamics of the Caloris impact and early-time modification, and even the cooling and despinning of the entire planet. To unravel this through photogeology is a formidable task. However, the simplicity of the tectonic expression *within* Caloris argues for basin related driving stresses for *these* features.

FIGURE 42: (a) Preliminary map of scarps, ridges and plains on the outgoing (Caloris) hemisphere. (b) Preliminary structural map of Caloris. Only fracture pattern is shown within basin. Both are from Strom *et al.* (1975).

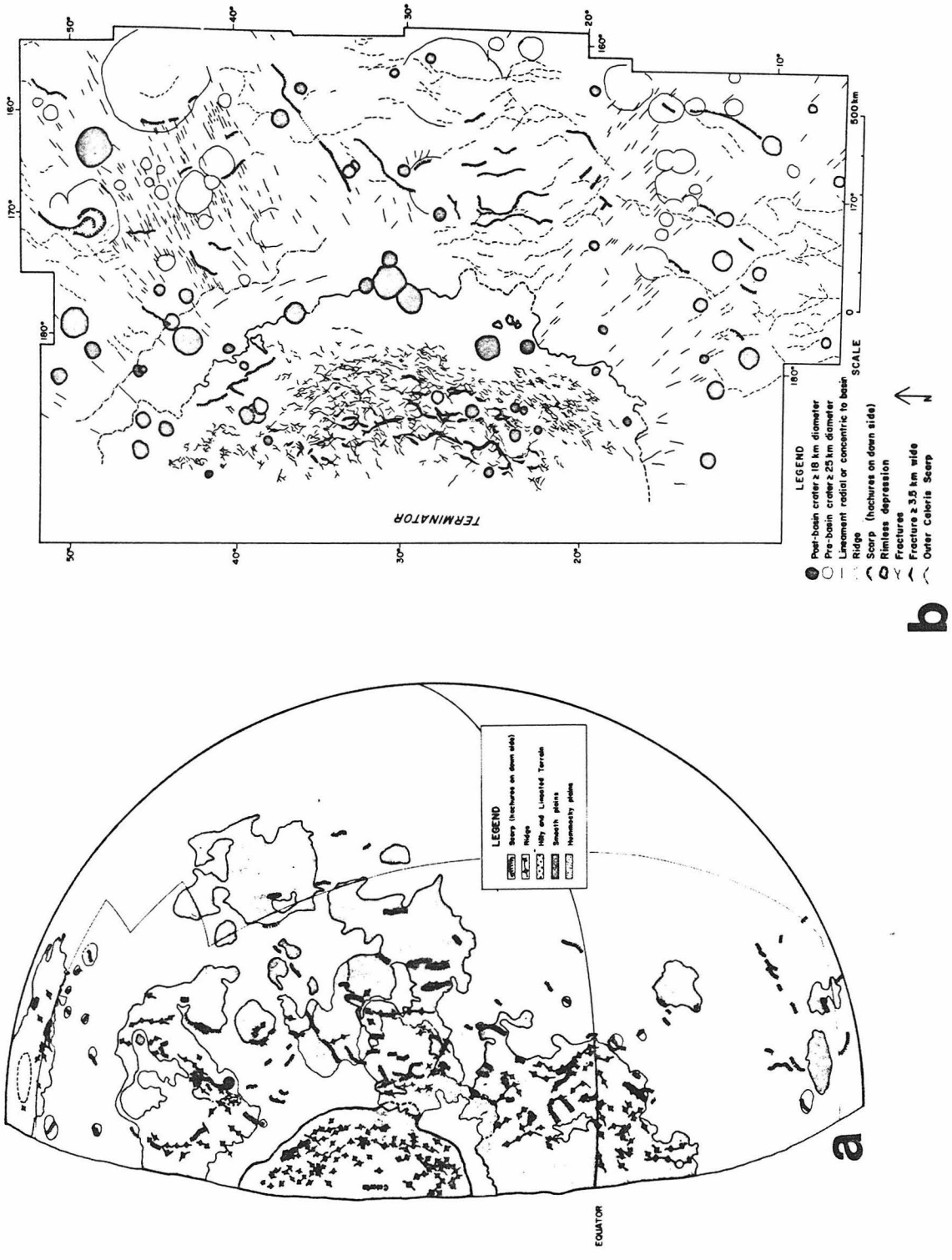
TERMINATOR
LEGEND
Post-basin crater ≥ 18 km diameter
Pre-basin crater ≥ 25 km diameter
Lineament radial or concentric to basin
Ridge
Scarp (hachures on down side)
Rimless depression
Fractures
Fracture ≥ 35 km wide
Outer Caloris Scarp
SCALE
500 km
N
b
LEGEND
Scarp (hachures on down side)
Ridge
Hilly and Lineated Terrain
Smooth plains
Hummocky plains
EQUATOR
a

e) Conclusions

To the observer's eyes the concentric thrusting predicted by the ring load at $r \sim 2a$ is borne out. The inner zone of strike-slip may be there, depending on the interpretation of tectonic features. Other mechanisms cannot be ruled out. The basin itself, however, contains normal faulting, dominantly concentric, subdominantly radial. This would be consistent with the ring load hypothesis for thinner lithospheres ($H/a < 0.2$). This constrains the lithospheric thickness to be ≤ 125 km. A substantial amount of concentric faulting relieves the radial tension locally, allowing radial normals to develop.

It should be emphasized that simple updoming within the basin would produce normal faults of predominantly radial orientation. The cross-cutting relationships of the basin graben and ridges illustrates the fact that the graben are new features, not reactivated, older low angle thrusts. This argues against the suggestion of Strom (1979) that the updoming was due to an ultrabasic intrusion. Presumably the lack of associated surface volcanics would make this an intrusive pluton. Furthermore, cooling of such a widespread pluton would lead to a subsequent episode of surface compression, postdating the graben. This is not observed. The ring load provides for the *final* isostatic adjustment of the basin.

If the lithosphere is too thin, however ($H/a < 0.1$), not enough deviatoric stress will be available for faulting (even for a 10 km ring load). Thus $H \geq 75$ km. These first limits on the thickness of the Mercurian lithosphere (though only at the time of faulting) provide a

constraint on thermal models. They also provide, for reasonable load magnitudes, the necessary uncompensated mass to substantially contribute to Mercury's inertial figure. The free air gravity signature over the basin is specific to the thickness estimates, and may be tested with a future orbiter mission to the planet.

APPENDIX

The analysis begins by rewriting the equilibrium equations for axial symmetry (eqns. 2.5):

$$\frac{1}{r}(r\sigma_{rr}),r - \frac{1}{r}\sigma_{\phi\phi} + \sigma_{rz,z} = 0 \qquad \text{(A.1a)}$$

$$\frac{1}{r}(r\sigma_{rz}),r + \sigma_{zz,z} = 0 \quad . \qquad \text{(A.1b)}$$

The hydrostatic pressure variation in the elastic slab is formally uncoupled by dropping the gravitational body force term. It and the hydrostatic compression in the strain field can be linearly superposed.

This form is particularly elegant as it admits solutions in terms of a scalar stress function (analogous to the Airy stress function in plane strain). Let $\chi(r,z)$ be that function. Then if

$$\sigma_{zz} = (3\lambda + 4\mu)\nabla^2\chi,_z - 2(\lambda+\mu)\chi,_{zzz} \qquad \text{(A.2a)}$$

$$\sigma_{rz} = (\lambda + 2\mu)\nabla^2\chi,_r - 2(\lambda+\mu)\chi,_{zzr} \qquad \text{(A.2b)}$$

$$\sigma_{rr} = \lambda\nabla^2\chi,_z - 2(\lambda+\mu)\chi,_{zrr} \qquad \text{(A.2c)}$$

$$\sigma_{\phi\phi} = \lambda\nabla^2\chi,_z - 2(1/r)(\lambda+\mu)\chi,_{zr} \quad , \qquad \text{(A.2d)}$$

where λ and μ are constants, then equations (A.1) are satisfied (Heaps, 1953). Alternatively,

$$\sigma_{zz} = (1/r)(r\chi_{,r})_{,r} \tag{A.3a}$$

$$\sigma_{rz} = -\chi_{,rz} \tag{A.3b}$$

$$\sigma_{rr} = \chi_{,zz} - (1/r^2) \int r \{\chi_{,zz} - \nu\nabla^2\chi\}dr \tag{A.3c}$$

$$\sigma_{\phi\phi} = \nu\nabla^2\chi + (1/r^2) \int r \{\chi_{,zz} - \nu\nabla^2\chi\}dr \quad , \tag{A.3d}$$

where ν is Poisson's ratio, suffices. Both require χ to obey the biharmonic equation (in cylindrical coordinates).

$$\nabla^4\chi = 0 \quad . \tag{A.4}$$

This equation admits a solution

$$\chi = J_o(kr) \{ (A + Bz) \sinh kz + (C + Dz) \cosh kz\} \quad , \tag{A.5}$$

where k, A, B, C, and D are arbitrary constants. It is easily shown that $\sigma_{zz} = -k^2\chi$ for this solution. Then, following Melosh (1978), if the load condition at the top of the slab ($\sigma_{zz}\Big|_{z=0}$) possesses a Bessel series or integral representation, the solution (A.5) will be complete

when given the boundary conditions (i.e., specifying $\sigma_{zz}\Big|_{z=0}$, $\sigma_{zz}\Big|_{z=H}$, $\sigma_{rz}\Big|_{z=0}$, and $\sigma_{rz}\Big|_{z=H}$). For this problem all but $\sigma_{zz}\Big|_{z=0}$ are identically zero. The Bessel integral form of equation (5.1) is

$$-L\, e^2\, \frac{a^2}{4} \int_0^\infty e^{-a^2k^2/2} \left(2k - 2a^2k^3 + a^4\, \frac{k^5}{4}\right) J_o(kr)\,dk \quad . \qquad (A.6)$$

Buoyancy enters in by reducing the applied load by an amount $\rho g u_z\Big|_{z=0}$ (Heaps, 1953). Note

$$u_z = (1/E) \int \{(1 + \nu)\sigma_{zz} - \nu\sigma_{kk}\}dz \qquad (A.7)$$

and

$$\sigma_{kk} = (1 + \nu)\nabla^2\chi \quad , \qquad (A.8)$$

where E is Young's modulus. Small normal flexural displacements of a thin, elastic, spherical shell floating on a liquid interior are given by

$$EH^3/[R(1 - \nu^2)]\nabla^4 u_z + (EH/R^2)u_z + \rho g u_z = L \quad , \qquad (A.9)$$

where R is the planetary radius, and L is the load (Brotchie, 1971). Thus membrane stress due to curvature may be parameterized (Melosh, 1978) in the cylindrical case by an effective buoyancy EHu_z/R^2. For Mercury EH/R^2 is generally small compared to ρg, so the approximation is good,

and the biharmonic solution may be used. In the thin shell limit, of course, the approximation becomes exact.

REFERENCES

Anderson, E.M. (1951). *The Dynamics of Faulting*. Oliver and Boyd, Edinburgh. 206 pp.

Brotchie, J.F. (1971). Flexure of a liquid-filled spherical shell in a radial gravity field. *Modern Geology 3*, 15-23.

Chinnery, M.A. (1964). The strength of the earth's crust under horizontal shear stress. *J. Geophys. Res. 69*, 2085-2089.

De Hon, R.A. (1979). Thickness of the western mare basalts. *Proc. Lunar Planet. Sci. Conf. 10th*, 2935-2955.

Goldreich, P. and Peale, S. (1966). Spin-orbit coupling in the solar system. *Astron. J. 71*, 425-438.

Guest, J.E. and Greeley, R. (1979). Geologic map of the Shakespeare Quadrangle of Mercury. *U.S. Geol. Surv. Map* (in Survey review).

Handin, J.A. (1966). Strength and ductility. *GSA Memoir 97*, 223-289.

Heaps, H.A. (1953). Stresses in the earth's crust under an axial symmetrical load. *Trans. AGU 34*, 769-775.

McGarr, A. and Gay, N.C. (1978). State of stress in the earth's crust. *Ann. Rev. Earth Planet. Sci. 6*, 405-436.

Melosh, H.J. (1978). Tectonics of mascon loading. *Proc. Lunar Planet. Sci. Conf. 9th*, 3513-3525.

Melosh, H.J. and Dzurisin, D. (1978). Tectonic implications for the gravity structure of Caloris Basin, Mercury. *Icarus 33*, 141-144.

Schaber, G.G. and McCauley, J.F. (1980). Geologic map of the Tolstoj Quadrangle of Mercury. *U.S. Geol. Surv. Map I-1199*.

Solomon, S.C. (1976). Some aspects of core formation in Mercury. *Icarus 28*, 509-521.

Strom, R.G. (1979). Mercury: A post-Mariner 10 assessment. *Space Sci. Rev. 24*, 3-70.

Strom, R.G., Trask, N.J. and Guest, J.E. (1975). Tectonism and volcanism on Mercury. *J. Geophys. Res. 80*, 2478-2507.

Tjia, H.D. (1970). Lunar wrinkle ridges indicative of strike-slip faulting. *Geol. Soc. Amer. Bull. 81*, 3095-3100.

Trask, N.J. and Guest, J.E. (1975). Preliminary geologic terrain map of Mercury. *J. Geophys. Res. 80*, 2461-2477.

Zohar, S. and Goldstein, R.M. (1974). Surface features on Mercury. *Astron. J. 79*, 85-91.